Title

Effects of dissolved organic matter, available retention sites, shear induced aggregation and surface heterogeneity in subsurface colloid transport

Author

Patiño Higuita, Janis Eneida

Publication Date

2022

Peer reviewed|Thesis/dissertation

Effects of Dissolved Organic Matter, Available Retention Sites, Shear Induced Aggregation and Surface Heterogeneity in Subsurface Colloid Transport

By

JANIS ENEIDA PATIÑO HIGUITA

DISSERTATION

Submitted in partial satisfaction of the requirements for the degree of

DOCTOR OF PHILOSOPHY

in

Civil and Environmental Engineering

in the

OFFICE OF GRADUATE STUDIES

of the

UNIVERSITY OF CALIFORNIA

DAVIS

Approved:

Veronica L. Morales

Thomas Harter

William P. Johnson

Committee in Charge

2022

Abstract

The way in which colloidal particles are transported and eventually retained throughout the subsurface porous media is a multi-scale problem that has direct implications for environmental, agricultural and public health sectors. Classic and current filtration models fail to accurately predict the fate of colloids, because they are largely based on mean-field values of surface and flow properties or because they do not account for the complexity of real systems.

The goal of this research is to improve predictive models and describe important mechanisms governing the fate and transport of colloids in the subsoil across different spatial scales–interface scale, pore/collector scale, Darcy scale–with a focus on silver engineered colloids and conditions relevant to agricultural soils. The work comprises a combination of novel experimental techniques and modeling approaches to improve our understanding of: i) short range forces affecting the attachment of colloids to surfaces in complex solution chemistries, ii) pore-scale locations where colloids are statistically most likely to be retained, iii) the influence of shear-induced aggregation on the overall particle distribution and re-entrainment into the bulk liquid phase, and iv) the link between the mechanisms responsible for colloid retention in porous media (from model simulations) and their fate (from experimental observations) in the presence of surface chemical heterogeneity under bulk unfavorable conditions.

This dissertation is divided into four projects that address current knowledge gaps concerning colloid transport:

The first project provides insight into the colloid-surface interaction energy when dissolved organic matter (DOM) is present in solution in the form of humic acid (HA). We investigated the origin and magnitude of opposing forces between silver and mica surfaces (representing nanosilver and sand grains) in solutions relevant to agricultural soils with direct measurements using a surface force apparatus. The results indicate that HA forms an adsorbed surface layer onto both surfaces with substrate-dependent properties. Ca^{+2} significantly modifies the adsorption layer characteristics (thickness and compressibility), hence the interaction energy profiles. Force-distance measurements indicate that when silver-mica systems are exposed to HA, osmotic-steric, electrostatic and van der Waals forces dominate. Soft particle theory is deemed inappropriate for this system. We instead propose attachment efficiency estimates from measured surface properties, which suggest high particle mobility when nanosilver is applied to HA-rich agricultural soils with modest ionic strength.

The second project investigates the role that pore structure plays in colloid retention across scales with a novel methodology based on image analysis. High-resolution spatial profiles of retained particles from micro X-ray Computed Tomography allow quantification of the contribution from commonly proposed retention sites toward colloid immobilization. At the Darcy-scale, the spatial distribution of immobilized colloids along the porous medium reveals depth-independent partitioning of colloids among the pore-scale locations. The total mass of retained colloids exhibits non-monotonic deposition profiles, suggesting slow particle release from flow-stagnation zones. At the pore-scale, dominance and overall saturation of all retention sites indicates that the solid-water interface and wedge-shaped regions associated with flow-stagnation (grain-to-grain contacts in saturated and air-water-solid triple points in unsaturated conditions) are the greatest contributors toward retention under the tested conditions. At the interface-scale, xDLVO energy profiles are in agreement with pore-scale observations when the pore structure is taken into account. Our calculations suggest relatively favorable interactions for colloids and solid-water interfaces and for weak flocculation (e.g., at flow-stagnation zones), but highly unfavorable interactions between colloids and air-water interfaces. Overall, we demonstrate that pore-structure plays a critical role in colloid immobilization.

The third project demonstrates that aggregation of a electrostatically stable suspension is induced at typical groundwater velocities. Here, we compare the repulsive DLVO force between particle pairs to the hydrodynamic shear force opposing it acting on suspended particles. Column experiments imaged with high-resolution X-ray Computed Tomography are used to measure aggregate structure and describe their morphology, probability distribution, and spatial distribution. Distributions of aggregate volume and surface area are found to follow a power-law function. Aggregate Feret diameter is deemed to be exponentially distributed with some flow rate dependencies caused by erosion and restructuring by the fluid shear. Furthermore, size and shape of aggregates are heterogeneous in depth, where a small number of large aggregates control the shape of the deposition profile. The range of aggregate fractal dimensions implies a reaction limited aggregation process and a high potential for restructuring and/or breaking during transport. Therefore, while shear-induced aggregation is not currently considered in macroscopic models for particle filtration, it may be critical to consider in the processes that control deposition.

In the fourth project, the soil surface heterogeneity is found to extend the attachment efficiency and residence time of colloidal particles at the near surface. Both of these alterations significantly affect particle transport and retention at each relevant

scale, such that macroscopic observations are deemed anomalous. At the interface-scale, we revise the interaction energy profiles considering chemical heterogeneities of the collector surface. Observations of deposited colloids at the pore scale are contrasted against continuum-scale predictions parameterized from rate coefficients upscaled from modeled Lagrangian trajectories. Results indicate that: i) Colloid-collector interaction energies are non-unique for surface heterogeneous systems and can span from strongly repulsive to strongly attractive; ii) The proportion of simulated particle by active retention mechanisms (fast/slow attachment and retardation at near surface) explain experimentally observed fraction of particles found at available pore-scale retention sites (solid-water interface and grain-to-grain contacts, respectively); and iii) Simulated non-exponential depth profiles of retained colloids and heavy-tailed breakthrough elution curves are in agreement with experimental mass balances and detailed depth profiles.

These collection of findings here reported have direct implications for the protection of subsurface ecosystems and water resources from potential contamination by hazardous colloids and for the rational management of agricultural soils. They are also critical to design strategies that effectively contain nanoparticle contaminant spreading in soils and groundwater.

Contents

State-of-the-art and research needs

1.1 Types of colloids and forms of entry to the subsurface

The fate and transport of colloids (defined as solid phase material with one dimension between 10 nm and 10 μm [1, 2]) is a topic of significant environmental concern for groundwater quality [3]. Colloid particles vary widely in concentration, composition, structure, and size depending on their origin and on site-specific properties [4]. Natural colloids, such as clays, participate in colloid-facilitated transport of pollutants including trace metals [5, 6, 7], pesticides [8, 9, 10] and radionuclides [3, 11, 12]. Pathogenic biocolloids, like viruses, bacteria, and protozoa can be intrinsically hazardous and tend to be implicated in waterborne disease outbreaks [13, 14]. Furthermore, depending on their nature, engineered nanoparticles (ENPs) can be either emerging contaminants [15, 16] or beneficial reagents of soil-groundwater remediation strategies [17, 18, 19]. Accurate prediction of colloid transport and immobilization in the subsurface is then crucial for assessing the risks associated with particle migration, especially when groundwater resources are exploited for drinking water and irrigation purposes. For example, ENPs contained in consumer products can end up in wastewater treatment plants (WWTP) [20]. Form there, the particles might migrate into soils and groundwater directly, when sludge is applied to croplands for nutrient recycling and treated wastewater effluents are used for irrigation purposes [21]. Agricultural soils and groundwater are thus particularly at risk of exhibiting high concentration of colloidal particles and will be the focus of the research herein

proposed.

Once colloids are released into the subsoil, their mobility, bioavailability, and toxicity becomes highly dependent on their surface properties. Colloidal-sized materials have specific physicochemical features as a result of their small size. ENPs in particular may exhibit size-related characteristics that differ significantly from those observed in bulk materials [21]. For instance, nanosilver (n-Ag) particles have a unique antimicrobial effect in comparison to bulk silver that makes them a very popular active ingredient in an increasing number of consumer and medical products to endow them with that property [22]. As a result of the increasing application of n-Ag, the United States Environmental Protection Agency (USEPA) expresses concern regarding its environmental fate, transport, and toxicity. Moreover, according to the USEPA, there is little to no information on the behavior of n-Ag in the environment and the same gap in the literature can be extended to other colloidal size materials [21]. As will be discussed in sections below, colloidal and nano silver are the subject of investigation for the projects of this dissertation.

1.2 Colloidal Silver

The application of silver-based colloids in consumer products has increased in the last 20 years [23, 24, 25]. Nanosilver (n-Ag) in particular, is used in the electronic industry [26], in medical applications[27], as an additive in paint coatings [28], and has gained popularity due to its biocidal properties in the garment industry to create odor-free clothing. Nonetheless, n-Ag inactivates microbes indiscriminately, which raises concerns regarding the impact that n-Ag will have on beneficial microbial colonies of wastewater treatment plants and soil ecosystems receiving large loads of n-Ag rich biosolids, which includes agricultural soils. Studies to date on colloidal silver have investigated its release rates from consumer products [29, 25], accumulation in sewage sludge [30, 31, 23, 21], aggregation behavior in aquatic systems [21, 29], and toxicity

on environmentally relevant microorganisms [32, 33]. The transport of these silver colloids in structurally complex porous media, under representative environmental conditions has received limited attention [34, 35] and needs to be understood to better evaluate the environmental risks of large loading of n-Ag in the environment [4]. The research plan that we propose will be carried out using colloidal silver since this material represents a specific concern for the general protection of environmental and public health.

1.3 Fate and transport models

The chemical and physical properties of natural porous media vary in space and in time. Numerical or analytical flow and transport models in general cannot resolve all variation scales of the spatial medium fluctuations due to limitations in computer power and characterization techniques [36]. We propose here a study of fate and transport of colloids that combines information at three different scales. First, quantitative information on the interaction energy between colloids and charged surfaces within soil pores is investigated at the **interface scale**, by directly measuring interaction forces. The interaction energy plays a critical role in determining the likelihood for colloid attachment to available interfaces in natural porous media (i.e. soil-water interface, air-water interface, grain to grain contacts, and the air-water-sold triple point), which are local representations of processes of filtration. Additionally, interaction energy is used in determining the stability of colloidal suspensions [37], which is known to also affect filtration [38, 39, 40, 41].

Second, colloid transport at the **pore scale** is investigated given that reactions among aqueous species and between aqueous species and the solid phase are considered a pore-scale phenomena [36]. Colloids have sizes from few nanometers to few micrometers while the pore scale encompasses a few micrometers to milimeters. Thus, it is a scale sufficiently large to analyze transport and deposition of individual

colloids as well as aggregates, while keeping information on the pore geometry. Furthermore, together with the interface-scale, the pore-scale is well-suited to investigate colloid transport and retention in the subsurface because it facilitates the analysis of colloid interactions with dissolved substances in the pore water and available interfaces for particle immobilization. For example, evidence of colloid retention at the air water interface (AWI) and air-water-solid (AWS) triple point, has been collected from analysis at the pore scale [42, 43]. The same conclusion can be drawn regarding evidence of colloid size exclusion [42], attachment, and straining processes affecting colloid retention [4, 44]. One of the hypotheses of the research proposed here is that experiments and modeling tools applied at the pore scale will indeed provide results that are relevant for macroscopic scales and consequential for better soil protection and management of colloid release.

Finally, we considered data from column experiments to obtain information on processes taking place at the **Darcy scale**, which typically covers a few pore sizes to decimeters [45]. We expect these data to reflect the transport behavior resulting from the cumulative effect of processes occurring at the pore and interface scales. At this scale, we address different cases where the pore structure of the medium is not uniform to determine if the pore structure or the interactions of the colloids with interfaces of the system play a larger role in filtration.

The classic colloid filtration theory (CFT) originally developed by Yao et al. [46] is a conceptual model from which most of the current approaches for predicting colloid fate and transport in the subsoil are built on [47, 48, 3]. The model is probabilistic and captures filtration as a processes involving two sequential steps. First, some fraction of suspended particles moving in the bulk pore will strike the porous medium (transport). Second, some fraction of those particles that arrived to the porous medium surface will attach to the grain (attachment). The transport term of the model can be computed analytically from system parameters with well accepted methods, as

detailed below. However, no accepted form exists as of yet to calculate the attachment term. CFT considers a single spherical particle of the filter media (collector), and three main processes by which a suspended particle can encounter the collector surface. First, a suspended particle can come in contact with the collector by its own size in a process known as *interception*. Additionally, the particle can follow a trajectory not dictated by the streamlines if its density is greater than that of water and get to the collector due to the influence of the gravitational force field. The transport mechanism in this case is influenced by the fluid drag on the particle and its buoyant weight and it is called *sedimentation*. Lastly, if Brownian motion has a considerable effect, as in the case of small particles with high molecular diffusion coefficients, mass transport to the collector is likely to happen by *diffusion* [46].

The governing equation to describe the temporal and spatial variation of particle concentration through a saturated homogeneous porous media in a steady-flow field is the one-dimensional advective dispersive equation (ADE) with a first-order kinetic deposition term [49, 50]:

$$\frac{\partial C}{\partial t} + \frac{\rho_b}{\theta}\frac{\partial S}{\partial t} = D\frac{\partial^2 C}{\partial x^2} - v\frac{\partial C}{\partial x} \tag{1.1}$$

$$\frac{\rho_b}{\theta}\frac{\partial S}{\partial t} = kC \tag{1.2}$$

Where C is the concentration of colloids in suspension, S is the concentration of retained particles, ρ_b is the bulk density, θ is the porosity of the medium, D is the hydrodynamic dispersion coefficient, v is the advective pore velocity, and k is an irreversible particle deposition rate coefficient. The main challenge in modeling colloid transport and fate lies in predicting the magnitude of k from system properties, as the rest of the parameters involved in the ADE.

Mass balance for the deposition of colloids in a clean packed filter bed of uni-

form spherical collectors yields the following relationship between k and the physical properties of the collection of collectors in the filter [51, 52]:

$$k = \frac{3(1-\theta)v}{2d_c}\eta \tag{1.3}$$

where d_c is the diameter of the collector and η is the single-collector removal efficiency, defined as the ratio of the total particle deposition rate on the collector to the rate at which particles approach the projected area of the collector from the upstream. This dimensionless deposition (or removal) rate of particles can be viewed as a product of an attachment efficiency (α) and a dimensionless transport rate (η_0) [53]:

$$\eta = \alpha\eta_0 \tag{1.4}$$

It is important to highlight that α is the term that would account for short-range interactions between the surfaces of particles and collectors (e.g., electrostatic repulsion), while η_0 accounts for hydrodynamic effects [53]. Thus, when interfacial interactions are favorable for deposition (i.e., in the absence of repulsive total interaction energies), α approaches unity, and the deposition rate is equal to the transport rate ($\eta = \eta_0$). In this case, particle transport is the rate-determining step. On the other hand, when interfacial interactions are unfavorable for deposition (i.e., repulsive interactions predominate between particles and collectors), α is much smaller than one and particle deposition rates are reduced. This case is referred to as unfavorable deposition [53]. The rate at which particles collide with the collector is related to the rate at which particles flow toward it, by η_0. Available expressions to calculate the value of η_0 [51, 48], follow the general form:

$$\eta_0 = \eta_I + \eta_G + \eta_D \tag{1.5}$$

where η_I, η_G and η_D are the contributions of the transport mechanisms that can result in contact between particles and collectors according to the CFT: interception, sedimentation and diffusion, respectively. Although Yao et al. (1971) proposed mathematical relations to calculate the individual terms in Equation 1.5 [46], alternative correlations have been derived to account for hydrodynamic and van der Waals interactions [48]; the role of the first one in the filtration behavior of colloids has been demonstrated by numerical solutions to Equation 1.1 while the second one is important for high ionic concentrations in solution [54]; and the array of the collectors [55]. Messina et al. (2006) found that if sedimentation and interception are the dominant transport mechanisms, the collector efficiency of the first sphere that encounters the colloid particles is significantly higher compared to the others, and then declines along the array down to an asymptotic value [55].

1.4 Colloidal forces and α

To capture the effects of solution chemistry on the stability or filtration ability of colloids, the interaction force or energy between a colloid with another colloid or a colloid with an interface, respectively, is typically computed. Specifically, DLVO theory estimates the thermodynamic net energy between charged particles immersed in a conductive medium, water in our case, as a function of their separation distance. In its classic form, DLVO theory describes the interacting energies as the sum of van der Waals and electrostatic interactions [56, 57]. An interaction energy profile between colloids and collectors can be constructed by taking this sum of attractive (negative) and repulsive (positive) interactions over a range of separation distances, as shown in Figure 1-1. The forces acting on the colloids are the derivative of the energies with respect to separation distance [58]. Thus, energy and force profiles exhibit the same features. Figure 1-1 illustrates two typical, classic DLVO interaction energy profiles for favorable (red dashed line) and unfavorable (black solid line) interaction

conditions and distinct regions that are typical of colloid-surface interaction profiles can be identified: primary minimum, repulsive barrier, and secondary minimum [15]. Particle deposition can occur when particle and collector come in proximity of the primary or secondary energy minima in figure 1-1.

In the absence of a repulsive barrier (favorable attachment conditions), α is assumed to be 1 [59]. On the other hand, when repulsive forces prevail between particles and collectors (unfavorable attachment conditions), a repulsive barrier exists (see Figure 1-1) that reduces the probability of colloid attachment to the surface by primary minimum or prevents it completely ($\alpha \sim 0$), depending on the barrier height. However, colloid attachment by secondary minima is still possible in the presence of the barrier, and it has been claimed to be the dominant attachment mechanism for deposition in contrast to particle aggregation [60]. Attachment efficiencies for deposition in the secondary minimum, when present, are associated to the probability that a particle does not have sufficient kinetic energy to overcome the repulsive barrier [61]. On the other hand, attachment efficiencies for deposition in the primary minimum have been related to the fraction of particles with sufficient kinetic energy to overcome the energy barrier and escape retention at the secondary minimum (usually small particles with higher velocities) [61]. It is important to mention that if the secondary minimum is not sufficiently deep (usually, larger than a few kT) the thermal energy may displace particles attached by this minimum and allow their return to the bulk suspension. Some authors have thus estimated the value of α from energy calculations of the depth of the secondary minimum, the height of the energy barrier, (See figure 1-1) and particle kinetic energies [60, 61].

Transitions between unfavorable and favorable conditions are most commonly induced by changes in solution chemistry [62], which can also alter the surface characteristics of particles and collectors [63]. The potential and charge of colloidal particles play fundamental roles in their interfacial electric phenomena, such as electrostatic

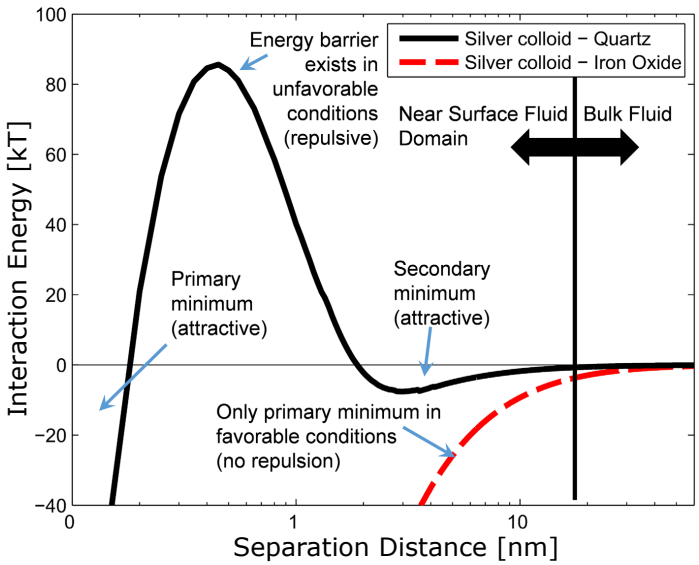

Figure 1-1: Examples of classic DLVO interaction profiles for favorable conditions (dashed red line) and unfavorable conditions (solid black line) for silver colloids interacting with an iron oxide surface and quartz surface respectively in a 300 mM ionic strength solution. Modified from Molnar et al., (2015).

interactions between colloidal particles and collectors and the motion of particles in an electrolyte solution [64]. An example of conditions that create favorable attachment in natural environments is the increase in solution ionic strength, which inhibits electrostatic repulsion by charge neutralization and shrinking of the electron clouds around surfaces.

When forces other than van der Waals and electrostatics are at play, the classic DLVO theory fails to describe, even qualitatively, the resulting interaction between colloids and collectors. Among the extra forces that have been proposed to extend the DLVO theory, we have Born repulsion, due to short range forces generated by the interpenetration of electron shells [58]; magnetic interactions, applicable to materials with magnetic properties [37, 65]; repulsive hydration, that becomes important at high electrolyte concentrations [66]; attractive hydrophobic interactions [58]; and steric interactions, which may take place when the interacting surfaces present chain molecules attached to them at one or multiple points [66, 37, 58].

Soft particle theory (SPT) [67] has been used to describe interfacial interactions

when particles are coated with polymeric layers [64, 68, 65] and to capture the enhanced stability and reduced filtration potential (low α) of polymer-stabilized colloids. However, this approach is not applicable to polymer layers thinner than the inverse Debye length (κ^{-1}) of the solution [64], a condition which is not guaranteed in natural systems. Application of the SPT requires information on electrophoretic mobility, surface charge density, and polymer layer characteristics that are often difficult to measure [65, 69].

Attempts to experimentally characterize the extent of the stabilizer layer on a particle's surface include measurements of the layer thickness by differences in hydrodynamic radius of bare and polymer stabilized colloids by dynamic light scattering (DLS) [69, 70]. To our knowledge, little attention has been paid to possible surface changes of the collector. When stabilizer agents are present in solution, their sorption is not restricted to colloidal particles. For instance, dissolved organic matter, ubiquitous in natural environments, has a high affinity for clay minerals [71] and will affect particle deposition onto these surfaces [72]. In order to incorporate the effects of surface modifications in the expressions for k, information on the characteristics of the material sorbed onto both colloids and collectors is necessary, together with the resulting interaction forces or energies.

1.5 Colloid behavior effects by dissolved organic matter

This section reviews the known effects of dissolved organic matter (DOM) on colloid transport and interactions with the porous medium. Several studies have reported significant changes in colloid mobility in presence of DOM [73, 74, 75, 5, 76, 77]. A typical characteristic of agricultural soils is high concentration of DOM [78] from fertilizer application (ranging from $\sim$ 17 to 86 mg/L C [79]). However, the degree to which macromolecules of DOM (mainly humic and fulvic acids) adsorb onto colloids and collectors and change their stability and attachment efficiency is difficult

to quantify and thereby even more difficult to model. This is because the molecular structure of DOM is first not well known nor is it uniform in all soil environments (e.g., DOM from manure, Elliott Soil, Swannee River, and peat have different chemical compositions). Second, direct measurements of the adsorbed layer thickness, density, and mass adsorbed are not straight forward. Consequently, it is difficult to parametrize mechanistic transport models with uncertain system parameters. DOM can additionally interact with ions present in the pore water after being adsorbed onto the surfaces of colloids and/or collectors [80], thus affecting the electro-steric forces it is responsible for in the colloidal system in question, as well as the molecular configuration it acquires in its sorbed state [76, 77, 73].

In natural environments, nearly all colloids and the collectors where they may deposit or immobilize regardless of inherent mineral type are negatively charged [15], which leads to electric double layer repulsion. In DOM-rich environments, if the DOM molecules adsorb onto colloid or collector surfaces, the negative charge can be enhanced due to the ionization of moieties, such as carboxylic acid -COOH and phenolic -OH groups, which characterize the DOM chemistry [15]. A direct consequence of this is reduced deposition or immobilization of colloids onto the soil grains. However, laboratory experiments consistently observe colloid deposition onto solid grains even at high DOM concentrations in the pore water [53, 81, 82].

Models that attempt to capture the modified colloid-colloid and colloid-collector interactions in the presence of DOM [83] require an extension of classic DLVO theory to account for the additional repulsive forces at play, such as those of steric nature from the adsorbed polymer. Nonetheless, calculations of effective extended DLVO forces in a system requires substantial educated guessing of which combination forces are at play. To circumvent the guess work of theoretical calculations of extended DLVO interactions, the first project of this dissertation opts to measure directly the total interaction forces of silver-silver and silver-mica surfaces in the presence of DOM

by means of a surface force apparatus (SFA). A hypothesis of this research is that a better approach to describe colloid-collector interactions in the presence of dissolved salts and macromolecules is the direct measurement of the overall force at play when colloid and collector surfaces are immersed in water of compositions representative of agricultural soil conditions. These force measurements may be decomposed to elucidate the different unique force contributions to the total energy of interaction. Information regarding the thickness of the sorbed polymer layer, its compressibility, and mass adsorbed can also be extracted from SFA measurements.

1.6 Pore-scale processes

This section reviews the limitations of the most simple governing equation for colloid transport (Equation 1.1), where filtration is captured by a first-order kinetic sink term (Equation 1.2). This description of the system predicts concentrations of retained particles that decay exponentially with distance [84]. However, experimental results of excavated depth profiles have shown deviations from this theoretical behavior. For instance, preferential retention of latex colloids near the source have shown hyper-exponential trends [85]. These observations demonstrate discrepancies in predictions of particle removal when considering the sink term in equation 1.2 to be described by an irreversible first order kinetic process as a general rule. Many authors have highlighted the limitations of this assumption, such as: the existence of an equilibrium relationship between C and S, which would result in retardation on the particle transport but not in the irreversible removal of the particles from the liquid phase [50]; a reversible kinetic process, which would require separate kinetic rates for attachment (k_{att}) and detachment (k_{det}) [86]; and a combination of the processes just mentioned [86].

Colloid retention at sites that are not restricted to the water-solid interface (SW) has been confirm to be significant by numerous groups collecting microscopic data at

the pore-scale [87, 88, 68, 89]. Experimental methods using bright field microscopy (BFM) and confocal laser scanning microscopy (CLSM) provide exceptional resolution of particle location [90]. Nonetheless, these observations are made in only the few pores that can be imaged at a given time, leaving open the question if such observations are representative of the plentiful pores in a porous medium and therefore not allowing the rational incorporation of retention sites into the mechanistic models. For instance, several studies found that straining of particles that are physically too large to pass through certain pores [91, 92] plays a key role in transport and in the shape of the depth profiles. Similarly others found that immobilization at grain-grain contacts (GG) can be significant since this is a hydrodynamically stagnant portion of the porous medium [93, 94]. In unsaturated systems, several groups have implicated attachment to the air-water interface (AWI) as the key difference between colloid filtration in saturated vs. unsaturated soils [95, 96]. Up to now, no study quantified the relative importance of pore-scale retention sites in a statistically representative way. Even so, the many unique retention sites identified cannot be represented in the geometry of Equation 1.2. Here, all retention forms are lumped into a single term that represents the mass removed per unit surface area corresponding to the solid-water interface alone, which is physically incorrect.

Experimental observations and mathematical simulations corroborate that colloid retention in the subsoil is highly dependent on the medium's pore structure and water content [97, 98]. In saturated systems, the most noted retention sites include the above mentioned SW, GG contacts and the mechanism of particle straining [91, 92, 93, 94]. In unsaturated porous media, colloid transport may be influenced by attachment to the same retention sites present in saturated conditions, plus additional sites that come with the presence of the air phase such as the air–water interface (AWI) [99, 42, 95], air–water-solid (AWS) [89, 98, 87, 88, 97] triple point and, straining in water films enveloping the solid phase [95, 100]. Differences in hydrodynamic forces acting

on retained colloids at air-related interfaces (i.e. hydrophobic and capillary) [99] can thus alter colloid transport predictions [4, 101] and need to be considered in addition to the forces present in saturated systems.

The second project of this research proposal, aims to elucidate the most significant pore sites where particle retention takes place in soils under variable pore velocity, saturation, and solution chemistry to justify their consideration in down-/up-scaling modeling efforts. To do so, we analyze the spatial distribution of retained colloids from transport experiments imaged by X-ray computed tomography (XRCT). The obtained pore-site specific spatial maps are statistically evaluated to determine the dominance and saturation of individual retention sites for all pores within the sample. Interfacial interactions from xDLVO are also used to qualitatively rationalize the observed retention trends.

1.7 Shear induced aggregation

A crucial assumption made by CFT is that suspended particles travel and interact with collector surfaces individually. Nonetheless, repeated evidence of the ubiquity of particle aggregation when moving through saturated granular media suggests that this supposition is mechanistically incorrect[102, 40, 41, 39, 103, 97]. Over the third project of this dissertation, we evaluate the hypothesis that hydrodynamic shear is, in some cases, able to provide suspended particles with sufficient energy to overcome electrostatic repulsion, resulting on shear induced aggregation and enhanced colloid filtration. We use direct measurements of the structure of colloid deposits in porous media obtained from XRCT to study the link between imposed flow rate, aggregates morphology, and the mechanisms for particle deposition. To understand the relationship between filtration and aggregate size, we also investigate the aggregates spatial distribution along the porous media and their mechanical properties in light of their tendency to become unstable during a physical or chemical disturbance.

1.8 Surface chemical heterogeneity

As previously mentioned, CFT alone fails to predict colloid transport behaviour in the presence of unfavorable particle-collector interactions (which are the most common in environmental systems), often leading to underestimation of the mass of immobilized particles [84, 104]. Furthermore, traditional CFT cannot explain experimentally-observed anomalous deposition profiles (non-exponential) and heavy-tailed breakthrough curves (see Equations 1.1 and 1.2) [91, 105, 106, 107, 108, 109, 110, 111]. Given these limitations, alternatives to CFT (or modifications to it) are crucial to explain particle retention trends at all spatial scales. A growing body of literature suggests that nanoscale chemical heterogeneities on the surfaces of particles and/or collectors is at least partially responsible for colloid filtration under unfavorable conditions, as heterogeneity creates local regions for favorable particle retention besides broadening the residence time of the colloids within the vicinity of the porous media grains [112, 111, 113, 114, 115, 116]. However, the field of colloid filtration still relies on mean-field values of surface properties to parameterize transport simulations. The final project of this dissertation seeks to explain experimentally-observed colloid retention trends at the pore- and Darcy- scales by using a mechanistic model that accounts for the stochastic nature of particle-collector interactions, which has implications at the interface-, pore-/collector-, and Darcy- scales.

Direct Measurements of the Forces Between Silver and Mica in Humic Substance-Rich Solutions[a]

Janis E. Patiño[1], Tonya Kuhl[2], Verónica L. Morales[1]

[1] Department of Civil and Environmental Engineering, University of California, Davis

Davis, United States

[2]Department of Chemical Engineering, University of California, Davis

Davis, United States

Abstract

Deposition of engineered nanoparticles onto porous media from flowing suspensions is important for soil and groundwater quality. The deposition mechanism is controlled by interaction forces between particles and collectors. We investigated the origin and magnitude of opposing forces between silver and mica surfaces (representing nanosilver and sand grains) in solutions relevant to agricultural soils with direct measurements using a surface force apparatus. Solutions of variable $NaNO_3$, $Ca(NO_3)_2$ and humic acid (HA) concentration were used to differentiate individual contributing forces and quantify surface properties. The measured Hamaker constant for silver-water-mica was consistent with Lifshitz theory. Our results indicate that HA forms an adsorbed surface layer, but its charge, thicknesses, compressibility, and mass are significantly larger on mica than silver. Ca^{+2} primarily reduced the differences between the initially adsorbed HA layer properties on each surface. Force-distance profiles indicate that when silver-mica systems were exposed to HA, osmotic-steric, electrostatic and van der Waals forces dominate. Soft particle theory

[a]This chapter has been published as: Patiño, J. E., Kuhl, T. L., & Morales, V. L. (2020). Direct Measurements of the Forces between Silver and Mica in Humic Substance-Rich Solutions. Environmental Science & Technology, 54(23), 15076-15085.

was deemed inappropriate for this system. Derjaguin's approximation was utilized to translate force measurements into interaction energy between nanosilver particles and mica-collectors. We propose attachment efficiency estimates from measured surface properties, which suggest high particle mobility when nanosilver is applied to HA-rich agricultural soils with modest ionic strength.

2.1 Introduction

The expanding application of engineered nanoparticles (ENPs) in medical products, textiles, paints, cleaning agents, electric appliances, and cosmetics is increasing their presence in the natural environment [29, 117, 25, 118, 26]. Nanosilver (n-Ag) in particular is broadly used because of its biocidal properties[119, 120, 121]. Several studies have found that n-Ag erodes from consumer products and is released into wastewater treatment plants, where it is removed from the wastewater and accumulated in the sludge [29, 25, 122, 123]. In the United States sludge is commonly applied to agricultural soils to recycle nutrients, which serves as a major entry route for ENPs into soil and water environments[124, 125]. Excessive n-Ag release into the subsurface raises concerns regarding the impact it could have on the quality of groundwater used for potable water production, and the potential toxic or detrimental effects on beneficial soil microorganisms [126, 127, 32, 33]. Toxicity mitigation of n-Ag towards soil bacteria has been observed when ENPs are coated with humic acid and other organic materials in the pore water [128]. Understanding the transport and fate processes of ENPs in natural matrices like agricultural soils is therefore essential to the protection and future use of soil and groundwater resources.

Transport and deposition of suspended particles onto the surface of porous media is commonly modeled with colloid filtration theory (CFT). In CFT, deposition is described as a first-order kinetic process that depends on two sequential steps. First, the single-collector contact efficiency, η_0, captures the mass transfer rate from the bulk fluid to the solid surface controlled by diffusion, interception and sedimentation[48].

Second, the attachment efficiency, α, captures the energy of interaction between the particle and the solid[46]. Classic Derjaguin-Landau-Verwey-Overbeek (DLVO) theory[56, 129], and extensions to it (e.g., Ohshima, Grasso et al., Dwivedi et al., [64, 130, 131] and references therein), are the gold standard for describing the additive attractive and repulsive interactions as a function of separation distance. The one-dimensional form of CFT describes colloid concentration, C, in time and space as:

$$\frac{\partial C}{\partial t} = D\frac{\partial^2 C}{\partial x^2} - v\frac{\partial C}{\partial x} - k_d C, \tag{2.1}$$

where D and v are the dispersive and advective terms, respectively. k_d is the irreversible deposition rate coefficient, which is related to contact and attachment efficiency terms via [132, 133]:

$$k_d = \frac{3}{4}\frac{(1-\theta)}{R_M} v\alpha\eta_0. \tag{2.2}$$

Here, θ is the porosity of the medium and R_M is the mean radius of the soil grains (collectors). While η_0 can be evaluated from well-accepted correlations[48, 134], there is not yet a similarly accepted and general correlation to determine α from suspension properties or DLVO profiles, although several different approaches have been proposed[135, 136, 137, 69, 61]. Specifically, a general validated model for α that describes both bare and polymer-coated particles is still lacking.

Deposition of ENPs within the soil environment by either individual particles or homo/hetero-aggregates is greatly influenced by the combined effects of solution ionic strength (IS), ionic composition, pH, stabilizing agent, and organic matter[118]. Macromolecular interactions with dissolved organic matter (DOM), such as humic and fulvic acids in soil pore water, have been found to have a profound impact on ENP stability in terrestrial and aquatic environments[138, 139, 140, 141, 142]. On the

one hand, humic substances readily adsorb to surfaces and act as stabilizing agents for colloids and ENPs in DOM-rich solutions[143, 144, 76], thereby potentially altering their transport in granular media[145, 146]. On the other hand, the presence of Ca^{+2} modifies ENP-DOM complexes through cation bridging, which can cause charge neutralization or reversal and enhance retention with delayed breakthrough[147, 148]. Despite numerous studies of aggregation, adsorption, and deposition of ENPs with DOM[149, 150, 151, 146, 152, 153], direct quantification of the relative contribution from specific interactions between the surfaces of ENPs and soil grains (van der Waals, electrostatic, osmotic-steric, elastic-steric, etc.) to the resulting total force, and thus, to particle deposition, is lacking. This is due in part to the limited experimental methods available to directly evaluate colloidal forces (e.g., by atomic force microscopy[154] or surface force apparatus[155]), substantial guess-work involved in modeling the theoretical energy of interaction, and difficulty in properly characterizing adsorbed layer properties. Such information is highly dependent on the characteristics of the bare substrates and is required to parameterize transport models to improve particle migration predictions. These knowledge gaps are addressed in this study.

The objective of this work was to directly measure the interaction force profile between silver and mica surfaces in solutions representative of agricultural soils. The actual surface potentials, DOM adsorbed layer thickness, and compressibility, as well as total colloid forces were determined experimentally. Separation of the force profiles into their individual contributions allowed us to establish their origin. The measured force profiles for different solution conditions were translated into energy of interaction profiles for cases of n-Ag particles interacting with sand-like collectors. Each suspension's expected attachment efficiency was parameterized by precise measurements of surface and adsorbed layer properties and modeled with CFT.

2.2 Materials and Methods

2.2.1 Materials

Measurements were made under three different solution conditions. The first (termed "control") was composed of an electrolyte solution of 0.5 mM $NaNO_3$ (99.995 %, Sigma, St. Louis, MO) to define the physical contact between the surfaces and their surface charge properties. The second (termed "-HA") was composed of 0.5 mM $NaNO_3$ with 20 mg/L of Eliott Soil humic acid (HA) (International Humic Substances Society, St. Paul, MN). The concentration of 20 mg/L was selected to mimic DOM-rich groundwater conditions (18 - 20 mg C/L)[156]. The third (termed "-HA-Ca") was composed of 0.5 mM $NaNO_3$, 0.25 mM $Ca(NO_3)_2$ (99.995 %, Sigma, St. Louis, MO), and 20 mg/L HA. Milli-Q gradient water (resistivity of 18 MΩ·cm) was used to prepare the solutions and pH was adjusted to 7 by addition of NaOH. The surfaces studied were silver and ruby muscovite mica (S&J Trading, New York), which are described in detail in the next section. Silver particles of 100 nm diameter stabilized with sodium citrate (Sigma Aldrich) were used in zeta-potential measurements.

2.2.2 Surface Force Measurements

A custom-automated surface force apparatus (SFA) was used to measure interaction forces between silver and mica surfaces. This methodology was chosen because it allows for direct and precise measurements at separation distances down to 0.1 nm, thus providing a "ground truth force profile" of the system[58]. Additionally, the use of SFA facilitated the definition of an absolute reference for contact between the surfaces, which is a limitation of alternative methodologies. SFA uses multiple-beam interferometry to directly measure surface separation and contact geometry[157]. The technique is described in detail elsewhere[58, 155, 158]. Briefly, one surface (mica) was mounted on a fixed stage while the second (mica/silver) was mounted on a double-

cantilever spring of known stiffness ($\sim 2.4 \times 10^{-5}$ mN/m), which can be displaced vertically. Mica was chosen as the model for collector in porous media because it is a layered alumina-silicate mineral that can be cleaved along the basal plane <001> to yield a molecularly smooth surface of uniform thickness (here 2 to 3 μm) over large areas. Due to its atomic smoothness, mica is an ideal substrate for high-resolution force profile measurements of adsorption layers. It is noted that nanoscale roughness is prevalent in the subsurface and has been shown to affect ENP transport[113]. Nevertheless, the aim of our work is on better characterizing the force responsible for attachment for HA-coated surfaces. Importantly for studies of HA adsorption, the basal plane of mica has negatively charged lattice sites, similar in density to highly negatively charged silica or sand[159]. Mica surfaces were coated on one side with a 55 nm thick silver layer deposited by evaporation (Alfa Asear 99.99%). This layer permits the partial transmission of light directed normally through the surfaces, which constructively interferes and produces fringes of equal chromatic order (FECO) for surface separation determination.

Within two days of depositing the silver-coating, the surfaces were glued onto cylindrical lens and mounted into the SFA. Contact in air was measured. Afterwards, the SFA was filled with one of the three aqueous solutions and allowed to equilibrate for at least two hr for measurements in control solution and at least 24 hr for measurements in the -HA and -HA-Ca solutions in a temperature-controlled room at 25°C. Minimal hysteresis was observed between subsequent force profile measurements (compare approach and separation in Figure 2-1) indicating that the force measurements were carried out at essentially equilibrium conditions. Two configurations of silver-coated mica surfaces were used. In the symmetric configuration, the silver-coating faced the back of both surfaces to measure mica-mica forces. In the asymmetric configuration, the silver-coating faced the front of one surface and the back of the other surface to measure silver-mica forces. Determination of forces be-

tween the surfaces in a cross cylinder configuration was obtained from the deflection of the cantilever spring supporting the lower surface[58]. The distance between the surfaces (D) was measured by the position of FECO peak wavelengths within a spectrometer using a computer automated acquisition system. Final data obtained from the SFA consisted of force profiles as a function of separation distance between the two surfaces. The measured force between crossed cylinders was normalized by the geometric mean radius of curvature, R. At least two independent SFA experiments were carried out for each configuration and solution combinations tested. The results below show one representative data set, but replicates were consistent.

2.2.3 Interpretation of SFA data

Interacting Forces

The following describes the approach followed to separate the individual force contributions to the net force measured by SFA. Repulsive electrostatic double layer force, F_{EDL}/R contributions were determined for each experiment by numerically fitting the nonlinear Poisson-Boltzmann (NLPB) model to SFA data for $D > 10$ nm, where the interacting forces were purely electrostatic[160, 161]. The effective Debye length, κ^{-1}, was determined from the exponentially decaying force and compared to the expected κ^{-1} based on solution properties. Deviations enabled an estimate of HA's contribution to the system's overall electrostatics. Attractive van der Waals force, F_{VDW}/R, contributions were obtained from the control solution data, after subtracting the electrostatic force. The van der Waals attractive force is the same across all experiments of equivalent surface configuration. The Hamaker constant, A, for the silver-water-mica system was determined as[58]:

$$\frac{F_{VDW}}{R} = -\frac{A}{6D^2} \tag{2.3}$$

Additional repulsive force contributions from adsorption of HA were estimated as the residual after subtraction of both the fitted electrostatic and van der Waals forces (classic DLVO) from SFA measurements of the total interaction force profile.

Electrophoretic mobility values were collected on nanosilver suspensions matching the solutions described above using the ZetaPlus analyzer (Brookhaven Instruments Corp., Holtsville, NY). Ten measurements were collected for each sample, with replicate samples for each solution. Zeta-potentials (ζ) were determined from average electrophoretic mobilities using the Smoluchowski equation [162]. These values were compared to the surface potential data obtained from the SFA measurements.

2.3 Results and Discussion

2.3.1 Interaction forces

Control solution

Measured force profiles in the control solution (no HA) between opposing silver-mica (red markers) and mica-mica surfaces (grey markers) are shown in Figure 2-1. Classic DLVO surface forces are observed with long-range electrostatic repulsion and short-range van der Waals attraction. The adhesive contact of the surfaces in air was defined as $D = 0$ nm. We note that the mica-mica contact is well-defined for molecularly smooth surfaces. The mica-silver contact, however, was slightly compressible (i.e., the surfaces were elastically flattened upon compression), consistent with a surface roughness of~ 5 Å on the silver surface from evaporation deposition[163].

Electrostatic repulsion is captured by the NLPB model, whereby the boundary conditions of constant charge or constant potential describe the two extremes. Real systems lie somewhere in between due to charge regulation[161], as is shown in the inset of Figure 2-1. The control data more closely resemble a constant charge behavior (as described in the next section). The empirically determined effective κ^{-1} in the

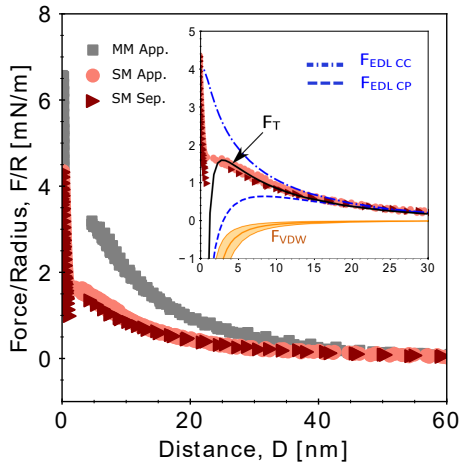

Figure 2-1: Force-distance profiles between opposing mica-mica (grey markers) and silver-mica (red markers) surfaces in the control solution. $D = 0$ nm is defined as the contact between the surface pairs. Inset shows the predicted electric-double layer at constant charge (F_{EDLCC}) and constant potential (F_{EDLCP}) boundary conditions, as well as van der Waals (F_{VDW}) contributions to the total force for the silver-mica experiments.

control solution was 14±0.3 nm, consistent with the expected value from solution properties (see Table 2.1). Semi-log plots showing κ^{-1} for each solution are shown in Figure S1.

Van der Waals attraction is obtained from data with the control solution, and is assumed to be the same across all experiments of equivalent surface configuration. The Hamaker constant for silver-mica interacting through water has a range of $A = [2.2, 6.4] \times 10^{-20}$ J, consistent with Lifshitz theory estimations of $A = 4.2 \times 10^{-20}$ J[164]. Uncertainty in A is reflected in the orange shaded region of van der Waals attractive forces shown in the inset of Figure 2-1. Both constant charge and constant potential fits to the data are shown. The best fit to the total profile is obtained with constant charge and $A = 4.3 \times 10^{-20}$ J (middle line in shaded region) as demonstrated by the solid line, F_T. The value of A was assumed constant across experiments based on refractive index measurements (data not shown), whose results were equivalent in

the control and HA-rich solutions.

-HA and -HA-Ca solutions

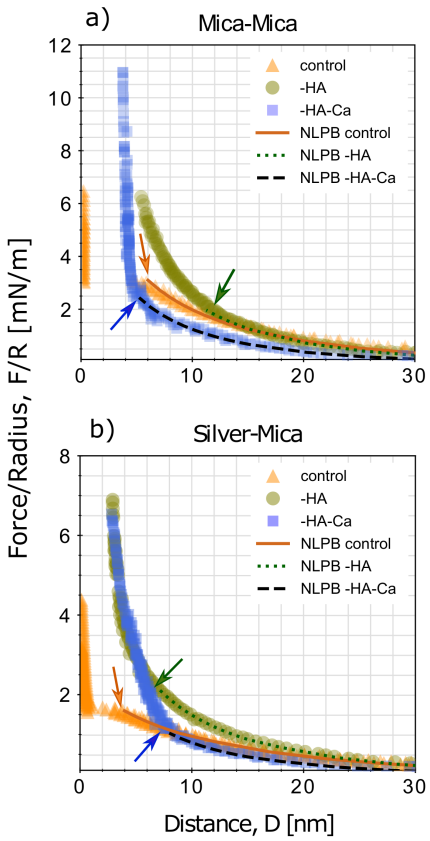

Figure 2-2: Force-distance profiles between opposing a) mica-mica and b) silver-mica surfaces. Markers correspond to the different solution conditions: control (orange triangles), -HA (green circles), and -HA-Ca (blue squares). Lines show the fit of the nonlinear Poisson-Boltzmann model at constant charge boundary conditions. Arrows indicate the onset of non-electrostatic force at short separation distances.

Measured force profiles in the -HA (green circles) and -HA-Ca (blue squares) solutions between opposing mica-mica and silver-mica surfaces are shown in Figure 2-2a and b, respectively. Generally, the force maximum is higher for the symmetric compared to the asymmetric system, signaling that HA adsorption on mica is greater

than on silver and that the solution composition impacts the adsorption behavior. Long-range electrostatic repulsion was well described by the NLPB model at constant charge boundary conditions (shown by the solid, dotted, and dashed lines for the control, -HA, and -HA-Ca solutions, respectively). Distances where deviation from a purely electrostatic interaction (arrows) denote the onset of repulsion due to adsorbed HA. We note that it was impossible to bring the surfaces into contact ($D = 0$ nm) due to the HA adsorption layers and hydrating water. Importantly for both solutions, short-range van der Waals attraction is masked by the overwhelming net repulsive forces imparted by electrostatics and adsorbed HA. This is discussed in greater detail below. The effective κ^{-1} (see Table 2.1) for -HA was 2 nm lower than for the control solution and its expected value, signifying an increase in IS due to a release of ions from charged HA functional groups. Similarly, for -HA-Ca the effective κ^{-1} was lower than its expected value. The effective IS in solutions containing HA was ∼0.16 mM higher than was expected (from only added salt), accounting for the ions released from HA. It should be noted that released ions from HA affect electrostatics in non-negligible ways, therefore the effective IS should be considered in DLVO calculations, particularly in low IS solutions.

2.3.2 Surface potential

Surface potential measurements for all tested treatments, shown in Table 2.1, reveal that silver and mica surfaces are very highly charged ($\psi_0 = [-45, -130]$ mV, respectively) and require estimation of electrostatic interactions by NLPB, rather than well-known analytical approximations to DLVO theory (e.g. Hogg et al.[165], Wiese and Healy [166], Bell et al. [167]) that assume low potential ($|\psi_0| < 25$ mV). Estimated ψ_0 values in the control solution, in the absence of HA, are in agreement with values reported in the literature. ψ_0^M = -110 mV for mica is within the range reported by Israelachvili, (1978) [160] of [-50, -130] mV, while ψ_0^S = -50

Table 2.1: Summary of charge and adsorbed layer properties for silver and mica surfaces at each tested solution composition. κ^{-1} is the Debye length, ψ_0 is the surface potential, ζ is the zeta-potential, L is the uncompressed adsorbed HA layer thickness, λ is the layer's compressibility, and Γ is the estimated mass of adsorbed HA. The sub- and superscripts indicate the surface type as mica (M) or silver (S).

Parameter		Solution composition		
		Control	-HA	-HA-Ca
κ^{-1} expected	[nm]	13.5	13.5	11.1
κ^{-1} effective	[nm]	14±0.3	12±0.2	10±0.8
IS expected	[mM]	0.5	0.5	0.75
IS effective	[mM]	0.47	0.64	0.92
ψ_o^M	[mV]	-110±10	-130±20	-80±10
ψ_o^S	[mV]	-50±5	-60±5	-45±5
ζ_S *	[mV]	-52±4	-61±3	-44±3
L_M	[nm]	0	5.5	2.4
L_S	[nm]	0	0.5	4.4
λ_M	[%]	0	48.8	14.5
λ_S	[%]	0	53.8	66.0
Γ_M	[mg/m^2]	0	2.24	2.24
Γ_S	[mg/m^2]	0	0.18	1.19

* Values measured for 100 nm silver nanoparticles.

mV for silver is consistent with reported zeta-potential measurements of silver colloids and nanoparticles[168, 169], including our own collected values (see ζ_S in Table 2.1). Excellent agreement between SFA-determined ψ_0 and ζ-potential measurements demonstrates the statistical equivalence between the two methods. For the -HA solution, adsorption of negatively charged HA moieties onto silver and mica surfaces resulted in more negative ψ_0 relative to experiments in the control solution. Adsorption of polydisperse macromolecules onto like-charged surfaces in the presence of monovalent ions has been reported before[170, 171]. We propose that the major mechanisms of adsorption in the -HA solution are charge screening by $NaNO_3$, and attractive interactions between cations adsorbed on the negatively charged surfaces and the aromatic moieties in HA. The cation-π interaction is well recognized as an

intermolecular, non-covalent attraction (including a substantial electrostatic component) between cations and aromatic π-systems, and it is comparable in strength to hydrogen bonding[172, 173]. For the -HA-Ca solution, ψ_0 on both surfaces was more neutral compared to the -HA solution. In this case, Ca^{+2} neutralized some functional groups by forming coordination complexes with ligands (e.g., HA, silver and mica surfaces)[76]. In both HA-containing solutions, the relative change in ψ_0 was larger on mica, which is more negatively charged than silver.

2.3.3 Magnitude and origin of non-electrostatic repulsive forces

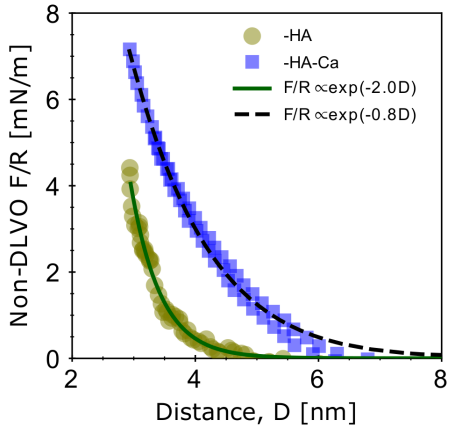

Figure 2-3: Non-DLVO force-distance profiles between opposing silver-mica surfaces in -HA (green circles) and -HA-Ca (blue squares) solutions. Solid and dashed lines show the exponential decay of the repulsive forces with distance.

Quantitative evidence of non-electrostatic repulsive forces are presented in this section. To verify that SFA measurements can be used to discern individual surface force contributions, we first presented evidence that total force, F_T, in the control solution was captured by the summation of F_{VDW} and F_{EDL} alone (see F_T in inset of Figure 2-1). The total force in HA-containing solutions, however, shows that an additional repulsive force (generally considered of steric origin in the literature[69, 65, 162]) significantly contributes toward F_T. To determine the steric contribution from the adsorbed HA layers, the F_{VDW} and the fitted F_{EDL} were subtracted from F_T. It

is noteworthy that the presence of HA adsorbed layers prevented the surfaces to come into contact as defined from the control solution ($D = 0$). Moreover, the minimum separation distance for -HA and -HA-Ca solutions was the sum of the compressed layers on each surface–that is $2L'_M$ for the symmetric system and $L'_M + L'_S$ for the asymmetric system. At such separations, VDW interactions between the surfaces were essentially negligible. Figure 2-3 shows the magnitude of the remaining non-electrostatic repulsive force in -HA and -HA-Ca solution conditions for the asymmetric mica-silver system. It is evident that this non-DLVO force decays exponentially with distance, with average rates of $\sim$ 2.0 and 0.8 nm^{-1} for -HA and -HA-Ca solutions, respectively. The faster decay rate for the -HA solution, compared to the -HA-Ca case, is consistent with the thinner but denser total adsorbed layer ($L_M + L_S$) in the former solution[174].

Certainty in the origin for each contributing surface force is necessary to make predictions of colloidal interactions in HA-rich systems that cannot be measured directly by, for example SFA. Modeling approaches for calculating the structural forces brought about from HA sorption have been heavily based on soft particle theory (SPT)[68, 175, 65]. However, SPT requires three key conditions are met: the adsorbed macromolecules must be composed of many repeating subunits ($> \mathcal{O}(10^2)$), polydispersity of the polymer must be low, and $L >> \kappa^{-1}$. According to our measurements, none of these conditions are satisfied for HA adsorption layers on mica or silver. First, the molecular structure of HA is highly variable, making it unlikely that the adsorbed macromolecule assembles into long chains of at least hundreds of identically repeating units. Second, the polydispersity of HA is relatively high (1.76 - 2.5)[176, 177]. Highly polydispersed materials display a complex interplay between adsorption and configurational entropy. While larger molecules diffuse and equilibrate more slowly onto the surfaces, their adsorption results in a more pronounced decrease in the interfacial energy and is thus favored at longer times[178, 179]. Third,

in all cases tested in this study $L < \kappa^{-1}$ by at least a factor of two, indicating that elastic-steric repulsion is negligible compared to osmotic-steric repulsion for HA. All together, these considerations suggest that Ohshima's soft particle theory is not appropriate for describing repulsive forces imparted by adsorbed HA. In sections following, we present quantitative evidence for the osmotic origin of extra repulsive forces in HA-rich systems.

2.3.4 Adsorbed layer properties

Experimental properties regarding adsorbed layer characteristics for each surface and solution tested are summarized in Table 2.1. In the control solution conditions, surfaces were bare and all adsorbed layer properties are reported as zero.

Layer thickness and compressibility

Uncompressed adsorbed HA layer thickness, L, was determined by the distance where the force profile measurements deviated from the NLPB fit, as indicated by the arrows in Figure 2-2. The compressibility of the HA layers, λ, was estimated as $\lambda = (L - L')/L \times 100$, where L' is the compressed layer thickness at a separation distance recorded for an applied force of 6 mN/m. At this range, an increase in applied force did not change the separation distance by more than 1 nm. The symmetric configuration was used to estimate HA layer thickness on one mica surface as $L/2$ in each solution. The asymmetric configuration then provided the layer thickness on the silver surface by subtracting the known thickness of the layer on mica from the measured L of the system. The same logic was used for the estimation of λ. Here, we interpret λ as a proxi of the density of the adsobed layer.

All measured uncompressed adsorption layers between approaching surfaces were thinner than the solution κ^{-1}. This facilitated fitting the system's electrostatics, which are dominant at $D > 10$ as $L < 7$ nm. By subtracting electrostatics and van

der Waals from the total force profile, we distinguish the steric contribution from the adsorbed HA layers. For -HA solution conditions, the adsorbed layer on mica, L_M, was an order of magnitude thicker than that on silver, L_S. In this solution, the compressibility of the adsorbed layers on silver and mica λ_S and λ_M, respectively, was close to 50%, suggesting an intermediate layer density that is independent of the substrate. For -HA-Ca solution conditions L_M and λ_M were reduced, implying an increase in the HA layer density on mica, while L_S and λ_S increased, indicating that the layer on silver in presence of calcium was thicker and more diffuse that the one on mica. At this solution, L_M and L_S were in the same order of magnitude.

Mass adsorbed

Mass of HA adsorbed per unit surface area was obtained through the expression $\Gamma = \rho_{HA}\phi L'$. ρ_{HA} is the HA density taken as 1.45 g/ml[180]. $\phi = 0.55$ is the volumetric fraction of HA to the solvent, from direct measurements of similarly polydispersed polymers in a good solvent at $F/R \sim 6$ mN/m[181]. Substantial differences in mass of adsorbed polymer per unit area, Γ, were observed across solution conditions. For the -HA solution, Γ_M was an order of magnitude greater than Γ_S. Our estimate for Γ_M is in agreement with the report by Taunton et al.,(1990) [182] for high molecular weight polymer adsorption onto mica in good solvent conditions. Our estimate for Γ_S, however, was considerably lower than values reported elsewhere[69]. For the -HA-Ca solution, Γ_S significantly increased, suggesting that Ca^{+2} counterions promote adsorption of negatively charged HA onto like-charged silver[183]. We point out that the value for Γ_M in -HA-Ca reported in Table 2.1 is different from what was determined based on this parameter's definition ($\Gamma_M = 1.54$ mg/m^2). This original calculation would imply that desorption of HA happened in the presence of Ca^{+2}. We know this result to be incorrect. Rather, Ca^{+2} is expected to enhance HA adsorption and, most importantly, to increase the density of the existing adsorbed

layer. Investigating the nature of this discrepancy is beyond the scope of this work, so we instead report the estimated value for Γ_M from -HA solutions again.

2.3.5 Deposition of silver nanoparticles in HA-rich porous media

Nanoparticle deposition on mica-like porous media at the solution conditions relevant to this study was investigated by estimations of the system's attachment efficiency, α, from colloid filtration theory (CFT). α is a kinetic transport parameter widely used to quantify the probability of a particle attaching to a soil grain after collision. To determine the best model for estimating α in each solution composition, it was first necessary to properly account for the different force contributors to the net interaction that describes the system. Here, we demonstrate that the interplay of the osmotic, electric double layer, and van der Waals forces is sufficient to capture the measured interactions.

Interaction energy translation

In environmental engineering applications, it is standard to employ energy of interaction profiles to justify deposition trends of colloids/nanoparticles transported in porous media. We used Derjaguin's approximation[184] to translate the force profiles between cross-cylinders of silver-mica surfaces from SFA measurements, F/R, into energy of interaction, W, between hypothetical cases of silver nanoparticles and mica collectors, viz:

$$W(D) = -\frac{R_S R_M}{R_S + R_M} \int_{\infty}^{D} \frac{F}{R} dD'. \tag{2.4}$$

Here, R_S and R_M correspond to the radii of the (silver) nanoparticle and the (mica) collector, respectively. The translated profiles are considered empirical data for var-

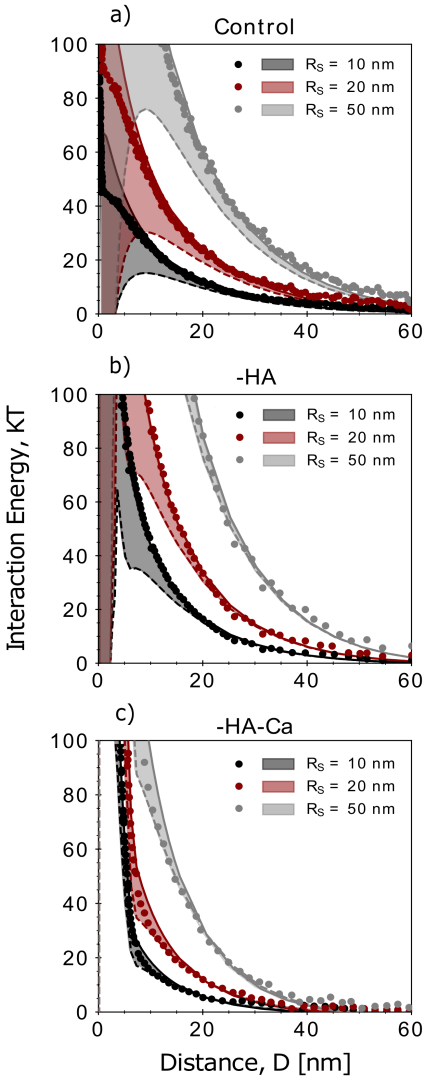

Figure 2-4: Total energy profiles ($W_T = W_{EDL} + W_{VDW} + W_{OSM}$) for interactions between silver particles and mica collectors in a) control, b) -HA, and c) -HA-Ca solutions. Shaded regions show the model predictions with upper and lower limits for electrostatics corresponding to constant charge (solid line) and constant potential (dashed line), respectively. Empirical data (translated from SFA force measurements) is shown as symbols.

ious scenarios of nanoparticle sizes. Furthermore, these data are used to gauge the relative effect of adsorbed HA on the energy of interaction between collectors and nanoparticles of different sizes.

To complement the empirical data, theoretical estimations of the total energy of

interaction, W_T, are provided with an extension to classic DLVO theory to account for osmotic repulsion[185] as per the following.

$$W_T = W_{EDL} + W_{VDW} + W_{OSM} \tag{2.5}$$

$$W_{VDW} = -\left(\frac{R_S R_M}{R_S + R_M}\right)\frac{A}{6D} \tag{2.6}$$

$$W_{EDL} = \left(\frac{R_S R_M}{R_S + R_M}\right)\frac{2\pi}{\kappa}\text{NLPB} \tag{2.7}$$

$$W_{OSM} = \begin{cases} 0 & D \geq 2\bar{L} \\ \left(\frac{R_S R_M}{R_S+R_M}\right)\frac{2\pi}{\nu_1}\Phi_S\Phi_M\left(\frac{1}{2}-\chi\right)(\bar{L}-\frac{D}{2})^2 & \bar{L} \leq D < 2\bar{L} \\ \left(\frac{R_S R_M}{R_S+R_M}\right)\frac{2\pi}{\nu_1}\Phi_S\Phi_M\left(\frac{1}{2}-\chi\right)\bar{L}^2\left(\frac{D}{2\bar{L}}-\frac{1}{4}-ln\left(\frac{D}{\bar{L}}\right)\right) & D < \bar{L} \end{cases} \tag{2.8}$$

We consider R_S = 10, 20, and 50 nm for different particle size scenarios. W_{EDL} was determined by numerically solving the Poisson-Boltzmann equation since the surface charges exceeded the validity of well-knonwn analytical approximations for electric double layer energies. It should be noted that the set of expressions for W_{OSM} is adapted from an approximation for a symmetric system (Peter Kralchevsky, personal communication, 18 March 2020). Here, ν_1 is the volume of a solvent (water) molecule, χ is the Flory-Huggins solvency parameter, $\bar{L} = (L_M + L_S)/2$ is the average adsorbed layer thickness, and Φ_S and Φ_M are the volume fraction of the adsorbed HA layer onto silver and mica spheres, respectively, and calculated as:

$$\Phi = 3\frac{\Gamma R^2}{\rho_{HA}[(L+R^3)-R^3]}. \tag{2.9}$$

Figure 2-4 shows very good agreement between model predictions for W_T (shaded region marking the boundary condition limits for constant charge and constant potential) and the empirical data (markers) under all particle sizes and all solution

conditions. In estimating W_{OSM}, χ was treated as a free model parameter and ρ_{HA} was fixed at 1.45 g/cm^3 (a parameter the model was not sensitive to). It is worth noting that the peaks at $D \sim 4$ nm in model predictions for -HA solutions are due to the large difference between L_M and L_S. This discrepancy creates a discontinuity in the individual expressions for W_{OSM}, which is indistinguishable for the -HA-Ca solutions where L_M and L_S are within the same order of magnitude. The higher limit on the y-axis was fixed at 100 kT since higher energy barriers are considered insurmountable with the particles kinetic energy. The complete energy profile is shown in Figure S2. From this, it is evident that classic DLVO is insufficient to describe the system and that an osmotic contribution captures well the physics of the additional repulsion imparted by HA adsorption. Two notable trends are evident in Figure 2-4. First, the net energy of interaction scales with particle size, implying that inaccuracies in the modeled interaction energy are magnified with increasing particle size. Second, the energy barrier increases manyfold with solution composition complexity. That is, W_T^{max} for control $<$ -HA $<$ -HA-Ca, making it imperative to ascertain the origin of non-DLVO forces in complex solutions. Estimations of the elastic-steric component of steric-type forces[65] did not significantly contribute to the interaction profile and were confirmed negligible. As an additional reference, Figure S3 shows an equivalent comparison for predictions that considering only van der Waals and electrostatic energies, illustrating the need to include an additional osmotic force contribution.

Attachment efficiency

CFT is commonly employed to describe transport kinetics of particle deposition in porous media in dimensionless terms from breakthrough data. Various semiempirical correlations have been proposed to estimate the attachment efficiency, α, of colloidal suspensions colliding with simplified porous media[135, 136, 137, 69]. However, there is no widely accepted unified mechanistic model for predicting α under *unfavorable*

deposition conditions (i.e., with energy barriers high enough to prevent particle attachment). In the following, we employ the proposed correlation equation for bare electrostatically stabilized particles from Bai & Tien (1996)[136] to predict the attachment efficiency of nanoparticle suspensions in the control solution (α_{bare}). Similarly, we use the correlation equation for surface-coated electrosterically stabilized particles from Phenrat et al. (2010)[137] to predict the attachment efficiency of nanoparticles in the -HA and -HA-Ca solutions (α_{coat}). Details about α calculations are provided in the SI.

Predictions for α corresponding to the interaction energy profiles in the previous section are shown in Figure 2-5. The results are in qualitative agreement with experimental α values resulting from transport tests of silver nanoparticles suspensions in monovalent salt, in presence of HA, and, in solutions containing HA and divalent cations[186, 187, 188]. It is evident that α increases monotonically with particle size in both bare and surface-coated model correlations. For particles of equivalent size, α_{bare} was much larger than α_{coat} at $\mathcal{O}(10^{-2})$ and $\mathcal{O}(10^{-4})$, respectively. This is consistent with the lowest energy barrier found ($\mathcal{O}(10^1 - 10^2)$kT, see Figure S1) for the control solution, where only electrostatics create unfavorable conditions. Similar values for α_{coat} were found for particles of equivalent size in solution conditions that promote surface coatings. Efficiencies in -HA were slightly smaller than those in -HA-Ca solutions, which cannot be explained by trends in the energy barrier magnitude. At $\mathcal{O}(10^2 - 10^3)$kT (see Figure S1). Simply, the energy barrier afforded by adsorbed HA macromolecules is equally insurmountable in -HA as in -HA-Ca solutions. We propose that differences in α_{coat} are better attributed to the secondary energy well, which is entirely absent for -HA solutions and present for -HA-Ca with a deep enough minimum deeper than 5 kT) for particles $R_S \geq 50$ nm. This implies that within the geometry of porous media, retention in secondary energy minima in the presence of an insurmountable energy barrier would likley cause particles to accumulate at

grain-to-grain contacts[93]. Despite the reasonable agreement found between our authenticated energy of interaction profiles and the predictions for α, additional work is needed to i) confirm that elastic forces are negligible for a broader range of DOM conditions than those tested here, and if confirmed ii) revise the correlation for α_{coat} to give greater importance to the osmotic component over the elastic one for steric repulsion.

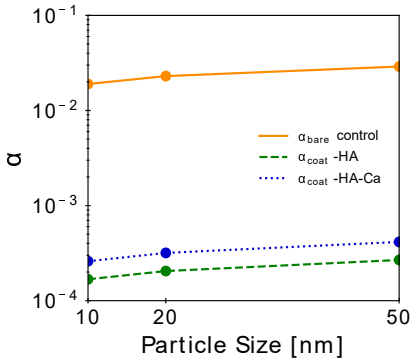

Figure 2-5: Estimated attachment efficiency, α, for suspensions of variably sized particles colliding with simplified porous media at different solution conditions. Solid line considers the dimensionless semi-empirical correlation for electrostatically stabilized suspensions (without surface coatings) from Bai & Tien (1996)[136]. Dashed lines consider the correlation for electrosterically stabilized suspensions (afforded by adsorbed macromolecules) from Phenrat et al. (2010)[137].

2.3.6 Technical and environmental implications for colloid transport

This work investigated the surface interactions between charged silver and mica substrates in various solution compositions relevant to agricultural soils. We confirmed that in the absence of HA, the forces at play are electrostatic repulsion and van der Waals attraction. Once the surfaces are exposed to DOM, macromolecules like HA readily adsorb onto both materials. However, important differences on the adsorbed layers were found. On mica, the HA layer was thicker, more charged, and more dense than the one observed on silver. Additionally, changes in the effective solution IS

from ionization of the HA moieties were detected, which affect the overall system's electrostatics. When the solution complexity was increased by including calcium ions, the differences in adsorbed layer thickness and charge between mica and silver were reduced. The data indicate that calcium ions promote a greater adsorbed mass and increase the HA layer thickness for silver, but increase the HA layer density for mica.

Our measurements suggest that HA has the potential to influence the deposition of n-Ag particles onto soil grains in three key ways: i) by changing the electrical double layer forces; ii) by creating a physical barrier between particles and collectors; and, iii) by generating additional interactions due to compression of the HA adsorbed layers, as reflected in the measured force profiles and estimated energy profiles. Based on our calculations, the probability of particle deposition (α) is expected to be the lowest in HA-rich solutions, relative to the other solutions tested. In order to extend the use of the CFT to model ENPs filtration in HA-rich solutions, the osmotic repulsion arising from the overlap of adsorbed HA layers must be considered in addition to electrostatic and van der Waals interactions (classic DLVO theory). Because HA and other DOM macromolecules are ubiquitous in soil, and especially in agricultural soils, these results imply that HA-coated ENPs may travel much farther than their bare counterparts, potentially reaching sensitive water resources. The authors recognize that the combined effect of adsorbed natural macromolecules[186, 188], heterogeneity of the soil surface that creates favorable microsites for deposition[189, 190, 191, 112], and heteroaggregation[192, 193] may reduce the expected travel distances of ENPs. Nonetheless, our study demonstrates that osmotic repulsion from adsorbed DOM onto suspensions and collectors is the main factor controlling interactions between ENPs and soil surfaces, and consequently their probability for deposition. Precise characterization of the relevant surface coating properties on natural and engineered materials is a first step towards improving the accuracy of predictive models for colloid transport in the subsurface.

Acknowledgement

This work was funded in part by the U.S. NSF (EAR-1847689), the Hellman Fellowship, and the P.E.O. International Peace Scholarship. Acknowledgment is made to the Donors of the American Chemical Society Petroleum Research Fund (59864-DNI9 and 59-483-ND5) for partial support of this research.

Supporting information

S2-1. Debye length from force measurements

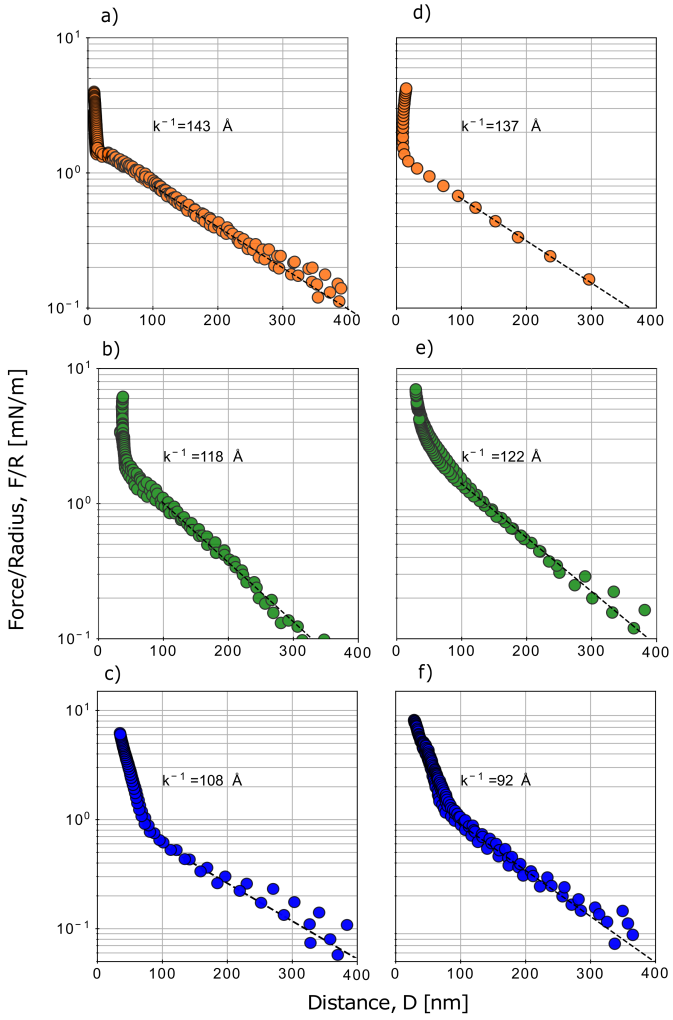

Figure S2-1: Force-distance profiles between opposing silver mica-surfaces in a) control solution, b) -HA solution and c) -HA-Ca solution. Dashed line indicates the exponential fit of the electrostatic forces, which decay corresponds to the Debye length, κ^{-1}. Replicates of the experiments are presented in figures d), e) and f).

S2-2. Energy predictions based on xDLVO

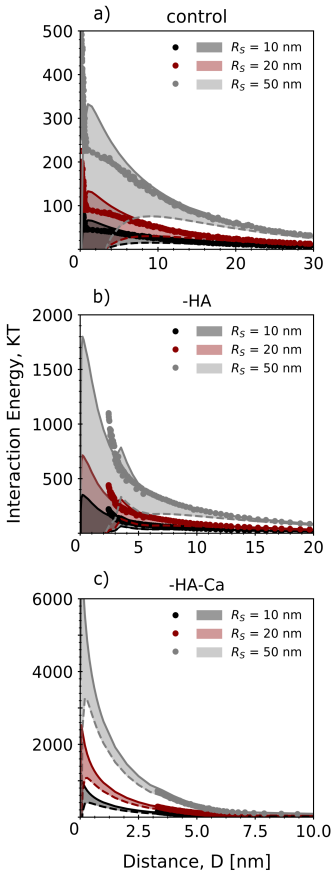

Figure S2-2: Total energy profiles ($W_T = W_{EDL} + W_{VDW} + W_{OSM}$) for interactions between silver particles and mica collectors in a) control, b) -HA, and c) -HA-Ca solution conditions. Shaded regions show the model predictions with upper and lower limits for electrostatics corresponding to constant charge (solid line) and constant potential (dashed line), respectively. Empirical data (translated from SFA force measurements) is shown as symbols.

S2-3. Energy predictions based on DLVO

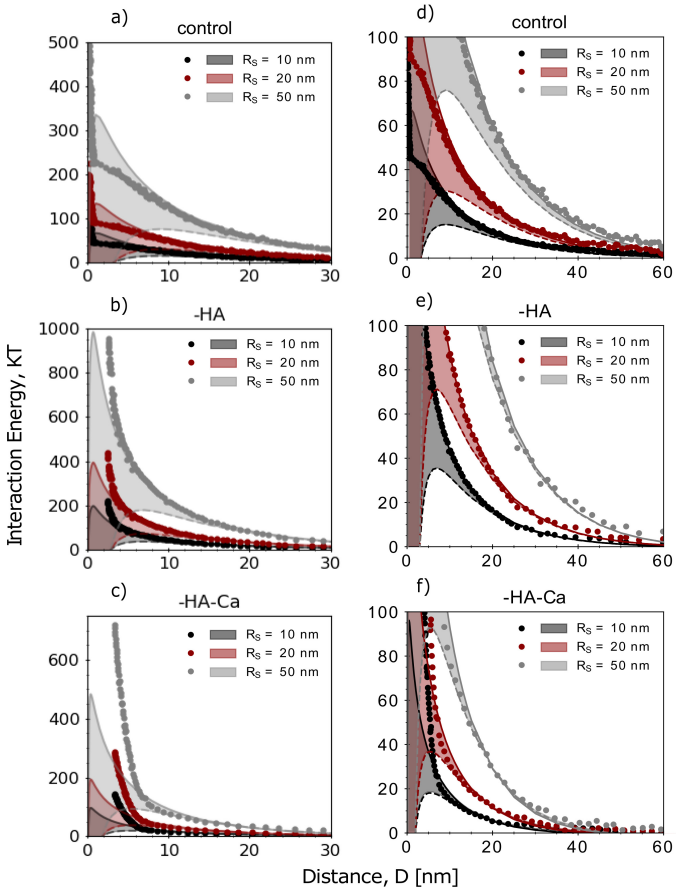

Figure S2-3: Total energy profiles ($W_T = W_{EDL} + W_{VDW}$) for interactions between silver particles and mica collectors in a) control, b) -HA, and c) -HA-Ca solution conditions. Shaded regions show the model predictions with upper and lower limits for electrostatics corresponding to constant charge (solid line) and constant potential (dashed line), respectively. Empirical data (translated from SFA force measurements) is shown as symbols. The same data with different limits in the x and y axis are presented in subplots d), e) and f) for direct comparison with Figure 4.

S2-4. Attachment efficiency, α, calculations

$$\alpha_{bare} = 2.527 \times 10^{-3} N_{LO}^{0.7031} N_{ES}^{-0.3121} N_{ES2}^{3.5111} N_{DL}^{1.352} \tag{S2-1}$$

$$\alpha_{coat} = 10^{-1.35} N_{LO}^{0.39} N_{ES}^{-1.17} N_{LEK}^{-0.10} \tag{S2-2}$$

The dimensionless numbers are listed in Table S2-1.

Table S2-1: Dimensionless numbers for α calculations

Parameter	Definition	
N_{LO}	$\frac{A}{9\pi\mu R_S^2 u_s}$	London van der Waals number
N_{ES}	$\frac{\epsilon\epsilon_0(\zeta_p^2+\zeta_c^2)}{12\pi\mu R_S^2 u_s}$	First electrokinetic parameter
N_{ES2}	$\frac{2\zeta_p\zeta_c}{\zeta_p^2+\zeta_c^2}$	Second electrokinetic parameter
N_{DL}	$2\kappa R_S$	Double-layer force parameter
N_{LEK}	$\frac{2R_S\bar{L}^2 u_s \Gamma N_a \rho_H A}{\mu M_w}$	Layer-electrokinetc parameter

where A is the Hamaker constant, μ is the water viscosity, R_S is the particle radius, u_s is superficial velocity, ϵ is relative permittivity of the fluid, ϵ_0 is permittivity in a vacuum, ζ_p and ζ_c are zeta-potential of the particles and collectors respectively, κ is the inverse of the debye length, L is the polymer layer thickness, Γ is the mass of adsorbed polymer per unit area, $\rho_H A$ is the polymer density and M_w is the polymer molecular weight.

Retention Site Contribution towards Silver Particle Immobilization in Porous Media[b]

Janis E. Patiño[1], Francisco J. Pérez-Reche[2], Verónica L. Morales[1]

[1] Department of Civil and Environmental Engineering, University of California, Davis

Davis, United States

[2] School of Natural and Computing Sciences, University of Aberdeen

Aberdeen, United Kingdom

Abstract

This work investigates the role that pore structure plays in colloid retention across scales with a novel methodology based on image analysis. Experiments were designed to quantify–with robust statistics–the contribution from commonly proposed retention sites toward colloid immobilization. Specific retention sites include solid-water interface, air-water interface, air-water-solid triple point, grain-to-grain contacts, and thin films. Variable conditions for pore-water content, velocity, and chemistry were tested in a model glass bead porous medium with silver microspheres. Concentration signals from effluent breakthrough and spatial profiles of retained particles from micro X-ray Computed Tomography were used to compute mass balances and enumerate pore-scale regions of interest in three dimensions. At the Darcy-scale, retained colloids follow non-monotonic deposition profiles, which implicates effects from flow-stagnation zones. The spatial distribution of immobilized colloids along the porous medium depth was analyzed by retention site, revealing depth-independent partitioning of colloids. At the pore-scale, dominance and overall saturation of all retention

[b]This chapter has been published as: Patiño, J. E., Perez-Reche, F. J., & Morales, V. L. (2022). Retention Site Contribution towards Silver Particle Immobilization in Porous Media. Water Resources Research, e2021WR031807.

sites considered indicated that the solid-water interface and wedge-shaped regions associated with flow-stagnation (grain-to-grain contacts in saturated and air-water-solid triple points in unsaturated conditions) are the greatest contributors toward retention under the tested conditions. At the interface-scale, xDLVO energy profiles were in agreement with pore-scale observations. Our calculations suggest favorable interactions for colloids and solid-water interfaces and for weak flocculation (e.g., at flow-stagnation zones), but unfavorable interactions between colloids and air-water interfaces. Overall, we demonstrate that pore-structure plays a critical role in colloid immobilization and that Darcy-, pore- and interface-scales are consistent when the pore structure is taken into account.

3.1 Introduction

The expanding use of engineered colloids in the manufacturing of medical and electrical appliances, textiles, paint protecting coverings, and consumer products has led to the accumulation of undesirable amounts of nano- and micro-size particles in the environment [29, 117, 25, 118]. Of particular interest are silver particles, employed in the fabrication of detergents and anti-odor clothing because of their biocidal properties [119, 120, 121, 194]. Studies up to date have demonstrated that a large proportion of colloidal silver can enter sewers and the wastewater treatment train via erosion during silver-impregnated textile washing [25, 23]. Furthermore, silver particle surfaces likely acquire a coating of surfactants [30, 195, 196] and dissolved organic matter [122, 65] along the sewer pathway, which increases the stability and persistence of the suspension. This raises concerns regarding the detrimental environmental and public health impact that stabilized antimicrobial silver-laden effluent and sludge may have on soil and aquatic systems where they are discharged [23, 25, 122, 123, 126, 127, 32, 197]. Regarding environmental health concerns, studies on soil microbial toxicity observed adverse effects on microbial growth, functions and diversity in soils, which became more pronounced over time [198, 199, 200]. Regarding public health concerns, reports on the oral toxicity of silver colloids suggest that mammals may experience dose-dependent altered neurotransmitter levels and immunological effects [201, 202],

and that the toxicity of silver particles increases with decreasing size [203]. A sound understanding of the underlying physics that govern spreading and retention of micro and nano-particles in porous media is necessary to improve the accuracy of mechanistic models that describe their transport. Such models are necessary for anticipating and ultimately preventing soil and groundwater contamination by engineered materials.

Macroscopic transport and retention of colloids is measured as deposited mass along the porous medium depth (depth profiles, DP) and/or concentration signals in the effluent (breakthrough curves, BT). Traditionally, these signals are described with mathematical models based on Colloid Filtration Theory (CFT). A classical view predicts exponentially decreasing DP from clean bead and first-order deposition kinetics assumptions [46]. Deviations from CFT have been frequently observed in the presence of repulsive interactions between particles and collectors (unfavorable conditions). Particularly, underestimation of the mass of immobilized particles [84, 104]. Particle retention under unfavorable conditions has been ascribed to deposition in secondary energy minimum [61], surface roughness [88, 204], concurrent favorable and unfavorable interactions between colloids and the porous media surface [84], and surface charge heterogeneity [53, 189, 205]. Anomalous DP behavior is common and is often associated with unique pore-scale retention mechanisms [206]. Hyperexponential DP have been explained by colloid straining in narrow pore spaces in addition to attachment to the soil-water interface [91, 105]. Uniform DP are thought to be controlled by blocking phenomena, where deposited particles prevent further colloid deposition [106, 107]. Non-monotonic DP are associated to colloid accumulation at low-flow regions [108, 109] and to size-dependent deposition of polydisperse suspensions [110]. Monotonically increasing DP have been attributed to colloid-induced charge redistribution on the collectors (Chen et al., 2011). While variations to traditional CFT-based models have been successfully implemented to capture a subset

of non-exponential DP behaviors [207, 111], as of yet, information on the pore structure (including locations where multiple interfaces meet) is not yet implemented in such modeling approaches. Thus, sound evidence is lacking to confidently pair the pore-scale mechanisms represented in the models with the DP behavior they produce. High resolution X-ray computed tomography (XCT) has recently gained traction to address aspects of this knowledge gap [108, 208, 209].

Microscopic variations in colloid retention occur largely as a result of the pore space geometry and its established flow field [4, 210]. CFT employs a first approximation of the mass transfer rate between suspended and arrested particles by upscaling an assumed perfect sink at the solid-water (SW) interface [46]. Nevertheless, the forces and torques that act on colloids near contact points where multiple interfaces meet are fundamentally different from those acting on a single interface [211, 98, 212]. Experimental observations (by various microscopic techniques) of colloid transport and deposition at the pore-scale have provided valuable insight on particle retention in locations other than the SW. Notable examples include: straining in too narrow pores [91, 4, 105, 213], accumulation in flow stagnant grain-to-grain contacts (GG) [108, 214, 82, 215], attachment to the air-water (AW) interface [216, 42, 217], pinning at the air-water-solid triple point (AWS) [218, 89, 43, 219, 88, 220], and film straining in thin films of water (TF) adjacent to solid surfaces [95]. While this evidence highlights the relevance of pore space structure, it is not possible to determine the contributing weight of alternative retention sites from observations in a handful of pores located at the boundary of the transport experiment device. Assessing the significance of various contending pore-scale processes warrants statistical analysis from observations in numerous pores *within* the porous medium.

Nanoscopic interactions between colloids and the individual surfaces present in porous media are traditionally modeled by Derjaguin-Landau-Verwey-Overbeek (DLVO) theory. In principle, these surface interactions control the attachment efficiency–and

consequently the deposition rate–in CFT models. Yet, a formal relationship between the two has not been established [65, 76]. In DLVO theory, the total energy of interaction is given by the sum of van der Waals attraction (VDW) and electronic double layer repulsion (EDL) [56, 57]. Extended versions of DLVO (xDLVO) include additional interactions affected by complexity of the solution chemistry and presence of air bubbles [15, 66]. Furthermore, the occurrence of chemical heterogeneities and roughness on any of the approaching surfaces can significantly modify their interfacial interactions [207, 82, 221]. Relevant xDLVO interactions to this work include: charge screening from changes in ionic strength, which affect the EDL [15, 222, 223]; steric interactions (ST) from surface adsorption of naturally occurring dissolved organic matter [15, 224, 225, 65, 69, 76, 208, 197]; polar or Lewis acid-base interactions (AB) from the electron-acceptor and electron-donor nature of the two approaching materials [226]; and hydrophobic interactions (HYD) between the particles and air bubbles under unsaturated conditions [227, 228, 66]. While substantial progress has been made to account for the pertinent colloidal interactions in typical groundwater systems, relating these surface energetics to pore-scale and Darcy-scale observations is not straight forward. This is mainly because during the process of deposition, particles interact with multiple planes simultaneously rather than the single infinite flat plane modeled in the theory. To the authors' knowledge, development of a theory that accounts for multi-plane energies of interaction is still an open research question.

The principal focus of this study is to provide a better understanding of the mechanisms of colloid retention in porous media that is in agreement across interface-, pore-, and Dacy-scales. Our first aim is to statistically evaluate the contribution of alternative retention sites, beyond the SW, toward particle retention under commonly found environmental conditions. The intent of the present work is to perform an efficient rather than a systematic assessment of the effects of mean pore velocity, saturation, and solution chemistry on the pore-scale locations where particles become immobi-

lized. Our second aim is to assess the impact that dominant retention sites have at other scales of interest in order to justify its consideration in down-/up-scaling modeling efforts. To do this, we determine the spatial distribution of retained colloids from transport experiments that are imaged non-destructively by high resolution X-ray Computed Tomography (XCT). The experimental setup was designed to work with a model porous medium to isolate the role that pore structure plays on filtration. Analyses of the spatial maps are used to simultaneously assess the macroscopic behavior at play, as well as the dominance and saturation of individual retention sites for all pores within the sample. Finally, theoretical particle interactions from xDLVO are used to qualitatively rationalize the observed retention trends.

3.2 Materials and Methods

3.2.1 Materials

Custom made hollow glass microspheres coated in a layer of 118 nm silver were used as the silver colloids for experimentation (Microsphere Technology, Limerick, IE). According to the manufacturer, the silver-glass-air spheres have a mean diameter of 14±4 μm and a density of 1000 g L^{-1}. Similar particles have been used in previous studies to investigate colloid retention specifically at grain-grain contacts [108] and biofilm distribution in porous media [229]. Suspensions of 20 g L^{-1} were prepared in the desired background aqueous solution (described below) and used in experiments within 10 hours. Concentrations of metallic silver in waste water are usually below 5 mg L^{-1} [230]. Nonetheless, silver particles are expected to accumulate over time in environmental compartments [194], especially with continual application of the nanomaterial source. Metallic silver nanoparticles (Ag-NP) in consumer products have sizes that range between 10 and 100 nm [122, 231, 230], which are smaller than the microspheres used in our experiments. This modification in concentration and

particle size from expected values of slude-receiving soils was required for visualization of deposited material with X-ray computed tomography, as described in section 2.3.

Borosilicate glass beads of 1 mm mean diameter were used used as the model porous medium (Sigma-Aldrich). The glass beads were chemically pre-treated by soaking in concentrated HCl for 24 h and rinsing with Milli-Q water until the pH was neutral to remove metal oxides, followed by baking overnight at 550 °C to remove organic impurities. The nanoscale surface roughness of glass beads is expected to be small as compared to natural porous media. Thus, both the chemical and physical heterogeneity in the porous medium used for experiments in this work is likely to be small, although not necessarily insignificant. Investigating the level of physicochemical heterogeneity remaining in the already idealized porous medium and its contribution toward immobilization, however, is not explored further. Sandy soils may range in grain size from 0.06-2 mm and likely pack differently than the glass bead bed in our experiments. While the particles and porous media used in this study differ in size and packing from the materials expected in real environmental systems, the goal of this work is not to exactly replicate a natural soil system. Rather, we aim to isolate a problem and disentangle the role that pore structure plays on filtration, which as of yet cannot be investigated in natural samples.

Three different background aqueous solutions were used to vary the particle stability and interface interactions between the silver colloids and the available pore-scale retention sites in the porous medium. The first solution was Milli-Q water (MQW), which was used as the control. The second solution was made with the anionic surfactant sodium dodecylbenzene sulfonate (SDBS) at a concentration of 1% by weight. This surfactant was chosen as representative of laundry formulations[232], thereby simulating the release of silver particles from washed silver impregnated garments. The third solution was made with dissolved organic matter (DOM) at a concentration of 0.02 g L^{-1} as an ubiquitous constituent of soil water and

wastewater sludge with known pronounced effects on colloid transport and stability [162, 69, 76, 65, 233, 234, 235, 236, 237, 238, 73, 104]. Specifically, Elliott Soil humic acid (International Humic Substances Society, St. Paul, MN) was used as a standard DOM, following the solution preparation of Morales et al., (2011) [76].

3.2.2 Column experiments

Cylindrical polypropylene columns (4.7 mm inner diameter and 35 mm length) were wet-packed to a depth of approximately 30 mm with clean borosilicate glass beads. A piece of stainless steel mesh was placed at the top and bottom of the packed bed to uniformly distribute the liquid at the boundaries and prevent the glass beads from entering the tubing. The flow rate was controlled by a push-pull syringe pump that exactly matched the rate at which influent was dispensed at the top and effluent withdrawn from the bottom of the column. Five pore volumes were used to condition the packed columns with the working background solution prior to transport experiments. Then, a pulse of 400 μL of the colloidal suspension was injected at a continuous flow rate, followed by flushing with particle-free background solution until the effluent concentration returned to baseline levels. The effluent concentration was measured in a flow-through cuvette by UV-vis spectrophotometry at a wavelength of 600 nm in 30 s intervals. Particle concentration in the effluent was determined from established linear calibration curves. Following the experiment, the column was sealed at both ends to prevent evaporation, maintained in a vertical position, and immediately analyzed with tomographic imaging on site, to ensure relocation did not change particle deposition patterns.

Replicate experiments were conducted for variable conditions regarding: i) water content (saturated vs. unsaturated), ii) pore velocity (fast vs. slow), and iii) solution chemistry (MQW vs. SDBS vs. DOM) as summarized in Table 3-1. Saturated conditions required inlet/outlet flow rates to always remain matched after wet pack-

ing the column. To achieve unsaturated conditions, the inlet and outlet flow rates were temporarily mismatched (the inlet flow was reduced) to allow for slow draining. When the desired water content was reached (determined gravimetrically), matching of inflow and outflow rates was resumed and allowed to equilibrate prior to injection of the particle suspension. It is important to note that unsaturated experiments experienced a gradient in moisture content with depth, as illustrated in Figure S2, which is extremely difficult to overcome for such small columns. The water content of each packed column was measured before and after the transport experiment to verify that it remained constant. Only experiments that met a constant water content condition were considered here. The pore velocity, $v = q/\theta_w$, was controlled through the imposed Darcy discharge, $q = Q/A$, and the volumetric water content of each experiment, θ_w, where Q is the flow rate and A is the cross-sectional area of the column. The solution chemistry was maintained constant throughout each experiment, whereby the background solution for the suspension and the particle-free solution used to flush out the colloid pulse were the same.

Table 3-1: Summary of experimental conditions tested. q is the Darcy discharge, θ_w/θ is the fraction of water in the pore space or degree of saturation (where θ is the porosity of the packed bed), with classification into saturated θ_s and unsaturated θ_u. v is the resulting average pore velocity, with classification into fast v_f and slow v_s. Solution chemistry includes Milli-Q water (MQW), sodium dodecylbenzene sulfonate (SDBS), and dissolved organic matter (DOM).

Label	q [cm h^{-1}]	θ_w/θ [-]	v [cm h^{-1}]	Solution chemistry
A	38.39	1.00, θ_s	71.95, v_f	MQW
B	13.85	0.35, θ_u	82.41, v_f	MQW
C	18.92	1.00, θ_s	34.99, v_s	MQW
D	13.89	0.42, θ_u	69.47, v_f	SDBS
E	13.89	0.41, θ_u	71.16, v_f	DOM

3.2.3 XCT Scanning and enumeration of retained particles

XCT scanning: X-ray computed tomography (XCT) imaging of the column was conducted with a bench-top scanner (HMX Nikon Metrology, Derby, UK) to obtain a detailed three-dimensional static picture of the distribution of retained colloids in the porous medium. To achieve a voxel resolution of $\sim 10\mu m$, the sample was scanned in two separate segments of $\sim$ 15 mm length. The X-ray source was set to an energy of 50 kV with 300 μA intensity. A 0.1 mm aluminum filter was used to reduce beam-hardening artifacts. A complete 360°scan consisted of 2000 projections, with two frames per projection. Image reconstruction was performed with the scanner's designated software, CT-Pro. Details about the optimized XCT scanning settings are provided in the Supporting Information (SI).

Segmentation: Image segmentation was used to define the different materials in each column with dedicated commercial software for XCT image analysis (VG Studio Max 2.1, Heidelberg, DE). First, the images were pre-processed using a non-local mean filter to increase the signal-to-noise ratio. Adaptive thresholding was then used to segment the bulk phases with operator-specified input parameters for the *solids* (glass beads $\cup$ column), *water*, and *air* (for partly water saturated experiments). Region grower was used to refine particularly noisy bulk phase segmentation results. Finally, global thresholding was used again to segment total retained *silver colloids*, as the sample material with highest X-ray attenuation and largest histogram gray values. It is worth noting that the experimental materials were deliberately chosen to simplify their segmentation based on well-defined histogram peak cutoffs as illustrated in Figure 3-1. The SI describes the control tests performed to determine the visibility of retained colloids in the column.

Three-dimensional regions of interest (ROIs) for each prospective retention site were defined using a sequence of image operations (union, dilation, intersection, and

difference) on the defined bulk phase elements as follows. First, the *solids*, *water* and *air* elements were dilated by 2 voxels, here denoted by the subscript d. Next, the intersection between dilated element pairs $solids_d \cap water_d$, $air_d \cap water_d$, and $air_d \cap solids_d$ were used to create new elements corresponding to interfaces with the *solid-water* (SW), *air-water* (AW), and *air-solid* (TF, which refers to thin films), respectively. The *air-water-solid* (AWS) triple point element was defined as the intersection between $solids_d$, $water_d$ and air_d. The *grain-to-grain* (GG) contact element was obtained from watershed lines of the *solid* element. Then, all retention site elements were dilated by two voxels to create true volumes of otherwise two-dimensional surfaces. This initial definition of elements (i.e., ROIs that delineate the six pore-scale retention sites) causes them to overlap in some portions of the image volume. Subtraction of elements from one another is then used to assign voxels to only one retention site ROI. Lastly, a *bulk liquid* (BL) element was defined as the difference between the *water* element and all retention sites. This site would capture any retained silver mass that might protrude into the bulk water by straining. To summarise, we detect ROIs corresponding to six types of retention size, $\mathcal{S} = \{$SW, BL, GG, AW, AWS, TF$\}$. Figure 3-1 illustrates in false coloring the ROIs for each retention site available for a saturated and an unsaturated column.

3.2.4 Depth profiles and retention site statistics

ROIs belonging to total retained silver (Ag_T) and each individual prospective retention site $i \in \mathcal{S}$ were processed in pairs with the intersection operation to deduce the quantity of silver colloids deposited at each site, Ag_i. Figure 3-2 illustrates this process for silver retained at the SW interface at a given depth, z. These values were subsequently used to obtain i) retention site-dependent depth profiles (Darcy-scale) and ii) the fraction of retained silver in each site to determine their dominance and saturation (pore-scale). To the author's knowledge, this is the first attempt to extract

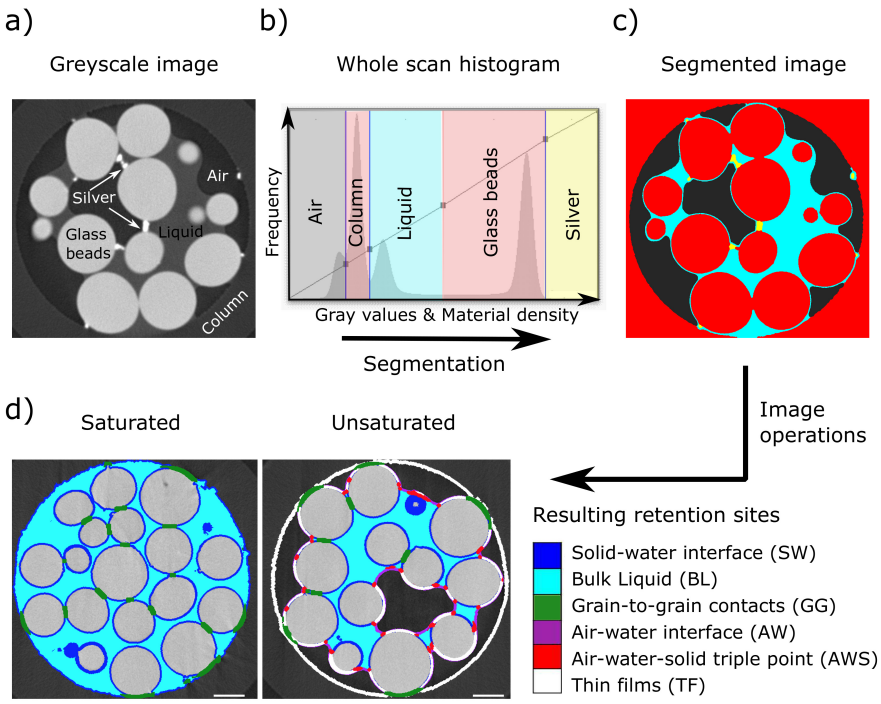

Figure 3-1: Workflow used to define pore-scale retention sites: a) cross section of XCT images in greyscale, b) histogram showing the peak cutoffs used to distinguish each bulk material, c) image segmentation of bulk phases in false coloring, d) cross section of XCT images illustrating the six different retention site ROIs in false coloring for saturated (L) and unsaturated (R) experiments. The scale bar represents 500 μm.

quantitative information relating colloid immobilization to pore-scale retention sites from three-dimensional information of the structure and deposition patterns of a filter medium.

Tomographic images of each experiment described in Table 3-1 contained N cross sections in depth. Each two-dimensional section, n, had a thickness of $\sim 10\mu m$, corresponding to a voxel length Δz. From these data, depth profiles of total silver were extracted, $Ag_T(z)$. The fraction of total retained silver found at each site in a given image cross section, m_i, is given by $m_i(n) = Ag_i(n)/Ag_T(n) = \frac{1}{\Delta z}\int_{\Delta z\cdot(n-1)}^{\Delta z\cdot n} \frac{Ag_i(z)}{Ag_T(z)}dz$. To rank the sites by importance, dominance was measured as the mean fraction of retained silver for a given retention site as:

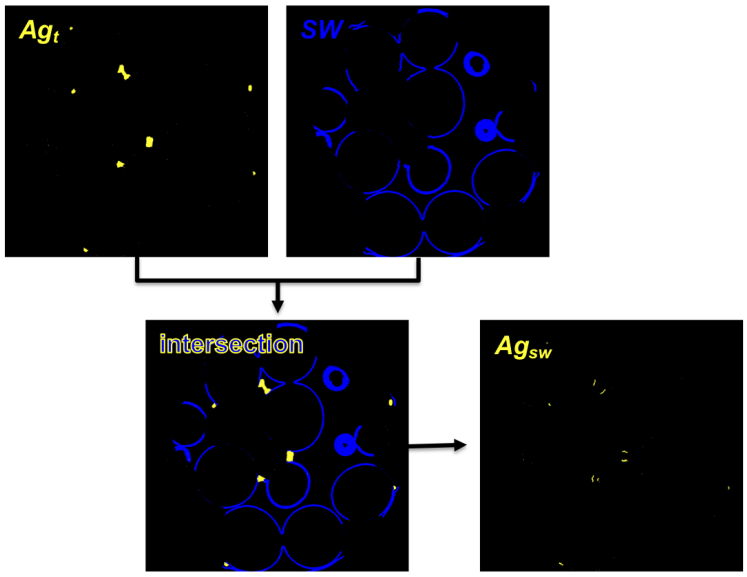

Figure 3-2: Exemplary intersection operation between elements for total retained silver (Ag_T) and a pore-scale retention site (solid-water interface, SW) at a given depth z. The outcome is retention site-specific silver accumulation, here silver retained at the solid-water interface (Ag_{SW}).

$$\bar{m}_i = \frac{\sum_{n=1}^{N} m_i(n)}{N} \tag{3-1}$$

To translate findings to systems with different retention site proportions, knowledge about the fullness of each site is needed. The fraction of retention site volume i filled with silver in a given image cross section, f_i, is given by $f_i(n) = Ag_i(n)/V_i(n) = \frac{1}{\Delta z}\int_{\Delta z\cdot(n-1)}^{\Delta z\cdot n} \frac{Ag_i(z)}{V_i(z)}dz$. Site saturation was then measured as the mean normalized fraction of retained silver by retention site volume as:

$$\bar{f}_i = \frac{\sum_{n=1}^{N} f_i(n)}{N} \tag{3-2}$$

It is noteworthy that the site ROIs can be composed of multiple objects, (discontinuous clusters of voxels, e.g. the grain-to-grain ROI is composed of multiple individual grain-to-grain contacts), where each object can retain different quantities

of silver particles. This is inevitable, yet $\bar{f}_i$ summarizes how full the collection of those objects is with retained colloids and allows us to compare against other retention sites i.

3.2.5 Interaction Energy profiles

Surface interactions for colloids approaching other charged surfaces were determined by extended-DLVO theory and parametrized by the system's physico-chemical properties listed in Table S2. The sum of van der Waals (V_{VDW}), electric double layer interactions (V_{EDL}), steric interactions (V_{ST}) and Lewis acid-base interactions (V_{AB}) are considered for colloid-SW and colloid-colloid systems [239, 240, 161, 162, 241, 242]. Colloid-colloid interactions were used to assess the likelihood for accumulation of colloids at close proximity in GG contacts and AWS triple points. Additionally, hydrophobic interactions, V_{HYD}, are taken into account for the colloid-AW system [243]. There is not a proper interaction energy scheme to describe colloids approaching the TF which is why their profiles are excluded from this analysis.

The analytical expressions for the various interactions considered (in sphere-sphere geometry) are given by the following:

$$V_{VDW} = -\frac{A}{6D}\left(\frac{R_1 R_2}{R_1+R_2}\right)\left[1-\frac{5.32D}{\lambda}\ln\left(1+\frac{\lambda}{5.32D}\right)\right] \tag{3-3}$$

$$V_{EDL} = 64\pi\epsilon\left(\frac{R_1 R_2}{R_1+R_2}\right)\left(\frac{\kappa_B T}{\nu e}\right)^2 \tanh\left(\frac{\nu e\zeta_1}{4\kappa_B T}\right)\tanh\left(\frac{\nu e\zeta_2}{4\kappa_B T}\right)e^{-\kappa D} \tag{3-4}$$

$$V_{ST} = \pi a_{ST}^2 \gamma_0^{ST}\exp\left(-\frac{D}{\lambda_{ST}}\right) \tag{3-5}$$

$$V_{AB} = 2\pi R_1 \lambda_{AB}\gamma_0^{AB}\left[1-\frac{\lambda_{AB}}{R_1}+\left(1+\frac{\lambda_{AB}}{R_1}\right)e^{-\frac{2R_1}{\lambda_{AB}}}\right]\exp\left(-\frac{D}{\lambda_{AB}}\right) \tag{3-6}$$

$$V_{HYD} = -\frac{K_{HYD}}{6D}\left(\frac{R_1 R_2}{R_1+R_2}\right) \tag{3-7}$$

Here, A is the Hamaker constant for the system, D is the separation distance, R_1

and R_2 are the radii of two interacting spheres. For colloid-colloid interactions $R_1 = R_2 = 7\mu m$. For colloid-SW and colloid-AW $R_1 = 7\mu m$ and $R_2 = \infty$. λ, λ_{ST}, and λ_{AB} are the decay length for van der Waals, steric and Lewis acid-base interactions, respectively. ϵ is the dielectric constant of the water, κ_B is the Boltzmann constant, T is temperature, ν is the valence of the symmetric electrolyte, e the charge of an electron, ζ_1 and ζ_2 are the zeta potential of the two interacting materials. κ is the inverse Debye length, a_{ST} is the radius of steric hydration contact. K_{HYD} is the hydrophobic constant for air bubbles interacting with silver particles in water, here estimated as 7.67×10^{-20}.

3.3 Results and Discussion

3.3.1 Darcy-scale fate and transport

Mass balance of silver eluted from each experiment revealed that, on average, $< 10\%$ of the applied silver mass was recovered in the effluent for all tested conditions (See Table S3). Such low mobility is consistent with previous studies on transport of silver particles in neutral to alkaline conditions [220] and is expected for transport of large-sized particles (> 1 μm in diameter, as are the size of our particles) [15]. Here, we exploit the high degree of retention to cross-examine deposition patterns.

Depth profiles of retained particles in experiments testing variable water content are shown in Figure 3-3. The primary y-axis shows a stacked area plot of the fraction of silver particles deposited by available retention site in depth. The secondary y-axis shows the classic depth profile as the total mass of silver retained in depth. Similar profiles corresponding to experiments comparing pore velocity and solution chemistry are provided in Figures S3 and S4, respectively. The large signal variability is due to the high data resolution, given that depth intervals are collected at 10 μm from XCT imaging rather than the 1 cm from standard destructive approaches. Depth profiles

from replicates experiments are in qualitative agreement, but only representative results are presented for the purpose of comparison.

Close inspection of Figure 3-3 reveals two important trends. First, the contribution order toward retention by each prospective site (staked areas) is relatively uniform along the column depth. Even though there is high variability in the signal, there is no cross over of site dominance as a function of depth. This suggests that available sites, however small they are, have not become entirely saturated. In water saturated conditions, the mass of immobilized particles is distributed between three retention sites with substantial contribution from sites other than the SW interface. In water unsaturated conditions, similar trends are observed, albeit with additional retention sites available. The slight change in retained particle distribution in the last 10 mm of the column can be explained by a modest increase in saturated at the lower boundary [208]. In both water saturation systems the SW interface contributes significantly, though not exclusively to particle retention. Knowledge of the identity and relative contribution of active retention sites is critical for improving mechanistic models for colloid filtration. In the following section we discuss the specific contribution by each retention site.

Second, the depth profiles of total mass of silver (black solid line) are non-monotonic and characteristic of *anomalous* transport (the reader is additionally referred to Figure S5 for a moving average of the same signal). *Normal* colloid transport follows an exponential decay in mass retained with depth; thereby any departure from this is considered anomalous. Similar anomalous trends in depth were observed for experiments of variable pore water velocity and pore water chemistry (Figures S3 and S4). Specifically, non-monotonic deposition has been ascribed to non-attached colloids in the near surface domain [111] that may accumulate at hydrodynamically stagnant regions. This mechanistic perception is in agreement with observed accumulation of particles at all depths in GG contacts for the saturated case and AWS

triple points for the unsaturated case. Importantly, distinguishing between the mass retained at perfect sinks (SW with infinite retention time) and imperfect sinks (flow stagnation regions of GG or AWS with finite retention time) can help better understand the mechanisms leading to breakthrough curves with heavy tailing. Modeling broad residence time distributions is yet subject of future work.

In all experiments, particles remained at the BL even after flushing for more than 10 pore volumes likely because, even in a bead pack, the flow field is not perfectly homogeneous [244] and flow-induced aggregation created particle clusters that were too large to be flushed out [209]. Additional tests were conducted in transient conditions for draining (data not shown) that eluted material retained at the BL, thus confirming that the image signal at this location is truthful.

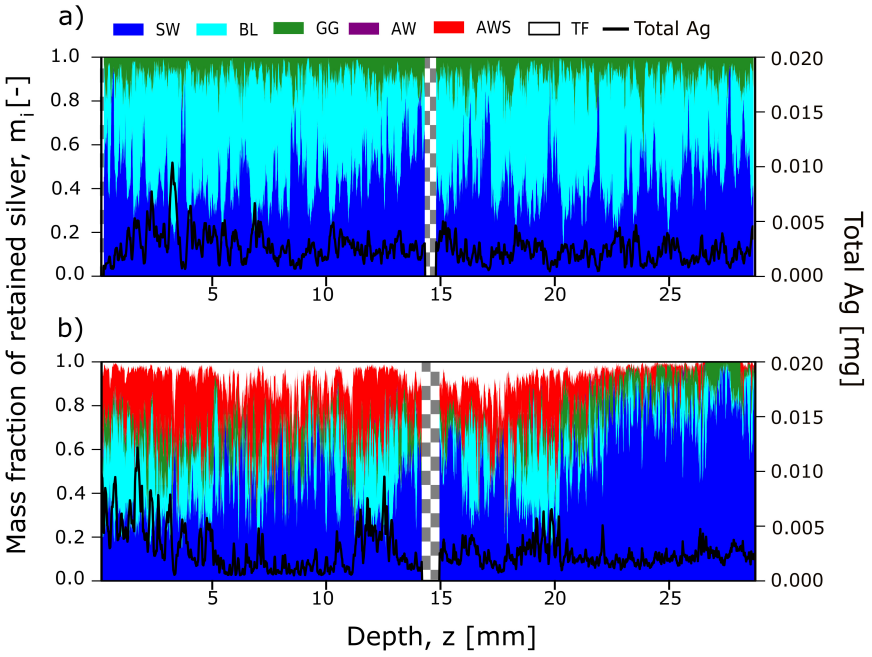

Figure 3-3: Depth profiles. Primary y-axis shows stacked area plots of the fraction of retained silver at six candidate pore sites with depth. Secondary y-axis shows the total retained silver with depth (black line). A comparison is presented for experiments of constant pore velocity (v_f) and solution chemistry (MQW) but variable water content: a) fully saturated (θ_s), b) unsaturated (θ_u). Checkered shading indicates missing data during image stitching. The fraction of retained colloids at each site is relatively constant in depth, while the total mass of silver retained changes non-monotonically with depth.

3.3.2 Pore-scale retention site statistics

Mean site dominance ($\bar{m}_i$), and mean site saturation ($\bar{f}_i$) results are presented as scatter clusters in Figure 3-4. It is worth noting that by definition, $\bar{m}_i$ adds up to unity because it is normalized by the total silver immobilized throughout the column and summarizes the overall site contribution towards particle immobilization. On the other hand, the mean site saturation $\bar{f}_i$ depends on the unique volume of available retention site i and does not need to add up to unity. Subfigures are organized to

facilitate comparisons for variable water content (Figures 3-4a and d), variable pore velocity (Figures 3-4b and e), and variable solution chemistry (Figures 3-4c and f). The reader is referred to Table 3-1 for the other conditions maintained constant for each grouping.

General: Across all experiments, the SW interface (blue markers) was the most dominant retention site (highest $\bar{m}_i$ values) but accounted only for up to half of the total mass retained ($\bar{m}_{SW} \leq 0.5$), while the AW and TF were the least dominant retention sites ($\bar{m}_{AW}|\bar{m}_{TF} \leq 0.15$). This implies that mechanistic models should account for multiple sinks terms to more accurately represent the processes involved in anomalous colloid filtration behavior. Regarding site saturation, no site ever approached its full capacity ($\bar{f}_i < 3 \times 10^{-3}$), however small they were. These outcomes are expected because saturation of a retention site is never anticipated to be complete unless the deposition conditions are fully favorable. This is not the case for any of the experimental conditions in this study. For this and various additional reasons, deposition in a given retention site is hindered, and thus the quantity $\bar{f}_i$ can be limited to a maximum which is lower than unity. Additionally, this suggests that it is unlikely that primary retention would switch from one site to another upon reaching a threshold saturation.

Variable water content: For variable water content, Figure 3-4a shows that the stagnant regions, represented by the GG contacts in saturated and GG plus AWS in unsaturated experiments, are responsible of at least 0.1 of the total mass retained. The BL is the second most dominant site in both saturated and unsaturated conditions, but there is a decrease in $\bar{m}_{BL}$ with decreasing water content. The value of $\bar{m}_{AWS}$ for unsaturated conditions suggests a trade-off of deposited particles between the BL and the stagnant region AWS when the system goes from saturated to unsaturated conditions.

Regarding the site saturation (Figure 3-4d), AWS has the highest value of $\bar{f}_i$

for unsaturated conditions, which means that this site is the most saturated with particles, followed by the SW. In saturated conditions, the GG showed higher f_i than the BL, but the most filled up site with particles was the SW. One can conjecture from these data that, when present, AWS sites affect the flow field more strongly than GG contacts between perfectly spherical grains.

Variable pore velocity: The dominance of the retention sites was similar for variable pore velocity, Figure 3-4b. Nonetheless, it is worth noting that both m_{SW}^{-} and m_{GG}^{-} increased with decreasing v. This observed behavior can be explained by longer contact times between particles and the SW, and longer particle residence times in the stagnation regions when the flow rate/mean pore velocity is lower [109].

The SW saturation (f_{SW}) was comparable to the one of GG (f_{GG}) when pore velocity was reduced, pointing to a larger proportion of retention at the flow stagnation zones of the system—GG contacts under lower pore velocities (see Figure 3-4e). These outcomes are in agreement with detailed studies of the inversely proportional size of flow stagnation zones with flow rate/pore velocity [214]. For the system under investigation, this amounts to larger stagnant flow regions associated with GG contacts at slower pore water velocities, leaving thereby fewer colloids to be retained at the SW interface and the BL.

Variable solution chemistry: For variable solution chemistry, the second most dominant site changes from BL in simple solutions (MWQ) to flow stagnation regions associated with the AWS and GG for more complex solutions (SDBS and DOM) (see Figure 3-4c). Under all tested solution chemistries, the AW and TF ranked at the bottom of the list for site dominance, hinting that the the importance of the AW in unsaturated media is less prominent than has been suggested in the literature. The authors conjecture that the reasoning postulated by Bradford & Torkzaban, (2008)[4] explains this observation. In short, near perfect slip conditions at the AW interface results in colloids sliding along the surface of air bubbles, directing them to AWS

where they can more permanently arrest.

Site saturation in Figure 3-4f was greatest for the SW and AWS interfaces. The large variability observed for f_{BL}^{-} in different treatments makes it difficult to draw general claims about its likelihood to fill up. Similarities in the $\bar{m}_i$ and $\bar{f}_i$ trends across solution chemistries, exclusive of the BL, suggest that changes in the interaction energy between colloids and available charged surfaces were not significantly affected by the presence of surface active compounds.

3.3.3 Interface-scale interaction energy

Energy profiles for a colloid interacting with: the SW interface (solid line), the AW interface (dot-dashed line), and another colloid (dashed line) in MQW solution chemistry are shown in Figure 3-5. Interactions between colloids and the SW interface are characterized by the lowest energy barrier ($\sim 7.5 \times 10^3\ kT$) coupled with the deepest secondary energy well ($\sim -25kT$). These conditions are considered relatively $favorable$ for reversible deposition at this retention site. Similar interactions were found between identical colloids (i.e., for flocculation) with a low energy barrier ($\sim 8{\times}10^3\ kT$) and a slightly more shallow secondary energy well ($\sim$ -5 kT). These conditions too are considered $favorable$ for accumulation of colloids at close proximity in stagnant flow regions. Interactions between colloids and the AW interface involve the highest determined energy barrier ($\sim 3{\times}10^4\ kT$) and an absent secondary energy minimum. Such conditions are typified highly $unfavorable$.

On the basis of interaction energy profiles, silver particles are expected to (i) deposit at the SW interface, albeit at the secondary minimum; (ii) aggregate (including weak flocculation) with comparable proportion at either GG contacts or AWS, depending on the system's water saturation as discussed above, or protruding into the BL; and (iii) never deposit at the AW interface. These interface-scale energetic trends are in agreement with observations of pore-scale site dominance and saturation shown

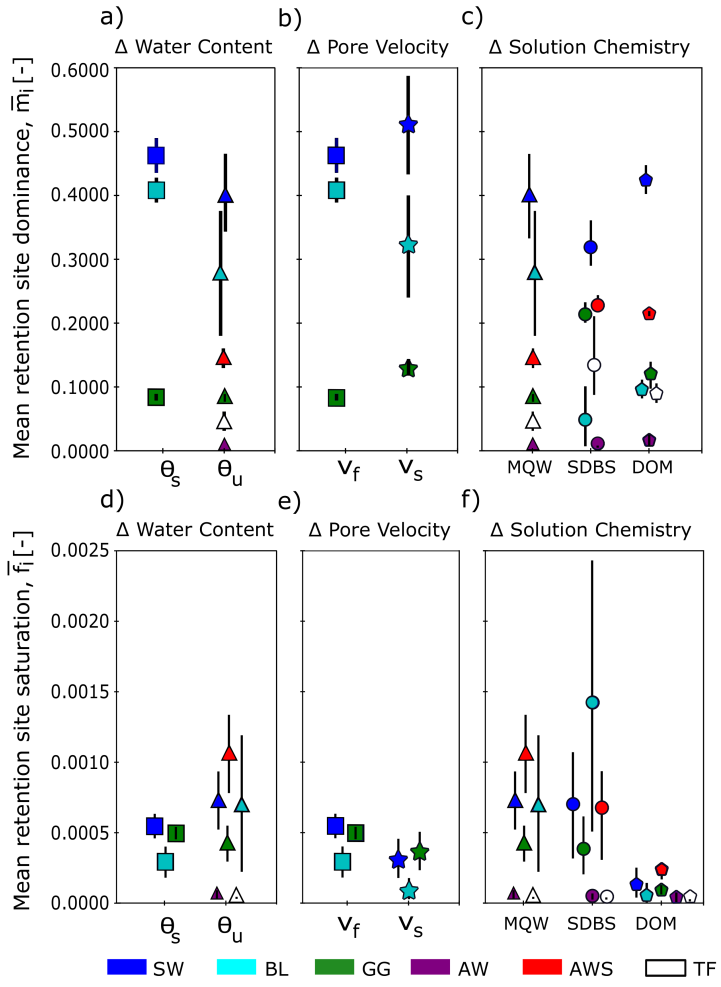

Figure 3-4: (Top) Mean retention site dominance, $\bar{m}_i$, and (bottom) mean retention site saturation, $\bar{f}_i$, for experiments of variable: (a, d) water content, (b, e) pore velocity, and (c, f) solution chemistry. Error bars denote maximum and minimum values for replicate experiments. Retention sites considered are solid-water interface (SW), grain-to-grain contacts (GG), bulk liquid (BL), air-water interface (AW), air-water-solid triple points (AWS), and thin films (TF). The most dominant site for silver retention is the SW, with flow-stagnant regions (GG for saturated and AWS for unsaturated experiments) following closely behind in all experiments. The AW ranked last in dominance whenever present. The site saturation of flow-stagnant regions is comparable to, and at times higher than, the SW. The AW and TF rank lowest for saturation whenever present.

in Figure 3-4 and Darcy-scale depth profiles shown in Figure 3-3, showing consistency across scales of investigation.

The authors note that the magnitude of the energy barrier height ($\gg \mathcal{O}(10^3)$ kT) for all computed interactions is insurmountable and implies that retention at a primary well is extremely unlikely. This is in agreement with the work by Shen et al., (2017) [61], who report a lack for primary minimum interaction for particles larger than 1 μm. In addition, the high degree of particle deposition observed across all experiments suggests that surface heterogeneity on the collector surface may have remained even after efforts to minimize it. While interactions between colloids and nanoscale heterogeneities on the collector surface can be *locally* highly favorable, theoretical interactions based on bulk measurements, as those shown in Figure 3-5, suggest *effective* unfavorable interactions for the system as a whole. That is, the interaction between a colloid and the heterogeneous collector surface is on average highly unfavorable. For the work here presented, the physico-chemical heterogeneity was removed as much as possible through synthetic manufacturing of smooth glass beads and chemical and thermal treatment. Yet, it is difficult to ascertain empirically if any level of heterogeneity remained that contributed to retention. The xDLVO profiles of Figure 3-5 show highly unfavorable effective interactions, yet significant retention was observed. We primarily ascribe this to secondary minimum interactions and pore-structure, but cannot rule out that some level of heterogeneity on the flat interfaces also impacted retention.

When considering heterogeneity more explicitly, colloids are expected to stochastically interact with portions of the collector surface that are entirely within, partially on, or entirely outside a heterogeneous nanosite [114]. These possibilities produce interactions that are favorable, intermediately favorable, or unfavorable, respectively, and cannot be inferred from effective xDLVO profiles. Hence, the authors suggest that a more appropriate representation of colloid-collector interactions in the presence of heterogeneity would honor the variability of possible interactions. However, investigating more deeply the impact of surface heterogeneity on xDLVO energy profiles

and ultimately on upscaled particle transport models is the subject of future work.

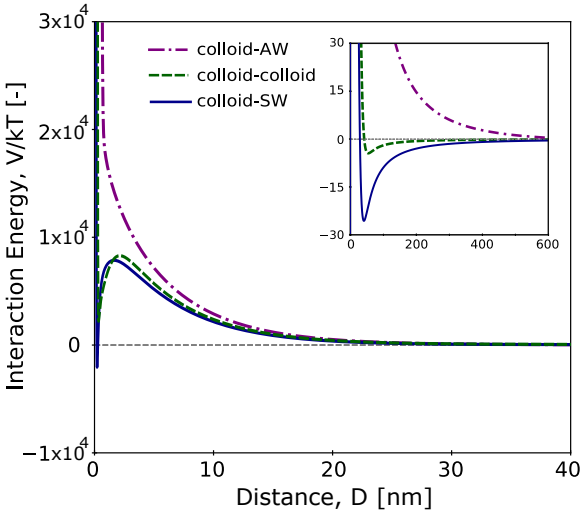

Figure 3-5: Total interaction energy as a function of separation distance for colloids approaching different charged surfaces: solid-water interface (SW), air-water interface (AW), and another colloid. Inset shows the secondary energy minima. The lowest energy barrier and deepest secondary energy well for the colloid-SW interactions are in agreement with the observed dominance of retention at the SW. A similar barrier and slightly more shallow secondary well for colloid-colloid interactions suggest weak aggregation and support the significant particle accumulation at flow-stagnant regions pertaining to grain-to-grain contacts and the air-water-solid triple point. The highest energy barrier and no secondary well for colloid-AW interactions support observations of minimal particle retention at the AW.

3.4 Conclusions

This study demonstrates that colloid deposition at the Darcy-, pore- and interface-scales are in full agreement when the pore structure is taken into account. At the Darcy-scale, transport was deemed consistently anomalous based on non-monotonic depth profiles observed, which are affected by regions of low-flow. Detailed analysis of retention site-specific depth profiles revealed that immobilized colloids were distributed broadly across six candidate retention-sites, and that the distribution was consistent in depth and largely independent of the experimental conditions tested. At the pore-scale, analysis of deposited mass identified the solid-water interface as the dominant retention site in all tested conditions, but it only retained up to 0.5 of the total deposited mass. Significant retention was additionally found in flow-stagnant regions corresponding to grain-to-grain contacts and the air-water-solid triple point for saturated and unsaturated systems, respectively. In unsaturated systems, deposition at the air-water interface was minimal. At the interface-scale, interaction energy profiles were in excellent consonance with the dominance ranking of available retention sites. Attachment to the solid-water interface and weak aggregation (in low-flow regions) were found to be favorable, while attachment to the air-water interface was deemed highly unfavorable. While the idealized colloids and porous media used in this work are a simplification of complex environmental systems, the findings reported shed light on the fundamental role that pore structure in aquifer media plays on the immobilization of suspended groundwater contaminants. Future work with more realistic materials and larger experimental columns would increase the representativeness of the results for real environmental systems. Significant retention of colloids in flow stagnation zones, which are subject to reentrainment by diffusive means, is likely a key driver of ubiquitous heavy tails in breakthrough curves. Understanding the physical justification for colloid elution (e.g., long residence times vs detachment kinetics)

is critical to revise mechanistic models that can more accurately predict fate and transport under environmentally relevant transient conditions.

Acknowledgement

This work was supported in part by the U.S. NSF (EAR-1847689), the Donors of the American Chemical Society Petroleum Research Fund (59864-DNI9), and Marie Curie Actions (FP7-PEOPLE-2012-SoilArchnAg No. 302251). The authors thank the editor and three anonymous reviewers for their constructive feedback. The data for depth profiles of retained particles and retention site distribution are available at https://doi.org/10.5281/zenodo.6456378.

Supporting information

S3-1. Optimized XCT scanner settings

Exponential attenuation law (Equation S3-1) was used to determine the theoretical emerged photon intensity (I) of each material in the sample, where I_0 is the incident beam intensity. X-ray mass attenuation coefficients (μ/ρ) for borosilicate glass, water, and silver were obtained from the NIST data base[1] for the range of photon energies achievable with the XCT system employed (40-400 KeV). Material density (ρ) and thickness values (t) were estimated from known properties, as summarized in Table S3-1. Figure S3-1 illustrates I/I_0 as a function of photon energy. From this figure it is apparent that the greatest difference in emerged photon intensity among the four main materials occurs at low photon energies. Accordingly, the energy level of the polychromatic XCT unit was set to 50 KV along with an 0.1 mm thick Aluminum filter to remove soft X-rays and intensity of 300 μA. Further scanning and image reconstruction specifics include tungsten target material, 2000 projections per scan, 2

[1]DOI: https://dx.doi.org/10.18434/T4D01F

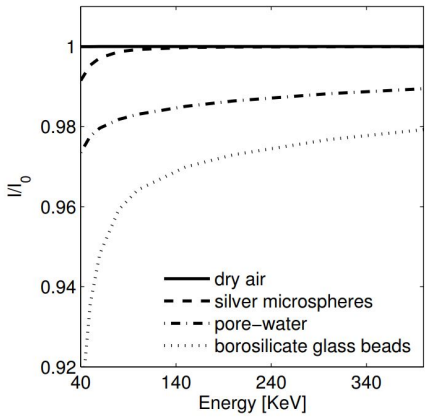

Figure S3-1: Approximate emerged photon intensity of bulk materials in experimental samples at the range of X-ray photon energies available.

frames per projection, as well as correction during reconstruction for beam hardening, noise reduction and minimization of ring artefacts with the commercial software CT-Pro.

$$I/I_0 = exp\,[-(\mu/\rho)x] \tag{S3-1}$$

Table S3-1: Estimated material density (ρ), thickness (t) and mass thickness ($x = \rho t$) for air, silver particles, pore-water, and borosilicate glass beads.

Material	ρ [g cm^{-3}]	t [cm]	x [g cm^{-2}]
Dry air	1.3e-03	0.10	1.3e-04
Silver miscrospheres	10	4.7e-05 [a]	4.7e-04
Pore-water	1.0	0.10	0.10
Borosilicate glass beads	2.2	0.10	0.22

[a] Thickness is estimated as two 118 nm silver coating layers per sphere and at least a pair of spheres.

S3-2. Quality control test for silver colloid visibility in XCT scans

To check the visibility of retained silver-coated microspheres in the XCT images, a known volume of the working colloid suspension was used to saturate a packed column of clean glass beads, which was subsequently scanned. A region of interest at the high end of the histogram, corresponding to silver particles, was used to quantify the volume of visible silver particles in the medium. It was found that 70% of the microsphere volume equivalent was visible in the XCT images. This percentage was applied as a correction factor during mass balance calculations. We note that individual microspheres were difficult to segment in the glass bead-packed column due to their similarity in size to the scan resolution (the so-called partial volume effect), despite their significantly greater attenuation coefficient compared to all other materials in the sample.

S3-3. xDLVO Parameters

The net interaction energy profiles were obtained using equations 7 and the parameters indicated in Table S3-2. K_{HYD} was calculated as the geometric mean of the hydrophobic constant of air bubbles in water, $1{\times}10^{-17}$ J [243, 245], and the hydrophobic constant of silver in water, K_{Ag}. The latter is calculated as $log(K_{Ag}) = -3.194(cos(\theta)) - 18.229$, where θ is the water contact angle on silver[243]. A θ of 20^o was used, based on previously reported values on silver surfaces wettability [246, 247].

Table S3-2: Parameters used for xDLVO calculations.

Description	Symbol	colloid-AW	colloid-colloid	colloid-SW	Units
Hamaker constant	A	-8.47×10^{-20}	1.39×10^{-20}	4.85×10^{-20}	J
Van der Waals decay length	λ	1.00×10^{-7}	1.00×10^{-7}	1.00×10^{-7}	m
Steric decay length	λ_{ST}	4.10×10^{-10}	4.10×10^{-10}	4.10×10^{-10}	m
Lewis acid-base decay length	λ_{AB}	6.00×10^{-10}	6.00×10^{-10}	6.00×10^{-10}	m
Dielectric constant of water	ϵ	80	80	80	-
Temperature	T	298	298	298	K
Valence of sym. electrolyte	z	1	1	1	-
Zeta-potential of colloids	ζ_1	-50.00	-50.00	-50.00	mV
Zeta-potential of collector	ζ_2	-75.00	-50.00	-60.00	mV
Inverse Debye length	κ	5.60×10^{-9}	5.60×10^{-9}	5.60×10^{-9}	m
Steric hyd. contact radius	a_{ST}	2.67×10^{-4}	1.14×10^{-7}	3.27×10^{-8}	m

Table S3-3: Experimental conditions and mass recovery for transport tests.

Label	Q [$m^3 s^{-1}$]	Inj. time [s]	Inj. mass [mg]	Mass in column [mg]	Retained mass [%]
A	1.82e-09	222	8.06	7.41	91.88
B	8.81e-10	480	8.46	7.75	91.64
C	8.95e-10	487	8.72	7.92	90.75
D	8.83e-10	460	8.13	7.67	94.34
E	8.83e-10	470	8.32	7.87	94.52

S3-4. Mass Balance of Particles Injected, Eluted and Retained

S3-5. Depth Profiles & Retention Site Distribution in Depth

Figure S3-2 illustrates the availability of retention sites in depth for the experimental conditions in Table 1 (main text). Depth profiles of retained particles in experiments testing variable water pore velocity and water pore chemistry are shown in Figures S3-3 and S3-4. The primary y-axis shows a stacked area plot of the fraction of silver particles deposited by available retention site in depth. The secondary y-axis shows the classic depth profile as the total mass of silver retained in depth. Figure S3-5

illustrates the moving average of the depth profile signals for all experiments.

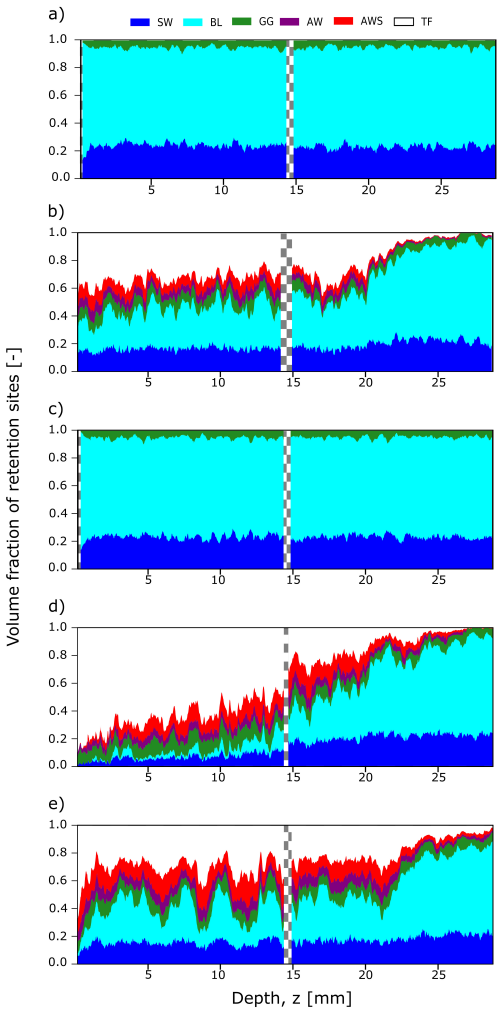

Figure S3-2: Retention site distribution in depth shown as volume fraction (volume of the retention site over the total volume available for particle retention). Figures correspond to experiments type a) A with fast pore water velocity (v_f), saturated conditions (θ_s), and MQW; b) B with fast pore water velocity (v_f), unsaturated conditions (θ_u), and MQW; c) C with slow pore water velocity (v_s), saturated conditions (θ_s), and MQW; d) D with fast pore water velocity (v_f), unsaturated conditions (θ_u), and SBDS; and e) E with fast pore water velocity (v_f), unsaturated conditions (θ_u), and DOM. Checkered shading indicates missing data during stitching.

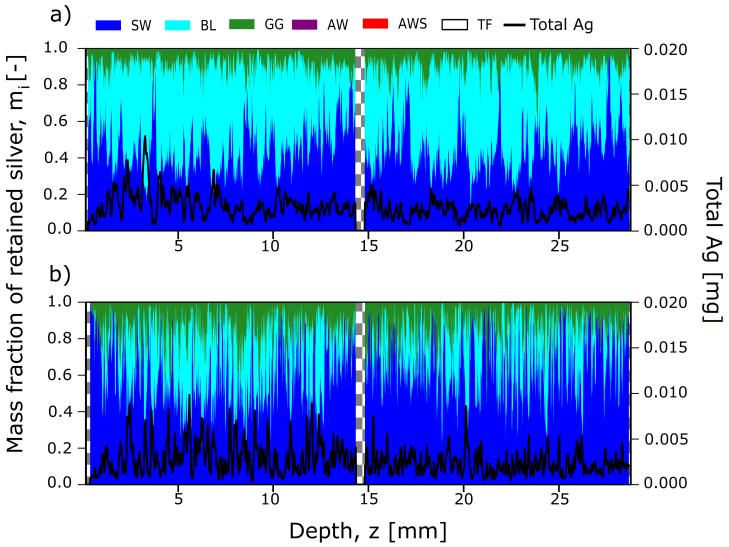

Figure S3-3: Depth profiles. Primary y-axis shows stacked area plots of the fraction of retained silver at the available pore sites with depth. Secondary y-axis shows the total retained silver with depth. A comparison is presented for experiments of constant water content (θ_s) and solution chemistry (MQW) but variable pore water velocity: a) fast (v_f), b) slow (v_s). Checkered shading indicates missing data during stitching.

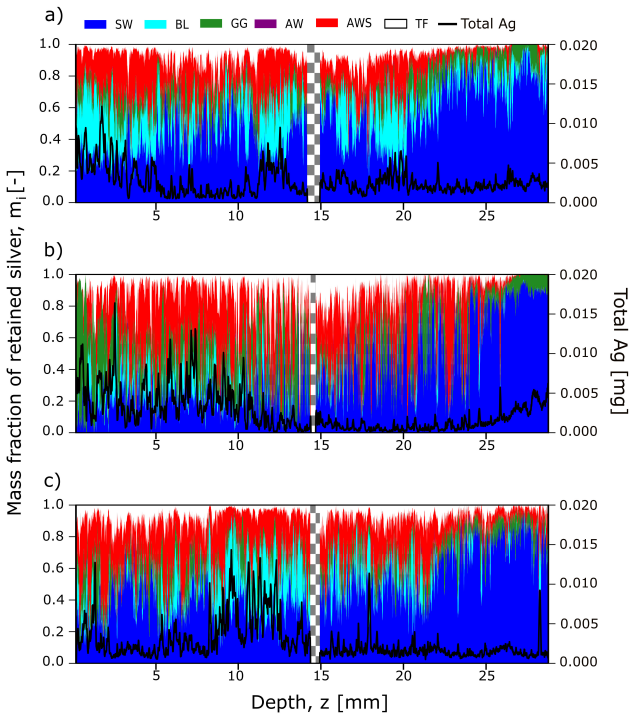

Figure S3-4: Depth profiles. Primary y-axis shows stacked area plots of the fraction of retained silver at the available pore sites with depth. Secondary y-axis shows the total retained silver with depth. A comparison is presented for experiments of constant water content (θ_u) and pore velocity (v_f) but variable solution chemistry: a) MQW, b) SBDS, c) DOM. Checkered shading indicates missing data during stitching.

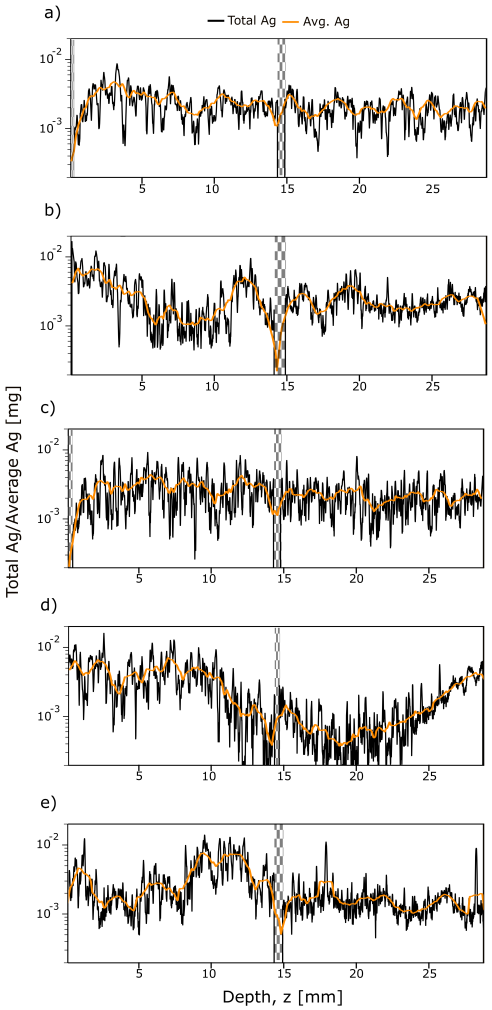

Figure S3-5: Depth profiles showing the total retained silver with depth (black solid line) and a moving average of 100 points (orange solid line) to illustrate the profile anomalous shape. Figures correspond to experiments typea) A with fast pore water velocity (v_f), saturated conditions (θ_s), and MQW; b) B with fast pore water velocity (v_f), unsaturated conditions (θ_u), and MQW; c) C with slow pore water velocity (v_s), saturated conditions (θ_s), and MQW; d) D with fast pore water velocity (v_f), unsaturated conditions (θ_u), and SBDS; and e) E with fast pore water velocity (v_f), unsaturated conditions (θ_u), and DOM. Checkered shading indicates missing data during stitching.

Morphology of Shear-Induced Colloidal Aggregates in Porous Media: Consequences for Transport, Deposition and Reentrainment[c]

Alejandro J. Perez[1], Janis E. Patiño[1], Miroslav Soos[2], Verónica L. Morales[1]

[1] Department of Civil and Environmental Engineering, University of California, Davis

Davis, United States

[2] Department of Chemical Engineering, University of Chemistry and Technology

Prague, Czech Republic

Abstract

Colloid deposition in granular media is relevant to numerous environmental problems. Classic filtration models assume a homogeneous pore space and largely ignore colloid aggregation. However, substantial evidence exists on the ubiquity of aggregation within porous media, suggesting that deposition is enhanced by it. This work studies the deposition process in relation to aggregate size and structure. We demonstrate that aggregation is induced at typical groundwater velocities by comparing the repulsive DLVO force between particle pairs to the hydrodynamic shear force opposing it. Column experiments imaged with high-resolution X-ray Computed Tomography were used to measure aggregate structure and describe their morphology probability distribution and spatial distribution. Aggregate volume and surface area were found to be power-law distributed, while Feret diameter was exponentially dis-

[c] This chapter has been published as: Perez, A. J., Patino, J. E., Soos, M., & Morales, V. L. (2020). Morphology of shear-induced colloidal aggregates in porous media: consequences for transport, deposition, and re-entrainment. Environmental Science & Technology, 54(9), 5813-5821.

tributed with some flow rate dependencies caused by erosion and restructuring by the fluid shear. Furthermore, size and shape of aggregates are heterogeneous in depth, where a small number of large aggregates control the concentration vs depth profile shape. The range of aggregate fractal dimensions found (2.2-2.42) implies a reaction limited aggregation process and a high potential for restructuring and/or breaking during transport. Shear-induced aggregation is not currently considered in macroscopic models for particle filtration, yet is critical to consider in the processes that control deposition.

4.1 Introduction

Colloid phenomena play an important role in porous media processes, including environmental fate and transport of colloids, colloid-associated contaminants, and nanomaterials [248, 249, 133]; granular media filtration [250]; clogging [251, 252]; and soil structure [253]. Numerous studies have suggested that aggregation can notably affect colloidal toxicity [254, 255, 256, 257],reactivity [258, 257, 259, 260], and environmental transport[102, 40, 41, 240, 39, 103]. For transport, aggregate structure has been shown to have a strong impact on deposition and mobilization [39, 261, 240, 41, 40, 103], although the detailed processes are not well understood.

According to colloid filtration theory (CFT), particle deposition in porous media occurs in sequential steps for transport and attachment[46]. During transport, particles are brought to the vicinity of a collector by Brownian diffusion, interception, and gravitational sedimentation. During attachment, particles interact with the collector surface at very short distances thought to be driven in large part by Derjaguin-Landau-Verwey-Overbeek (DLVO) interactions[56, 129]. The steady-state solution of CFT predicts that the depth dependence of particle accumulation should be exponential, which is frequently discrepant with experimental results. A key assumption made by CFT is that particles travel and interact with collector surfaces individually. However, direct evidence of the ubiquity of aggregation within porous media by numerous studies [39, 97, 40, 102, 41, 103] suggests that this assumption is mechanistically incorrect, and that aggregation is responsible for enhanced deposition. To the

authors' knowledge, Legg et al., (2014) [41] is the only study to present experimental evidence that particles preaggregate in the bulk fluid and subsequently deposit onto collectors as sparse-fractal aggregates (low-density), hinting that ripening is not the only mechanism through which aggregates deposit in the pores.

To correct for aggregation effects on the transport step, some studies propose to use an equivalent size given by the radius of gyration (or hydrodynamic size) of the aggregate and its effective density given by the fractal dimension, both of which impact the suspension's diffusivity [225, 240], drag[262, 263, 240], and sedimentation [189]. Conversely, Lin et al., (2012) [240] show that the size of the primary particle, not its aggregation state, determines the magnitude of the strength of colloidal interaction within the framework of DLVO theory; hence implying that the attachment step needs no correction. Moreover, very large aggregates are further immobilized by straining processes[213, 264]. The dynamic process of deposition involves attachment, detachment, as well as local erosion and rearrangement of existing colloidal deposits. Various recent studies have sought to correlate colloid deposition in porous media with aggregate structure, paying close attention to aggregate fractal dimension [240, 103, 39, 265, 261, 41]. Beyond aggregate compactness and size, however, morphologic properties like sphericity expose the ability of amorphous clusters to move across pore spaces given their orientation and response to shear flow [262, 266, 267, 268, 269, 270].

It is well known that the size and structure of colloidal aggregates is affected by chemical conditions [41], primary particle shape [271], and most importantly by the fluid flow to which the suspension is exposed [262, 265]. Hydrodynamic forces in the fluid experienced by suspended particles can enhance aggregation or deposition onto the porous medium surface. Similarly, shear stress on the aggregate can induce its breakup or restructuring [262, 103, 240, 41]. In environmental hydrodynamic systems, aggregation is generally considered to be reaction limited, whereby a repulsive energy barrier must be overcome by chemical or mechanical means to obtain successful ag-

gregation. Such reaction limited aggregation (RLA) tends to form more compact structures with characteristic fractal dimension of ~ 2.1, compared to those formed by diffusion limited aggregation (DLA) with fractal dimension of ~ 1.75 [240, 272].

In porous media, the coupling between pore fluid flow, colloid deposit morphology, and pore geometry has been found to clog the pore space and affect the evolution of head-loss [102, 103, 40, 261]. As deposition progresses, deposits on the filter media may locally alter the flow, which can impact subsequent removal of incoming particles or aggregates [261]. This consequently leads to a buildup of localized fluid shear that may restructure or break up aggregates, causing mobilization and redistribution of the colloidal material along the packed bed[41]. Results from simulations show that large particles and higher fluid velocities tend to form dense deposits of higher fractal dimension that are less prone to breakage and resuspension, while small particles and low fluid velocities produce more open deposits of lower fractal dimension[261]. Aggregates with lower fractal dimension have been shown to break more easily [265]. Frail aggregate deposits break in localized zones of high shear. This mobilizes colloidal material of lower fractal dimension, leaving behind a more compact deposit at the origin[103]. Redistribution of sloughed colloidal material locally recuperates permeability of the pore structure, permitting the colloidal filtration process to resume in a semi-clean bed as a system with self-regulating negative feedback [102].

In this study, direct measurements of the structure of colloid deposits in porous media are used to investigate the relationship between imposed flow rate, aggregate structure and the particle deposition mechanism. We consider the possibility that hydrodynamic shear can provide sufficient energy to overcome electrostatic repulsion between suspended colloids to induce aggregation and encourage deposition. Calculations of the opposing forces are presented to support our hypothesis. Detailed characterization of colloidal aggregates is used to determine how flow rate controls the variability in formed aggregate size and morphology. We then examine how aggregate

structure is linked to its ability to penetrate the packed bed, and use this to explain the concentration profile shape with depth. Lastly, aggregate mechanical properties are analyzed in light of their tendency to become unstable and undergo detachment (re-entrainment) during a physical or chemical disturbance.

4.2 Materials and Methods

4.2.1 Materials

Custom made hollow glass microspheres coated in a layer of 118 nm silver were used as the silver colloids for experimentation (Microsphere Technology, Limerick, IE). Silver particles were deliberately chosen because they facilitate imaging with X-rays as described below. According to the manufacturer, their mean diameter is 14±4 μm and density is 1.0 g mL^{-1}. Suspensions of 0.02 g mL^{-1} were prepared in Milli-Q water (pH=7, and ionic strength of 0 mM unless otherwise indicated) and used in experiments within 10 hours. Borosilicate glass beads of 1 mm mean diameter were used as the porous medium (Sigma-Aldrich). The glass beads were chemically pre-treated by sequential soaking in concentrated HCl for 24 hours to remove metal oxides, repeated rinsing with Milli-Q water until the pH was neutral, and then baked overnight at 550 °C to remove organic impurities.

subsectionSmall Angle Light Scattering

Small Angle Light Scattering (SALS) was used to monitor the silver aggregation extent prior to injection of the colloidal suspension into the columns for transport experiments. Here, the average radius of gyration of the clusters, $\langle R_g \rangle$, was measured under quiescent conditions (i.e., in the absence of hydrodynamic shear). The SALS instrument used in this work (Mastersizer 2000, Malvern, UK) has a working angle range θ = 0.02-40°, a wavelength of incident light λ_0 = 633 nm, and an intensity acquisition frequency of 1,000 s^{-1}. Details of the SALS system can be found else-

where [273], and the calculations for estimating $\langle R_g \rangle$ are described in the Supporting Information (SI). SALS measurements demonstrate that the chosen water chemistry creates unfavorable conditions for aggregation in our suspension. Hence, a physical factor must be responsible for any observed aggregation during transport, where hydrodynamic shear is present.

4.2.2 Opposing DLVO Repulsive and Hydrodynamic Shear Forces

Colloidal particles are typically stabilized by forces of electrostatic origin, indicating that the repulsive force barrier must be overcome for charge-stabilized particles to aggregate. In a porous medium, a suspension is subjected to shear by the nature of the flow, which can be sufficiently strong to "push" repulsive particles together. Hence, the occurrence of shear-induced aggregation can be assumed to depend on the balance between DLVO and shear forces [274]. We determine the propensity for shear-induced aggregation by considering the maximum shear force available at a given shear rate in comparison to the repulsive force barrier of the suspension.

To compute the repulsive barrier (the maximum force), the force between interacting identical particles was determined from classical DLVO theory. Repulsive electric double-layer force, F_{edl}, was estimated from the derivative of the potential energy of interaction as approximated by Gregory (1975) [275] as:

$$F_{edl} = \frac{64\pi a \eta_\infty k_B T}{\kappa} \gamma^2 exp(-\kappa h). \tag{4-1}$$

Here, a is the radius of the colloid, η_∞ is the bulk number density of ions, k_B is the Stefan-Boltzmann constant, T is the absolute temperature, $\gamma = tanh(ze\zeta/4k_BT)$ is the reduced surface potential of the colloid as a function of the ion valence, z, and the measured colloid zeta potential, ζ (measured with ionic strength of 1mM KCl),

κ is the inverse Debye length, and h is the separation distance. Attractive Van der Waals force, F_{vdW}, was estimated from the derivative of the retarded potential energy of interaction proposed by Gregory (1981) [239] as:

$$F_{vdw} = -\frac{Aa(1+\frac{28}{\lambda}h)}{12(h+\frac{14}{\lambda}h^2)^2}. \tag{4-2}$$

Here, A is the system's Hamaker constant and λ is the characteristic wavelength of the interaction, which has a value of l00 nm for most materials [162]. The total force profile, F, is the sum of F_{vdw} and F_{edl}.

Nano roughness on the surface of the colloidal particles were qualitatively observed with Scanning Electron Microscopy (see Figure S2 in the SI), and accounted for in the total force profile as per the work of Torkzaban et al., (2015)[252]. Surface roughness effects were incorporated into DLVO calculations to quantify the magnitude of the total force of non-smooth colloids. A simplified random representation of random roughness is considered with pillars of height h_r in the range 35-50 nm, and surface density f between 0.5-4%. The mean total interaction energy, $F_m(h)$, is estimated as the linear combination of interaction energies of asperity element tops and the smooth surface bottom as:

$$F_m(h) = (1-f)F(h+h_r) + (f)F(h). \tag{4-3}$$

To determine the maximum shear force available, the maximum hydrodynamic force, $F_s^{(max)}$, for two equal-sized spheres approaching each other in a simple shear flow was calculated as per the work of Husband & Adams, (1992) [276]:

$$F_s^{(max)} = 3.06\pi\mu\langle R_g\rangle^2 G. \tag{4-4}$$

Here, μ is the dynamic (shear) viscosity of the fluid and G is the measured shear rate in the column determined by Eq. S4 in the SI. The force balance results are

interpreted in consideration of the relevant inter-particle and hydrodynamic forces involved.

4.2.3 Column Experiments

Cylindrical polypropylene columns (4.7 mm inner diameter and 35 mm length) were wet-packed to a depth of approximately 30 mm with the clean glass beads and maintained fully water saturated. A piece of stainless steel mesh was placed at the top and bottom of the packed bed to keep the glass beads in the column and out of the influent/effluent tubing. The packed columns were conditioned with five pore volumes of Milli-Q water prior to transport experiments in a downward flow arrangement. Then, 400 μL of the colloidal suspension was injected at a continuous flow rate, followed by flushing with particle-free background solution of Milli-Q water until the effluent concentration returned to baseline levels. Effluent concentration was measured in a flowthrough cuvette by UV-vis spectrophotometry at a wavelength of 850 nm in 30 s intervals. The flow rate was controlled by a push-pull syringe pump that exactly matched the rate at which influent was dispensed at the top, and effluent withdrawn from the bottom of the column. Triplicate experiments were conducted for two different flow rates, 3.2 and 6.4 mL hr^{-1}. Following each experiment, the column was sealed at both ends to prevent evaporation, maintained in a vertical position, and was immediately analyzed with tomographic imaging on site to ensure relocation did not change particle deposition patterns.

4.2.4 XCT Scanning and Image Processing

X-ray computed tomography (XCT) imaging of the column was conducted with a benchtop scanner (ZEISS Xradia, MicroXCT-200) at the University of California, Davis to obtain a detailed three-dimensional static picture of the distribution of colloid deposits in the porous medium. The materials that make up the packed column and

the colloidal suspension were selected to obtain the greatest contrast and best quality images with XCT. To achieve a voxel resolution of 10 μm, the sample was scanned in multiple segments that were subsequently stitched together during reconstruction. The power of the X-ray source tube was set at 8 W with an energy of 40 kV. An Xradia LE#3 source filter was used to harden the spectrum and reduce beam-hardening artifacts. A complete 360°scan consisted of 1600 projections and required about 4 hr per segment. Each scan produced projection data of the packed porous media in segments of length of $\sim$ 10 mm. The projection data of each segment was used to reconstruct a stitched image of the column. Reconstruction and stitching was done with XRADIA proprietary software, TXM Controller, TXM Reconstructor and TXM Viewer.

Segmentation

Segmentation of the column images was performed with dedicated commercial software for XCT image analysis (Volume Graphics Studio Max and Amira). First, the images were pre-processed using a non-local mean filter to increase the signal-to-noise ratio. A hybrid segmentation approach, combining global thresholding and locally adaptive thresholding, was used to define regions of interest corresponding to the colloid deposits and the pore space. Next, global histogram thresholding was used to remove voxels corresponding to the silver colloids, as the sample material with highest X-ray attenuation and largest histogram gray values. Then, locally adaptive thresholding was used to perform precise segmentation of the pore space with operator-specified input parameters of the existing solid and liquid phases. Region grower was used to refine particularly noisy pore space segmentation results. Segmented images of colloid deposits and the pore space were finally used for aggregate morphology and shear rate distribution analyses, respectively.

Aggregate Morphology

Image processing and analysis of the morphological characteristics of colloidal deposits formed in porous media were performed using the software Fiji/ImageJ [277], including the Particle Analyser plugin in BoneJ [278] and Matlab. Particle Analyser (with a mesh resampling factor of 1) identifies individual particle clusters and analyses their characteristics separately for volume (V); surface area (SA); Feret diameter (Fe), as maximum diameter; geometric centroid coordinates (x, y, z); and major (r_{Maj}), intermediate (r_{Int}), and minor (r_{Min}) radii of the best fit ellipsoid. Geometric sphericity ($\psi = \frac{(36\pi V^2)^{(1/3)}}{SA}$) and aspect ratio ($AR = \frac{r_{Min}}{r_{Maj}}$) were additionally determined from the plugin outputs. Aggregate cohesive force and compaction were determined from fractal dimension, D_3, obtained from the scaling of the number of primary particles in an aggregate, N, vs the ratio between the minimum radius of the aggregate, r_{Min}, and the primary particle radius, r_0, such that $N \sim (r_{Min}/r_0)^{D_3}$. N is approximated as the ratio of measured aggregate volume to primary particle volume. Our analysis considers six structural characteristics, M_i, measured for each aggregate: V, SA, Fe, ψ, and AR, and D_3. The SI describes various control tests performed on the data to determine its quality and the smallest cluster size distinguishable from noise, given that individual primary particles cannot be resolved with this experimental setup.

4.2.5 Statistical Analysis

Global probability density functions were assessed for each aggregate morphology to evaluate their distribution and relative abundance as $p(M_i)$. Cross-correlations were used to measure similarities between morphologic characteristics. Significant correlations were those with an absolute Pearson's linear coefficients greater than 0.7 and p-values below 0.05. Conditional probabilities were used to evaluate different shape characteristics relative to aggregate volume as $p(M_i > M_i'|V)$. Trends in depth were

evaluated with joint probability density function for each morphological characteristic as $p(M_i, z)$. All statistical analysis was restricted to clusters containing at least 10 primary particles. Fractal dimension was evaluated for clusters of at least 30 primary particles as recommended by Lee & Kramer, (2004) [279]; to reduce uncertainty in the estimation of N due to partial volume effects, which diminishes with increasing aggregate size.

4.3 Results and Discussion

4.3.1 Suspension stability

Average radius of gyration of the colloid suspension prior to column injection was measured with SALS as 26.18 μm. This suggests that the suspension is stable under quiescent conditions (absence of fluid shear), and that formed colloid clusters are on average triplets over the course of a 20 minute time period. This measurement is used as a control to compare the aggregate size distributions achieved when the suspension is subjected to fluid shear during transport through porous media, as discussed below.

4.3.2 Opposing DLVO repulsive and hydrodynamic shear forces

A comparison between opposing DLVO repulsive and hydrodynamic shear forces enables determination of the critical hydrodynamic force required to onset shear-induced aggregation. The following presents a force balance approach similar to that used by Husband & Adams (1992), [276] who studied the forces involved in orthokinetic aggregation. Figure 4-1 shows exemplary DLVO force profiles of interacting colloids, considering nanoscale surface roughness (profiles corresponding to other densities are not shown). From these data, we estimate that the force barrier magnitude F_m could have a range of 9.3×10^{-11} to 4.9×10^{-10} N. The maximum hydrodynamic force (from Eq. 4-4) was determined to have a magnitude of $F_s^{(max)} = 2.83\times10^{-10}$ and 5.65×10^{-10}

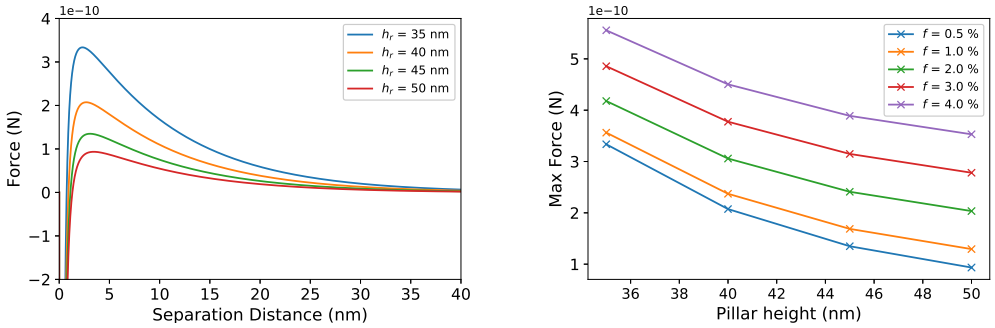

Figure 4-1: (Left) DLVO force profiles as a function of particle separation, corrected for nanoroughness of density $f = 0.5\%$ and variable pillar height, h_r. (Right) Force barrier for various combinations of roughness density and pillar height.

N for the slow and fast flow rates, respectively. Hence, the hydrodynamic shear over the quiescent triplets is confirmed to be large enough to overcome the repulsive force stabilizing the suspension and stimulate efficient aggregation, particularly for surface roughness of characteristically large pillar heights or low densities. The maximum shear force is found in 16% and 19% (8 and 10 times per mm^3 of media) of the channels in the column for slow and fast flow rates, respectively (also illustrated in Figures S4 and S5). An example of the lower force requirement occurrence for a specific suspension is given in section S3. The authors note that lubrication forces are not accounted for since the surface roughness in the system is rather large. As noted by Husband & Adams (1992) [276], considering the relevant hydrodynamic and inter-particle forces involved at constant water chemistry, too low a shear rate applied to a suspension will only break weak floccs formed at the secondary minimum. An increase in shear will result in productive aggregation into the primary minimum. Increasing the shear rate further may destroy previously formed aggregates.

Aggregate Size and Morphology

Global probability distribution functions for each characteristic measured are shown in Figure 4-2 for the two flow rates tested. The range of values for all morphologies is similar for both flow rates. Volume and surface area are power law distributed

($p(M_i) = mM_i^B$, where m is a constant and B is the scaling exponent), while Feret diameter shows an exponential distribution ($p(M_i) = me^{BM_i}$, where m is a constant and B is the power exponent). These distributions capture the strong heterogeneity of the colloidal aggregates. The fitted scaling exponents, B, increase with flow rate as shown in Table S1. The distributions for volume and surface area are power-law, and therefore are also scale invariant. Their fitted scaling exponents, $B < 1$, indicate that they also lack a well-defined mean and variance, since a power-law x^{-B} has a well-defined mean over $x \in [1, \infty)$ only if $B > 2$, and a finite variance only if $B > 3$. This shows that although very few voluminous aggregates contribute to most of the deposited colloidal mass, this small number of aggregates can strongly influence the concentration distribution in depth. Feret diameter, on the other hand, has well-defined moments with lower variability between diameters for the most and least probable aggregates. The distribution of sphericity is flow rate-dependent. Fast flow rates display a bimodal distribution with peaks at 0.4 and 0.8, where the more spherical second mode is more probable. Slow flow rates have an unimodal distribution skewed to higher values that peaks at 0.8. The distribution of aspect ratio approaches a Gaussian and peaks similarly at 0.4 for both flow rates. The mean and variance of the aspect ratio and sphericity distributions are reported in Table S1. The bimodal quality of sphericity may be attributed to aggregate stretching due to the increased shearing at higher flow rates, which is in agreement with increased skewness in the distribution for aspect ratio at the same flow conditions.

A major factor affecting an aggregate's response to flow is its shape [262]. On the one hand, the volume of an aggregate informs on its tendency to be strained and immobilized during transport through porous media [264, 269]. On the other hand, Feret diameter, sphericity, and aspect ratio inform about its susceptibility to pass through a pore throat based on its orientation with the flow. Spherical aggregates rotate smoothly in the presence of velocity gradients, while elongated aggregates expe-

rience oscillations of angular velocity in shear flows [262]. To the authors' knowledge, the effects of aggregate elongation morphology on deposition and transport kinetics in porous media have not been studied. However, the effect of primary particle aspect ratio on straining and transport has received some attention, albeit with conflicting results [266, 267, 268, 269, 270]. A greater amount of straining has been shown to occur for elongated primary particles, compared to spherical ones [267, 268]. However, observations of the opposite have also been reported[269, 266], attributing the effect to preferred rotation and orientation of the particle as it approaches a pore constriction. That is, the minor axis of the particle is considered to be the critical dimension controlling straining retention processes.

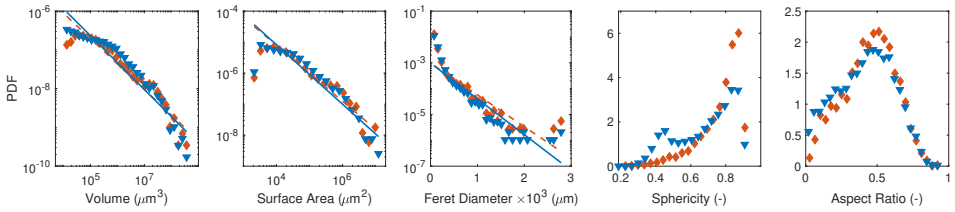

Figure 4-2: Probability density functions of colloidal aggregate size and morphology characteristics. Symbols correspond to experiments of slow (diamonds) and fast (triangles) flow rates. Lines indicate the power law or exponential fit to distributions for volume, surface area, and Feret diameter for slow (dashed) and fast (solid) flow rates.

In addition to the insights gained from individual aggregate structure distributions, it is useful to know how structural characteristic pairs are correlated. Figure 4-3 shows correlation matrices of the five characteristics investigated. P-values for all pairs were less than 0.05, signifying statistical significance across the board. Positive correlations with Pearson coefficients greater that 0.7 were found between volume-to-surface area, volume-to-Feret diameter, and Feret diameter-to-surface area for both flow rates. These three characteristics are strongly correlated in large part because of the prevalence of small aggregates with maximal surface area and limited configuration for Feret diameter. Anti-correlations were found only between Feret diameter-to-sphericity at slow flow rates. This could be attributed to the elongated

shape of larger nonspherical aggregates. In general, correlations between pairs were weaker for fast compared to slow flow rates corroborating the increased heterogeneity with higher shear.

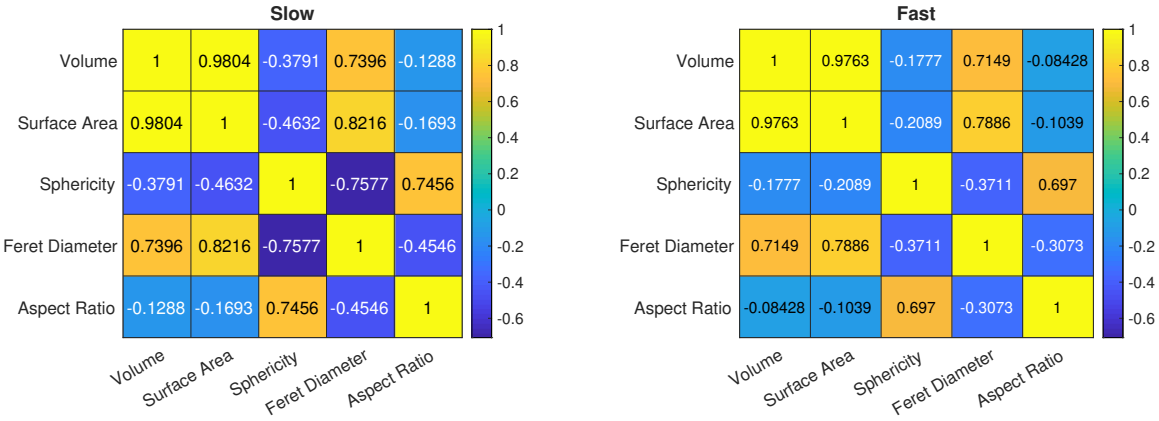

Figure 4-3: Pearson's rank correlation matrix of aggregate morphological characteristics for experiments conducted at slow and fast flow rates.

The distribution of the different measured morphologic characteristics relative to the given aggregate volume are shown in the conditional probability plots, $p(M_i > M_i'|V)$, of Figure 4-4. Reference lines for surface area and Feret diameter of ideal spheres of the same given volume are shown in black. Trends across the two flow rates are similar for all characteristics in aggregates larger than $10^{-5}\mu m^3$. Generally, the surface area and Feret diameter of aggregates increasingly depart from that of a perfect sphere as volume increases, suggesting that small aggregates approach spheres but acquire an elongated geometry as they grow in size [280]. A decrease in sphericity and aspect ratio with increasing volume for aggregates larger than $10^{-5}\mu m^3$ corroborates this trend. Differences in flow rate are seen, however, in Feret diameter and sphericity for aggregates smaller than $10^{-5}\mu m^3$. Small aggregates formed with fast flow rates have a broader range of Feret diameters and depart more strongly from the ideal sphere reference line than their slow flow rate counterparts. Similarly, sphericity changes non-monotonically with volume for fast flow rates, while slow flow rate shows a fairly uniform distribution for this volume range. We speculate that large aggre-

gates are retained by straining processes, and become elongated by the hydrodynamic shear which is stronger for higher flow rates in general, as well as locally where the pore is clogged by deposits of large aggregates.

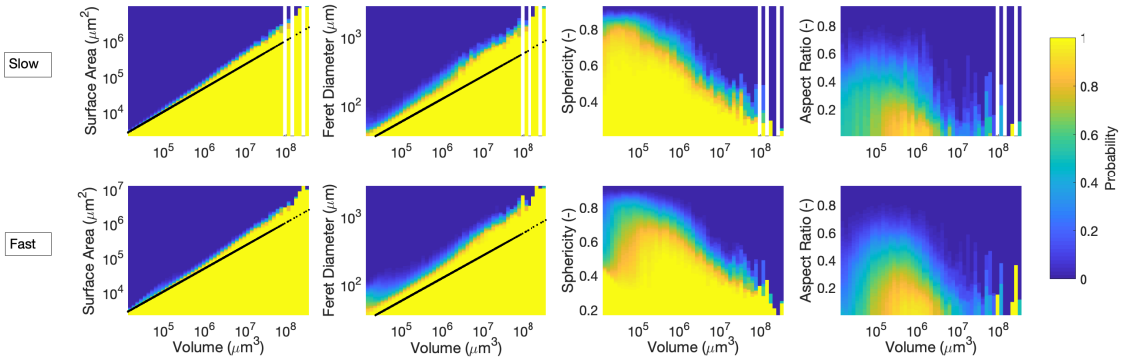

Figure 4-4: Relationship between volume and different morphological characteristics for corresponding aggregates in a given population. Top (bottom) panels correspond to experiments run at slow (fast) flow rates. The coloring gives the probability $p(M_i > M_i'|V)$ that an aggregate of morphology, M_i, of given volume, V, takes a value larger than M_i', where M_i' is plotted along the vertical axis. Reference lines for surface area and Feret diameter of ideal spheres of the same given volume are shown in black. The blank spaces at high values of V indicate the absence of aggregates of such size.

Aggregate distribution in depth

Figure 4-5 presents the joint probability distribution of each aggregate characteristic with depth, $p(M_i, z)$. The probability of finding aggregates of a given size or structural characteristic in depth is shown by the colored equiprobable contours. The contours indicate a higher probability of finding aggregates of large volume, surface area, and Feret diameter near the surface (top) of the column, than at greater depths. This trend is evident in the cone-shaped contours. No dependence on flow rate was observed.1 Conceivably, larger aggregates become strained in the pore space and travel fewer pore lengths, relative to the longer distance traveled by smaller aggregates. We compare $p(V, z)$ (Figure 4-5 first column) with traditional deposition concentration profiles in depth, $S_{Ag} \propto exp(\frac{-kz}{v})$ (see Figure S8 in the SI), which are independent of all aggregate characteristics. Here, S_{Ag} is the concentration of deposited silver, k is the first-order deposition kinetics term, z is depth, and v is the advective term. A stationary exponential profile is predicted by CFT, although hyperexponential profiles have been broadly reported in excavation experiments (e.g., Bradford et al., 2016 [281] and references therein). Given the small dimensions of our column, it is not possible to determine if our observed profiles are exponential or hyperexponential. In either case, $p(V, z)$ sheds light on why the concentration profiles have a (hyper)exponential shape, which is due to the small number of extremely large agglomerates found at shallow depths.

Fast flow rate conditions produce aggregates that approach a spherical shape near the top of the column and become elongated with depth (evident in the cone-shaped contours). In contrast, slow flow rate conditions produce aggregates that are dominantly spherical and show no depth dependency (evident in the vertical contours). These trends in depth are shared for aspect ratio between the two flow rates. Aggregate elongation is likely a result of exposure to higher shear from faster flow rate. High shear could push aggregates deeper in the packed bed, elongate them

with each passed pore throat, and selectively break mechanically weak and porous portions of the aggregate into smaller units that can travel deeper in the column, but are not eluted from it. It cannot be ruled out that local detachment of entire deposits could occur at some locations within the porous medium.

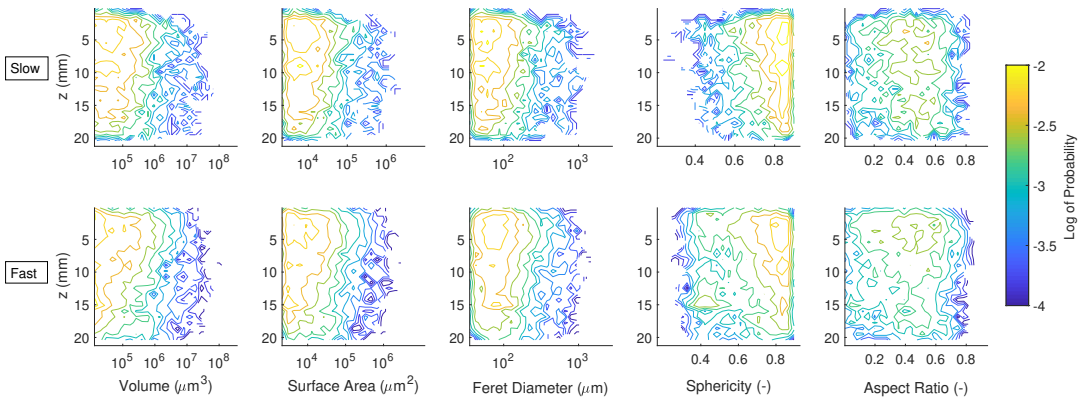

Figure 4-5: Spatial distribution of aggregate morphology characteristics with depth. Top (bottom) panels correspond to experiments run at slow (fast) flow rates. Colored contours give the probability $p(M_i, z)$ that an aggregate of morphology, M_i, is found at depth, z.

Determination of aggregate mechanical strength

Fractal dimension is here used as a metric to quantify an aggregate's mechanical strength and to understand its potential for restructuring by fluid shear. The fractal dimension of the entire aggregate population was smaller for slow, $D_3 = 2.22$ (2.20, 2.24), than for fast flow rates, $D_3 = 2.42$ (2.39, 2.44), where values in parenthesis indicate the 95% confidence bounds (see Figure S9 in the SI). Measurements of fractal dimension of subpopulations at multiple depth increments showed that D_3 did not change significantly with distance traveled by the aggregate (data not shown). It cannot be ruled out that the column might be insufficiently long to reveal the evolution of fractal dimension as a function of depth. The observed fractal dimensions in our aggregates confirms that the aggregation regime was RLA. Recall from the introduction that RLA has a characteristic fractal dimension of ~ 2.1[240, 272]),

with an upper bound close to 2.5 for aggregates that have undergone breakage [272]. For the lower observed D_3, aggregates have a higher potential for restructuring and breaking during porous media transport by the fluid shear to which the deposits are subjected, consistent with prior work [265, 272].

According to the calculations shown in the SI, the shear stress ranges can be coarsely approximated at $[1 \times 10^{-3}, 2 \times 10^{-2}]$ and $[2 \times 10^{-3}, 5 \times 10^{-2}]$ Pa for slow and fast flow rates, respectively. In agreement with conventional wisdom, aggregates exposed to higher shear stress at constant water chemistry are expected to have higher fractal dimensions, and vice versa. This is thought to result from increased breakage and restructuring of low-fractal dimension aggregates into higher-fractal dimension aggregates by the added stress. Previous studies have reported an increase in fractal dimension with flow velocity[103, 282, 261], albeit for a range of velocities that are one or two orders of magnitude greater than the ones used here, which are typical for groundwater. Recognizing that larger aggregates deposit near the surface of a packed bed, it is conceivable that when these deposits have low fractal dimension they could be easily broken by physical or chemical perturbations. This could remobilize aggregates as smaller fragments and promote their transport to greater depths in the porous medium.

4.3.3 Environmental Implications

Colloids often exist in the subsurface as primary minimum aggregates that are formed by the imbalance of stabilizing colloidal forces and the hydrodynamic shear of the flowing water that carries them. Aggregation may significantly reduce particle transport by increasing their hydrodynamic size. However, this study shows for the first time that the resulting aggregate size is power-law distributed, and that the spatial distribution of the very large clusters dictates the concentration depth profile. From a modeling perspective, the broad distribution of particle (aggregate) sizes and com-

paction will affect the transport (single collector) coefficient, but not its attachment coefficient, as outlined in CFT. This implies that colloids undergoing aggregation during transport in porous media move toward collectors by different proportions of CFT-considered transport mechanisms (diffusion, interception, sedimentation). As aggregates grow, they become less diffusive, while as aggregates break and restructure, their density changes affect their sedimentation potential. Experimental results showed that preferential formation of very large deposits of low fractal dimension occurs near the column inlet in steady state conditions. At greater penetration depths and higher shear, aggregates showed evidence for mild breakup and structural evolution. This implies that sporadic release and redistribution of particles during a physical or chemical disturbance is likely to disproportionately affect the small number of very large and frail aggregates near the inlet. Aggregate formation and breakage during realistic transient conditions should eventually produce clusters of stable size and level of compactness. Nevertheless, more detailed characterization of aggregate properties and their location during disturbance events is needed to predict when and where deposits form and become unstable.

Acknowledgement

This work was supported in part by Marie Curie Actions (FP7-PEOPLE-2012-SoilArchnAg), the Social Science Research Council (Sloan Scholars Mentoring Network Grant), and the Hellman Fellowship. The authors thank Dr. Hua Wu for SALS measurements and assistance in data interpretation.

Supporting information

S4-1. Small Angle Light Scattering

The radius of gyration was characterized by SALS following the protocol by Soos et al. [280] as presented below, including equations S1-S3. An example of the measured intensity of scattered light plotted in a normalized form $I(q)/I(0)$ as a function of scattering wave vector q is presented in Figure S4-1.

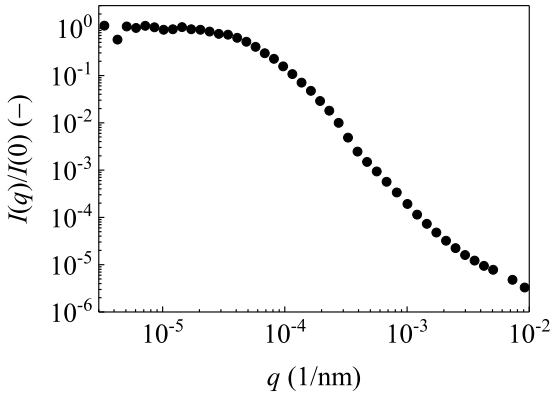

Figure S4-1: Normalized intensity of scattered light, $I(q)/I(0)$, as a function of scattering vector amplitude, q.

Scattering vector amplitude, q, is defined as:

$$q = \frac{4\pi n}{\lambda} sin\Big(\frac{\theta}{2}\Big) \tag{S4-1}$$

where θ is the scattering angle, n is the refractive index of the dispersing fluid, and λ is the laser wavelength in vacuum.

The measured light intensity is analyzed to obtain the rms radius of gyration, $\langle R_g \rangle$, through following expression

$$ln\big(I(q)\big) = ln\big(I(0)\big) - \frac{q^2}{3}\langle R_g^2 \rangle_{I(q)}, \tag{S4-2}$$

where

$$\langle R_g^2 \rangle_{I(q)} = \langle R_g^2 \rangle - \langle R_{g,p}^2 \rangle, \tag{S4-3}$$

and $\langle R_g^2 \rangle_{I(q)}$ and $I(0)$ are estimated from the slope and the intercept, respectively, of the linear relationship between $ln(I(q))$ and $q^2/3$. The mean squared radius of gyration, $\langle R_g^2 \rangle$, is obtained from equation S3 with a radius of gyration of primary particles $R_{g,p} = 7\mu m$.

Note that the tail in $I(q)$ at large q values indicates the presence of a small population of very small particles of size below 100 nm. These are most probably debris from the coating of colloid particles.

S4-2. SEM Images of Colloidal Particles

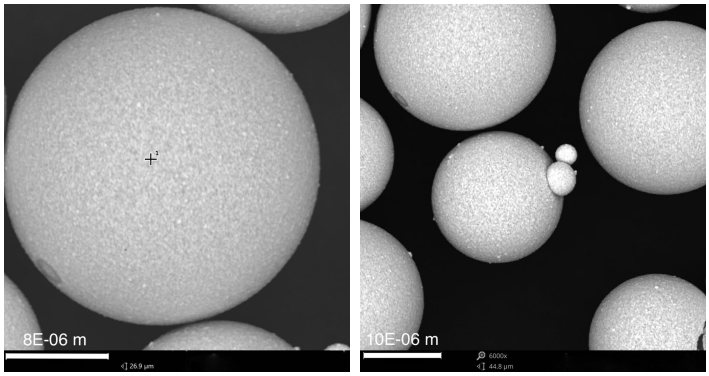

Figure S4-2: Scanning Electron Microscope Images of silver-coated hollow glass microspheres demonstrating mild surface roughness.

S4-3. Estimates for Shear Rate and Stress

A coarse estimate of shear rate and shear stress experienced by colloidal particles traveling in the porous medium is here provided. Shear rate, G, is estimated from information about the distribution of pore channel diameters, D, obtained from structural analysis of the pore space of XCT images and mean pore velocity, v, as[283]:

$$G = \frac{8v}{D}. \tag{S4-4}$$

Mean pore velocity is defined as:

$$v = \frac{Q}{An}, \tag{S4-5}$$

where Q is the flow rate, A is the cross-sectional area of the column and n is the mean porosity.

Distributions of the shear rate for slow and fast flow rate experiments are provided in Figure S4-3.

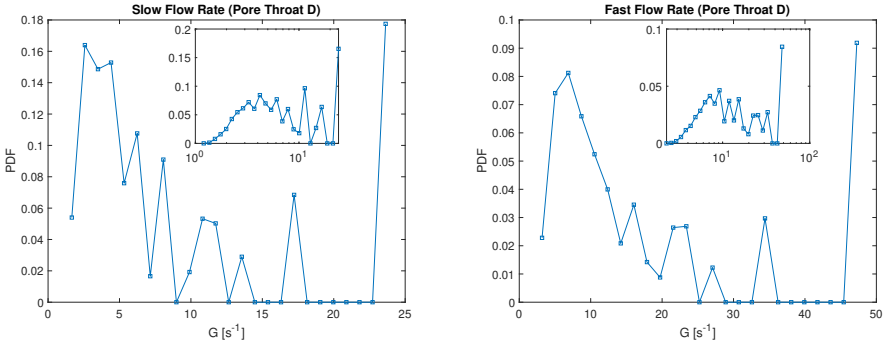

Figure S4-3: Distribution of shear rate for slow (L) and fast (R) flow rates. Insets display the same data in semi-log.

Shear stress, τ, is given by Newton's law of viscosity:

$$\tau = \rho\nu G, \tag{S4-6}$$

where ρ is the fluid density, and ν is the kinematic viscosity.

For example, to induce aggregation in a colloidal suspension of nano-roughness of $h_r = 50nm$ and $f = 3\%$, the hydrodynamic shear F_s must exceed the repulsive force $F_m = 2.78 \times 10^{-10}$. The hydrodynamic force requirement in each of the flow rates tested is met in 31% of the available channels in the medium for fast flow rates, and in 16% of the available channels in the medium for slow flow rates. This is equivalent to

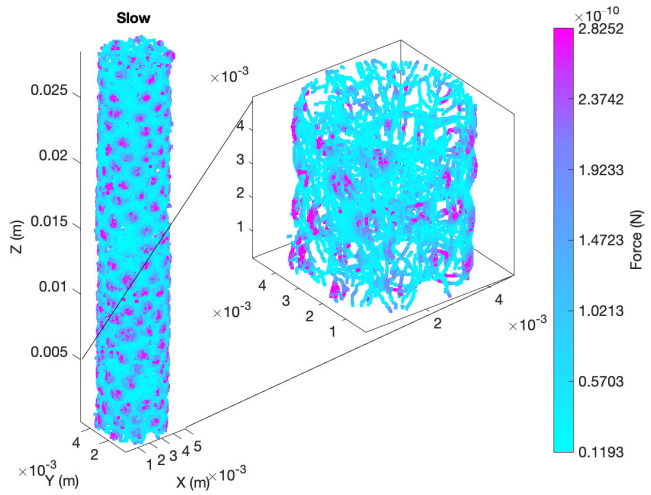

Figure S4-4: Frequency of hydrodynamic shear force occurrence for slow flow rates within the pore network.

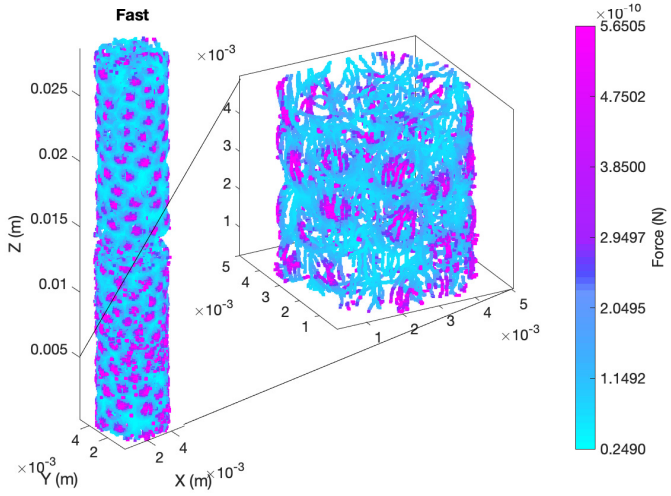

Figure S4-5: Frequency of hydrodynamic shear force occurrence for fast flow rates within the pore network.

17 times per mm^3 of the medium for fast, and 8 times per mm^3 of the medium for slow flow rates. Figures S4-4 and S4-5 illustrate the overall distribution of hydrodynamic forces in the column at their respective flow rates.

S4-4. XCT Image Analysis Quality Controls

Two quality controls were performed in the XCT images to (i) determine the threshold signal-to-noise ratio that can be used to *conservatively* filter data for morphology analysis to aggregates of interest, and (ii) evaluate the column verticality, which would skew the spatial distribution of aggregates in x and y planes.

Noise reduction: Impurities of the bulk materials used for transport experiments, general noise from the polychromatic X-ray source and detector, and partial volume effects collectively create noise in the tomographic images. This greatly complicates segmentation of very small silver colloid aggregates in our data. Nevertheless, to take advantage of this imaging technique, which can resolve larger clusters well and with high certainly, a threshold aggregate volume of 10 primary particles (i.e., the volume necessary to contain 10 primary particles) was used to conservatively filter out noise. True noise is expected to be evenly distributed throughout the interrogation volume and should thus be able to be subtracted from the silver aggregate signal of interest, as this is known to have a depth dependence. To determine a suitable threshold value of too small aggregates to be distinguished from noise, we evaluated the spatial distribution (centroid) of clusters smaller than various threshold values of primary particle numbers and checked for uniformity in spatial distribution. A threshold of 10 primary particles was chosen as the largest filter size that yielded an even spatial distribution in x and y, with random distribution in z (see Figure S4-6). Such a value is conservative and excludes the smallest aggregates from analysis.

Aggregate uniformity in x,y planes Tilting of the column from perfectly vertical position during experimentation can significantly skew the distribution of aggregates in the x and y axes. To evaluate column verticality, and therefore quality of data, the centroid of aggregates $>$ 10 primary particles were checked for uniformity along the cross section of the column. As shown in Figure S4-7, aggregates in the x and y

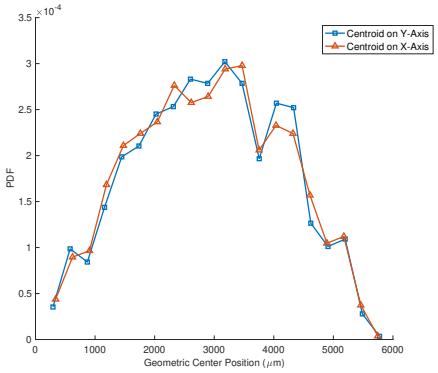

Figure S4-6: Representative spatial distribution (x, y, and z) of aggregates of <10 primary particles along individual axes of the column.

planes (aerial view of the column) are confirmed to be uniform. Hence, the spatial analysis of aggregate deposition is confidently limited to the z axis (column depth).

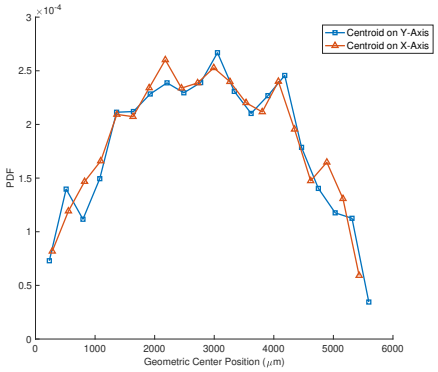

Figure S4-7: Representative spatial distribution (x, y, and z) of aggregates of ≥10 primary particles along individual axes of the column.

S4-5. PDF Parameters of Various Aggregate Morphology Characteristics

Table S4-1: Global Probability Distribution exponent values for volume (V), surface area (SA), and Feret diameter (Fe). Mean and variance values for aspect ratio (AR) and sphericity (ψ).

	V	SA	Fe	AR		ψ	
Flow rate	Exponent			Mean	Variance	Mean	Variance
Slow	-0.656	-0.901	-0.0028	0.767	0.00018	0.450	0.00098
Fast	-0.695	-0.960	-0.0032	0.631	0.00072	0.393	0.00184

S4-6. Depth Profiles in Concentration

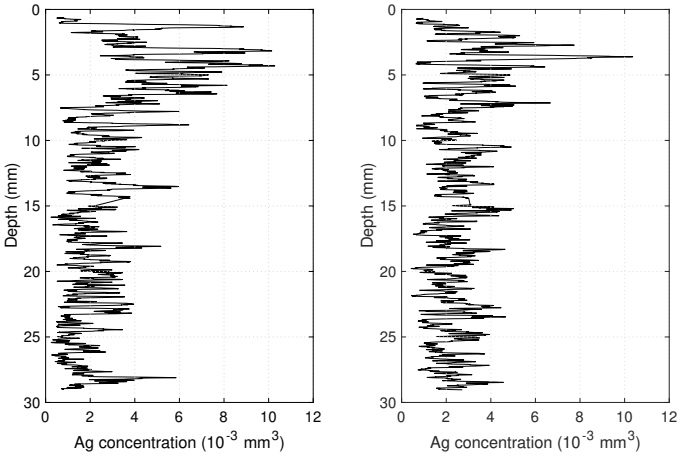

Figure S4-8: Representative depth profile for slow (L) and fast (R) flow rate conditions.

S4-7. Fractal Dimension

S4-8. Raw Data

Enclosed files contain raw data for the experiments here conducted. Files labeled Fast_i.xls or Slow_i.xls contain the morphological characteristics evaluated for each aggregate in a given experiment i as analyzed with the BoneJ plugin, Particle Analyser tool from FIJI. The latter portion of the file name reports the experiment's voxel size in μm. Blank spaces in select files indicate the removal of data at edges (top/bottom) of individual scans where reconstruction is of poor quality and noise signal is high.

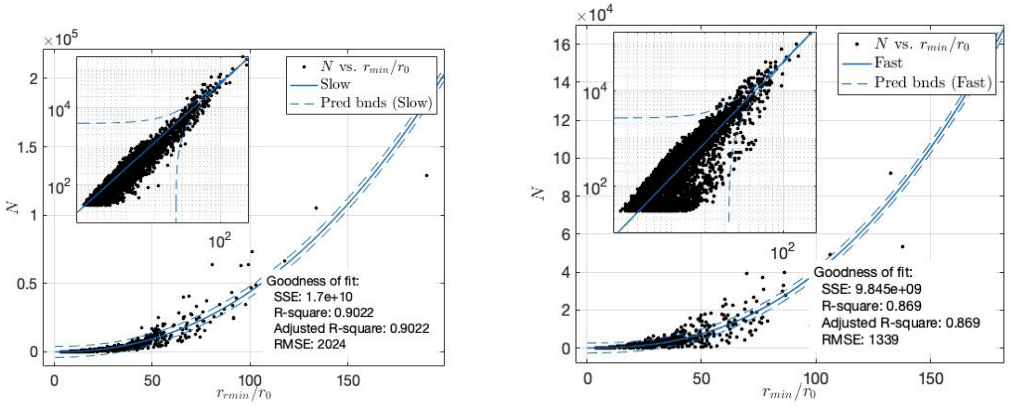

Figure S4-9: Relationship between number of primary particles in an aggregate (N) and the normalized radius of the aggregate cluster by the primary particle size (r_{Min}/r_0). Slow flow rate (L), fast flow rate (R). Inserts show the data in log-log space.

Reconciling Mechanisms of Retention with Fate of Particles in Saturated Granular Media in the Presence of Chemical Heterogeneity

Janis E. Patiño[1], William P. Johnson[2], Verónica L. Morales[1]

[1] Department of Civil and Environmental Engineering, University of California, Davis

Davis, United States

[2] Department of Geology & Geophysics, University of Utah,

Salt Lake City, United States

Abstract

The expanding use of engineered colloids in consumer products leads to undesirable amounts of nano- and micro-size particles in soils from wastewater effluent discharge. The capacity of soils to filter colloidal particles depends on multi-scale processes that are neither well understood nor accurately upscaled in predictive models. We compare laboratory experiments against a mechanistic modeling framework able to upscale emerging processes from the interface-, to the collector-/pore-, to the Darcy-scale. We demonstrate that the soil surface chemical heterogeneity and the residence time of colloidal particles within the near surface fluid domain significantly affect particle retention and cause anomalous macroscale transport. At the interface-scale, we revise the interaction energy profiles considering chemical heterogeneities of the collector surface. We use X-ray computed tomography to identify where the colloids accumulate at the pore-scale after being injected through glass bead packed columns. Thus, observations of deposited colloids in space are contrasted against continuum-scale predictions parameterized from rate coefficients upscaled from modeled Lagrangian trajectories. Our results indicate that: i) Colloid-collector interaction energies are non-unique for heterogeneous systems and can span from strongly repulsive to strongly attractive depending on the region of the soil surface that the colloid

encounters; ii) The particle status predicted by the model (e.g. attached, near surface, exited) explain the observed site-specific retention at the pore-scale; and iii) Simulated anomalous depth profiles of retained colloids and heavy-tailed breakthrough elution curves are in agreement with experimental non-monotonic depth profiles after considerations of the wide range of surface interactions and the broad residence time distributions of particles in the near-surface water.

5.1 Introduction

The fate of naturally-occurring as well as engineered colloids in soils is a topic of environmental and public health concern. Depending on their origin and composition, their presence in the subsurface can be either viewed as beneficial (e.g. iron oxide nanoparticles used in remediation strategies [19, 17]) or detrimental (e.g. viruses and toxic engineered nanomaterials [150, 33, 32]). For example, silver colloids employed in the fabrication of detergents and anti-odor clothing (because of their biocidal properties [119, 120, 121]) have been found in wastewater effluents [124, 125], thus raising concern regarding their presence in agricultural soils [23, 25, 122, 123]. However, prediction of the fate and of the distribution of colloids in soils and in porous media in general is often inadequate, due to deficient understanding of the physico-chemical processes governing transport and retention.

The mass transfer of particles between the liquid and solid phases that govern the filtration of colloids in soil-groundwater systems is a multi-scale problem. Nanoscopic interactions that arise among the surfaces of particles and soil grains (collectors) dictate how likely the colloids will deposit onto the collector surface in absence of a flow field. When both surfaces are like-charged, an energy barrier typically hinders deposition onto the collector surface. This situation is commonly observed in natural as well as engineered systems, since the surfaces of both colloids (e.g., bacteria, protozoa, viruses, engineered nanoparticles) and collectors (e.g., quartz minerals) tend to exhibit a net negative charge at near neutral pH [15]. Nonetheless, evidence has been repeatedly reported that shows particle retention under these so-called unfavorable

conditions for deposition [91, 105, 106, 107, 108, 109, 110, 111]. Such observations suggest the presence of at least some favorable colloidal interactions, thus questioning the applicability of classic colloid filtration theories [84]. The use of average values of energy interactions and flow fields allows for the straightforward application of classic filtration theories, but the latter have been shown to fail even under controlled experimental conditions (e.g. chemically cleaned glass and quartz. Therefore, using average values may be responsible for inaccurate predictions in circumstances comprising varied and complex surface chemistry and hydrodynamics conditions, such as typically found in natural environments.

In detail, nanoscopic interactions among colloids and the surface of the collectors are traditionally modeled by Derjaguin-Landau-Verwey-Overbeek (DLVO) theory[56, 129], and more recently by extended DLVO, which considers interactions additional to electric-double layer and van Der Waals (e.g., Born repulsion, Lewis acid-base interactions) [284, 112, 285]. A determinant input of these energy calculations is the average surface charge of the materials of interest, which is often replaced by the approximated ζ potential. Although this approach qualitatively predicts experimentally observed trends in retention [112], it fails to incorporate information on nano-to-microscale chemical heterogeneity on regions of the materials where the surface charges might differ from that of the bulk, locally reducing or eliminating repulsion. As stated by Duffadar et al., (2009), all naturally-occurring surfaces are heterogeneous, with great chemical and topographical diversity, which leads to the concurrent existence of both favorable and unfavorable colloidal interactions [286, 112, 111, 48, 287, 113]. Thus, the development of transport models that reflect the stochastic nature of interfacial, and consequently, pore scale interactions between particles and the granular media has become crucial to improve predictions and control of colloid fate in porous media [112, 111, 287, 113, 114, 115].

While interfacial particle-collector interactions are relevant at separation distances

of tens to hundreds of nanometers [58], flow properties are relevant at the pore scale and particle distribution are the ultimate results of filtration at the Darcy scale. Classic theories utilize two independent parameters to account for the probability of flow-based particle approach to collectors and interaction-based attachment, namely, η_0 and α, respectively. Their product yields the deposition probability and is used to calculate the deposition rate coefficient k of the entire (upscaled) porous media, assuming first-order deposition kinetics [46, 48, 162]. For example, the classic filtration theory (CFT) model yields (i) retained colloid concentrations (depth profiles, DP) that decrease exponentially with distance from the source and (ii) symmetric breakthrough-elution concentration histories (BTC). Nonetheless, non-exponential DP shapes (e.g., hyper-exponential, uniform, non-monotonic) and asymmetric long-tailed BTC have been observed under unfavorable conditions [91, 105, 106, 107, 108, 109, 110, 111], suggesting transport dynamics that are not well-captured by k as proposed by classic theories. Recent descriptions of the system that can account for such anomalies have comprised statistically distributed fluid velocities and k values to represent the effect of structural heterogeneity on particle transport [288], as well as the combined use of the k for fast deposition with additional rates for slow deposition and for particle retention at the near surface fluid domain [116, 115, 15]. In particular, the latter approach is based on the complete balance of forces (energy interactions) and torques (hydrodynamics) prevailing for the colloids at every location along each Lagrangian trajectory, which dictates the probability of deposition and re-entrainment, and ultimately the distribution and fate of the colloids. That being said, further efforts are needed to, on the one hand, provide experimental observations of particle fate strengthening the validity of this approach and, on the other hand, understand the significance of the modeled mechanisms in different systems and circumstances.

The overarching objective of this work is to demonstrate how predictions of colloid fate at the Darcy scale benefit from considerations of the mechanistic processes taking

place at the collector, pore, and interface scales. Specifically, we aimed to describe the transport mechanisms of colloids moving through an average unfavorable porous medium in the presence of surface heterogeneity. We use controlled column experiments combined with detailed XCT imaging and a mechanistic model to i) explain the observed deposition behaviour of silver colloids by considering a wide range of interfacial energies of interaction for colloids and collectors; ii) determine the mechanisms driving colloid immobilization at available pore-scale retention sites and; iii) predict anomalous transport behavior as non-exponential depth profiles and BTC with extended tailing using trajectory simulations based on the Lagrangian solution of forces and torques with explicit consideration of the near surface fluid domain.

5.2 Materials and Methods

A link between the mechanisms responsible for colloid retention in porous media (from model simulations) and their fate (from experimental observations) is drawn at relevant scales covering the interface, collector, pore, and Darcy. Simulations are performed with the mechanistic model Parti-Suite (PS) (https://wpjohnsongroup.utah.edu /trajectoryCodes.html), which upscales interfacial interactions based on xDLVO, computes attachment efficiencies from Lagrangian particle trajectories in a Happel-sphere geometry, and estimates macroscopic transport behavior as detailed depth profiles and breakthrough curves from explicitly estimated deposition rates based on smaller-scale statistics. Experiments from a silver colloid slug transported in a fully water saturated glass bead column under unfavorable conditions from Patino et al. (2022) [289] are used for ground truth comparison. Briefly, the available data provide the mean-average ζ-potential of each material with which interface-scale energy potentials are estimated, pore-scale spatial distribution of retained colloids from high-resolution X-ray computed tomography (XRCT) imaging of the column, and Darcy-scale depth profiles of retained materials along the column depth. Input pa-

rameters for simulations were specified to be consistent with the experimental setup. Figure 5-1 illustrates the workflow at different spatial scales.

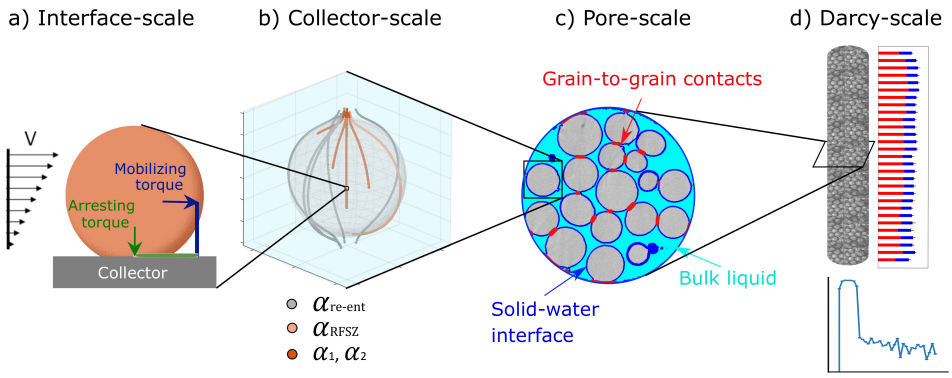

Figure 5-1: Upscaling schematic for colloid transport in a porous medium. a) Velocity profile and the torques acting over a single colloid near the collector surface (modified from VanNess et al., 2019)[290]. b) Lagrangian colloid trajectories within a representative elementary volume, a single collector with flow, as encoded by their final status. c) Pore-scale retention sites where colloids can accumulate (from [289]). d) Column packed with collectors from which depth profiles and breakthrough signals are recovered.

Interface-scale: Interaction Energy profiles

Energy profiles of interaction between the silver colloids with surface roughness and glass beads with chemical microsites were estimated with the xDLVO module of PS [111].

Custom-made hollow glass microspheres coated in a layer of 118 nm silver were used as the silver colloids for experimentation (Microsphere Technology, Limerick, IE). According to the manufacturer, the silver-glass-air spheres have a radius, $r_p = 7.0{\times}10^{-6}$ m. Borosilicate glass beads of $1.0{\times}10^{-3}$ m mean diameter were used used as the porous medium for transport experiments (Sigma-Aldrich). The average (measurable) ζ-potential of the silver microspheres and glass beads is considerably negative (-50 and -65 mV, respectively) [289]. We hypothesize that positively charged sites microsites are present on the collector surface, herein referred to as collector chemical

heterodomains (CCHD), given the observed particle deposition in these otherwise unfavorable conditions. Locally-attractive regions within net-repulsive, heterogeneously-charged surfaces have been previously postulated to explain retention in net-repulsive systems [287, 291, 292]. In the absence of available direct measurements for CCHD ζ-potential, we set its value to the opposite charge of the average grain surface (+65 mV). Rasmuson et al., 2019 [293] have reported that the primary control for attractive interactions between colloids and the collector is the presence of CCHD, not the magnitude of their ζ-potential. Scanning electron microscopy (SEM) images of the silver microspheres suggest a mild level of surface roughness (refer to Figure S5-1). Colloid asperities are therefore represented in the model as contiguous hemispheres with 20 nm height based on the relationship between particle size and asperity height from Rasmuson et al., 2019 [293]. Table S3-2 summarizes all input parameters for the XDLVO module for PS.

The system represented is that of silver colloids interacting with glass beads immersed in water (or colloid-solid-water interface, colloid-SW) in the presence of surface heterogeneity. The sum of van der Waals (V_{VDW}), electric double layer (V_{EDL}), steric (V_{ST}), and Lewis acid-base interactions (V_{AB}) are here considered [239, 240, 161, 162, 241, 242]. The analytical expressions for the various interactions (in sphere-sphere geometry) are provided in Equations S1 to S5-4. The most unfavorable conditions for colloid-SW interactions take place when the entire zone of interaction between particles and collectors (ZOI) falls outside the CCHDs. The ZOI is the effective contact area over which a colloid and the collector interact. The ZOI's size, $R_{ZOI} = 2\sqrt{\kappa^{-1} r_p}$, is controlled by the Debye length of the solution κ^{-1} and the particle radius r_p [286]. Conversely, the most favorable conditions for colloid-SW interactions occur when the ZOI completely overlaps with a heterodomain region. All colloid-SW interactions are contained within these two extreme scenarios.

Collector-/Pore-scale: Particle Trajectories and Retention sites

Trajectory simulations of particles traveling through a Happel-sphere geometry (a representative elementary volume of a porous medium) were performed using the Traj-Hap module of PS. Briefly, Lagrangian trajectories are built as per the force-torque balance between colloid-SW interactions and the flow field hydrodynamics (see Figures 5-1a and b).

Particle trajectories were used to calculate the collector efficiency of the system, η, as the fraction of introduced colloids that enter the near-surface pore water (separation distance between particles and collector $<$ 200 nm [113, 116], approximately the thickness of the hydrodynamic boundary layer). Once the particles reach this region, they can either deposit onto the collector surface by fast or slow attachment, re-enter to the bulk pore water, or slowly slide/roll along the collector surface without attachment until reaching the rear-flow stagnation regions. These number fractions are used to determine α_1, α_2, $\alpha_{re\text{-}ent}$, and α_{RFSZ}, respectively, and are subsequently used to estimate multi-rate coefficients in the advective-dispersive reactive model described below.

Simulations were conducted for 5000 trajectories of singlets ($r_p = 7 \times 10^{-6} m$), triplets ($r_p = 1 \times 10^{-5} m$), and tenplet particle aggregates ($r_p = 1.5 \times 10^{-5} m$), to account for the polydispersivity of the suspension used here, as was determined experimentally in earlier work [209]. Chemical heterodomains of 500 nm were uniformly distributed onto the collector with a surface coverage of 2%. The size of the CCHD and the surface coverage were estimated from the size of the primary particles and the size of the collector following the recommendations in Ron et al. (2019) [113]. Trajectories were generated for two particle densities, $\rho_p \in$ [1.00, 1.03] g/cm^3 since the value declared by the manufacturer (ρ_p=1.00 g/cm^3) is considerably low for colloidal particles and sedimentation of the suspension was observed over time. Table S5-3 summarizes all input parameters for the collector-scale module for PS.

Experimentally-observed spatial distribution of colloids at the pore-scale were used to set the reference for the effective regions where particles are retained. Briefly, X-ray computed tomography (XCT) imaging of the column was conducted to obtain a detailed three-dimensional map of pore structure of the medium and the spatial distribution of retained particles within it. Image segmentation was used to first define the bulk phases: *solids*, *water*, and the total retained *silver colloids*. Then, a sequence of image operations was applied to define regions of interest (ROIs) corresponding to the *solid-water interface* (SW) and the *grain-to-grain* (GG) contacts. A *bulk liquid* (BL) element was designated as the difference between the *water* element and the SW and GG sites. This pore-region captures any retained silver mass that is not anchored to a retention site and will likely breakthrough the column with sufficient time. To summarise, we detect ROIs corresponding to three types of retention sites, $\mathcal{S} = \{\text{SW, BL, GG}\}$. Figure 5-1b illustrates in false coloring the ROIs for each retention site available within the column [289]. At this scale, a direct comparison is drawn between the mechanistically-predicted particle locations in the model and the mass distribution in the experiments.

Darcy-scale: Deposition profiles and BTC

Detailed depth profiles and breakthrough curves for the system were simulated with the Upscale-Continuum module of PS. The one-dimensional advective-dispersive reactive model is based on the following set of governing equations.

$$\frac{\partial C}{\partial t}\theta_b = D\frac{\partial^2 C}{\partial x^2}\theta_b - v\frac{\partial C}{\partial x}\theta_b - \alpha_1 k_f C\theta_b - (1-\alpha_1)k_{ns}C\theta_b \tag{5-1}$$

$$\frac{\partial C_{ns}}{\partial t}\theta_b = (1-\alpha_1)k_{ns}C\theta_b - v_{ns}\frac{\partial C_{ns}}{\partial x}\theta_{ns} - k^*_{f2}C_{ns}\theta_{ns} \tag{5-2}$$

$$\frac{\partial S}{\partial t}\rho_b = \alpha_1 k_f C\theta_b + k^*_{f2}C_{ns}\theta_{ns} \tag{5-3}$$

Here, C is the concentration of colloids in suspension, t is time, θ_b is the volumetric water content of bulk fluid in the representative elementary volume, D is the hydrodynamic dispersion coefficient, x is distance along the column depth, v is the advective pore velocity, α_1 and k_f are the fraction and particle deposition rate coefficient of fast-attaching colloids, k_{ns} is the rate coefficient for net transfer to the near surface, C_{ns} is the concentration of colloids in the near surface, v_{ns} is the near surface fluid velocity determined from the residence time of the slow-attaching colloids [115], θ_{ns} is the volumetric water content in the near surface fluid in the representative elementary volume, k^*_{f2} is the rate coefficient for attachment of near surface colloids when the near surface fluid domain is explicitly simulated, S is the concentration of retained particles, and ρ_b is the bulk density of the medium. Note that the total volumetric water content in the representative elementary volume is $\theta = \theta_b + \theta_{ns}$.

The various rate coefficients were estimated considering the porous medium as a series of collectors of identical diameter d_c in accordance to traditional colloid filtration theory [46, 116, 115]. Consequently, k_f, k_{ns} and k^*_{f2} were explicitly calculated viz:

$$k_f = -\frac{3(1-\theta_b)^{1/3}}{2d_c} ln(1-\eta)v \tag{5-4}$$

$$k_{ns} = -v^* \frac{N_c}{L} ln(1-\eta(\alpha_2 + \alpha_{RFSZ} + \alpha_{re\text{-}ent}) \tag{5-5}$$

$$k^*_{f2} = -2\frac{v_{ns}}{\pi d_c} ln(1-\eta\alpha_2) \tag{5-6}$$

where v^* is the characteristic velocity for scaling particle transfer to near-surface pore water (geometric mean between v and v_{ns}) [115] and N_c/L is the number of collectors per unit length.

By parameterizing the model with the above listed rate coefficients and setting the initial and boundary conditions to those used in the experiments (see Table S5-4), we obtain the deposition profiles (DP) and breakthrough curves (BTC) for each aggregate

size tested (singlets, triples, tenplets). The DPs are obtained for the total mass of retained material in depth, and also differentiated by the mechanism responsible for retention. A second set of simulations was executed at a time three times longer than the experimental duration to assess the heavy tail of the BTC. The results of the individual aggregate size simulations were combined to produce a final DP and BTC of a homoaggregated polydispersed system. The assumptions made are that the deposition phenomena is additive across polydispersed suspensions and that particle-particle interactions are negligible.

Experimental data a the Darcy-scale is focused on the DPs, which are provided both as the total mass of retained material in depth, and also differentiated by the specific pore-scale retention-site where the particles were found (SW, GG). BTCs from experiments are not available for comparison. At this scale, a link is made between the depth distributed mechanisms (from simulations) and retention-site locations (from experiments).

5.3 Results and Discussion

5.3.1 Colloid-SW Interactions

Figure 5-2 shows the range of theoretical net energies of interaction for a colloid approaching the surface of a collector with chemical heterogeneity as an area plot. We argue that this representation is more appropriate than a single interaction profile when CCHDs are present. This is because the local charge at play, and therefore net interaction, can vary as the ZOI samples different portions of the surface with CCHDs (see insert of Figure 5-2).

The dashed line in the plot illustrates the repulsive limit in our system. That is, the interactions between a silver colloid with -50 mV surface charge and a region of the collector surface with a local charge of -65 mV. The energy barrier in this

extreme case reaches values of $\mathcal{O}(10^3)$ kT, which suggests negligible particle deposition. Conversely, the solid line illustrates the attractive limit herein considered. This represents interactions between a silver colloid with -50 mV surface charge and a region of the collector surface with a local charge of +65 mV. All intermediate colloid-collector interactions in our system are contained within these limits, and depend on how much the ZOI overlaps with a CCHD and whether the CCHD is large enough to generate a net attractive interaction. Altogether, the unique interactions a colloid experiences with the heterogeneous collector are stochastic and therefore require a modeling framework that can account for such variability.

Representing chemical heterogeneities is not straightforward as there is not yet an established way for their measurement and characterization [286, 115]. Nonetheless, representing a wider range of interfacial interactions in models is already an improvement to mean-field approaches, where the average (effective) charge of the collector surface is used to represent the unique interaction profile between a colloid and a collector. Such an approach omits the occurrence of some attractive interactions among the surfaces of particles and collector and thus, underestimates the overall colloid filtration efficiency[286].

5.3.2 Particle Immobilization Mechanisms

Figure 5-3 shows as a pyramid plot the simulated particle mechanisms as a percentage of the total amount of particles injected (left hand side) and the experimentally-observed colloid distribution (fate) within the porous media (right hand side).

The results from upscaling simulations (Figure 5-3, left hand side) indicate that of the injected particles, $> 60\%$ are eluted or *exited* from the porous medium (grey bar), $\sim 38\%$ *attached* to the collector surface (orange bar), and a small fraction ($< 1\%$) persist in the *near surface* of the collector grains without proper attachment (tan bar). The latter fraction accounts for the mass that remains in the near surface

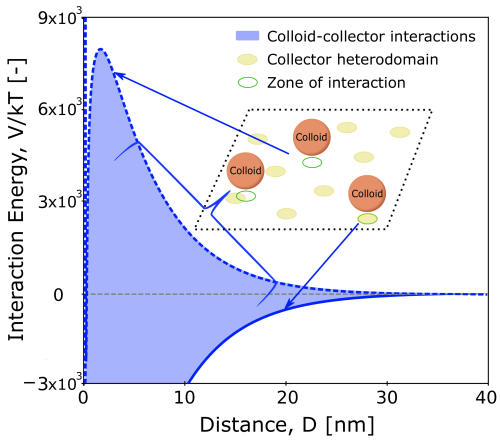

Figure 5-2: Total interaction energy as a function of separation distance for a colloid approaching the surface of a collector (solid-water interface) with surface heterogeneity. The dashed line shows the upper repulsive limit for the case where the zone of interaction between colloid and collector completely avoids heterodomains. The solid line shows the lower attractive limit for the case where the zone of interaction between colloid and collector falls completely within an oppositely charged heterodomain. The majority of interactions are expected to fall between these two limits. The insert shows a schematic of three types of interactions possible.

for long enough to be dragged or rolled by the flow to so-called rear flow stagnation zones. The error bars for these data indicate the variability in particle status percentage for particle density uncertainty ($\rho_p \in [1.00, 1.03] g/cm^3$). Additional simulations were also conducted to assess immobilization trends in the absence of CCHDs, equivalent to a homogeneous collector of uniform average charge (see Figure S5-3). This approach predicts that 99.99% of the mass *exited*, 0% *attached* and 0.01% retained at the *near surface*. The lack of attachment is attributed to a consistently larger mobilizing torque than the arresting torque everywhere along the collectors surface under homogeneously unfavorable conditions. Although a substantial fraction of injected particles arrive at the near surface, an insurmountable repulsion restricts attachment entirely.

The results from experimental observations of accumulated particles by pore-scale retention site are shown in Figure 5-3, right hand side. About 50% of the injected mass was associated with the *bulk liquid* at the end of the transport tests (cyan bar),

which represents particles found in the effluent breakthrough and particles that are not attached, but were not flushed out long enough to exit the column. Approximately 35% of the particles were found at the *solid-water interface* (blue bar), where it is expected that they have been properly attached. And, around 10 % of the injected mass was accumulated at *grain-to-grain contacts* (red bar).

Overall, the percent magnitudes of mechanistically-predicted particle locations are in very close agreement with the experimental observations of silver retained at different pore-scale locations (cf. symmetry in the left and right side of Figure 5-3). The percent of exited colloids in simulations is comparable to that of colloids found in the bulk liquid for experiments (gray and cyan bars, respectively). In this scenario, the particles experience mobilizing torques that are greater than those required for arresting and are thereby able to exit the column entirely or avoid retention for the duration of the test. The percentage of attached colloids in simulations is comparable to that of experimental colloids found at the solid-water interface (orange and blue bars, respectively). In this scenario, particles experience a greater arresting torque than the mobilizing torque, which allows a particle that is on the collector surface (the solid-water interface) to become formally attached. Lastly, the percentage of simulated colloids at the near surface is comparable to that of experimental colloids found at the grain-to-grain contacts (tan and red bars, respectively). In this scenario, a near balance between mobilizing and arresting torques allows particles to remain at the near surface without physically contacting the collector. This causes colloids to roll toward rear flow stagnation zones in the simplified Happel-sphere geometry or toward grain-to-grain contacts for porous media with structure. The discrepancy in magnitude between this transport mechanism and its corresponding fate is likely due to particles at grain-to-grain contacts that have spent long enough times at such regions to become properly attached at CCHDs in that vicinity. That is, some of the particles that are attached are found at both the solid-water interface and at

grain-to-grain contacts.

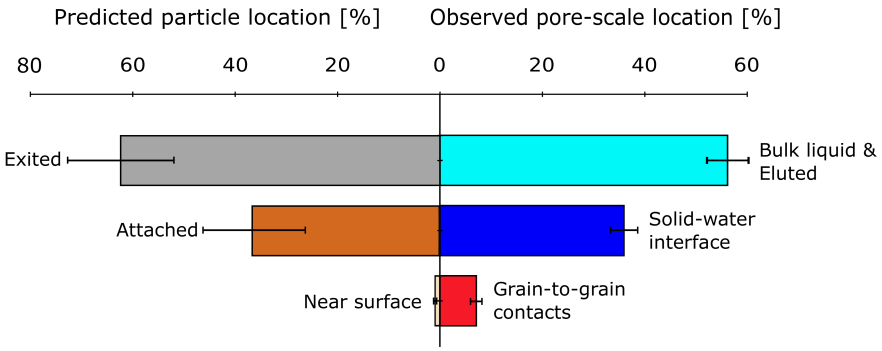

Figure 5-3: Particle location predicted from the model simulations vs. particle distribution over pore-scale locations obtained from XRCT.

5.3.3 Anomalous Depth Profiles & Long Elution Break Through Curves

Figure 5-4 presents deposition profiles of retained colloids along the porous medium depth in the presence of CCHD for both simulations and experiments. Stacked bar charts are used to illustrate the proportion of particles retained by mechanism (in simulations) or by pore-scale location (in experiments) at each discretized depth. The the error bars represent variability on the total mass due to particle density (for simulations) and between replicates (for experiments).

Simulated DPs (Figure 5-4a) exhibit a non-exponential trend with depth (a sign of anomalous transport), capturing $\sim 40\%$ of the injected mass. Here, we find that retention by attachment occurs at all depths (orange stacks) and that a consistently small but significant amount of particles are associated to the near surface (tan stacks) at depths greater than one third the column's total depth. Experimental DPs (Figure 5-4b) also exhibit a non-exponential (more precisely, a non-monotonic) trend with depth, capturing $\sim 43\%$ of the injected mass. In this case, the majority of retained mass is found at the solid-water interface (blue stacks) with a depth-uniform

contribution of mass immobilized at grain-to-grain contacts (red stacks).

Figure 5-5 depicts the simulated breakthrough curves of colloids eluted from media with (gray solid line) and without (green dashed line) CCHDs. In the presence of CCHDs, the concentration signal shows exponential tailing (another sign of anomalous transport) and $\sim 63\%$ of the injected mass is eluted from the system at the end of the simulation time (see Table S5-4. This is in close agreement with the percentage of mass that was not retained experimentally (Table S5-4). By contrast, in the absence of CCHDs, the concentration signal is devoid of tailing and the entirety of the injected mass is eluted from the system. This is inconsistent with experimental mass balances. Together, the non-exponential DP and heavy tailed BTC suggest anomalous transport behavior when surface heterogeneities are present. In this system, this is attributed to broadly distributed colloid residence times, which are prolonged during particle associations with the near surface of a filter medium dotted with CCHDs. Importantly, our simulations show that heavy tailing results mainly from reentrainment of near surface associated particles and is rarely produced from kinetic detachment processes.

Although simulated and experimental DPs are consistent in terms of magnitude and shape of the total mass deposited, some apparent depth-dependent mismatches between mechanisms and pore-scale fate remain to be clarified. Specifically, simulated DPs indicate that at shallow depths particles are all attached, not accumulating at the near surface water, while experimental DPs show particle retention at both solid-water interface and grain-to-grain contacts close to the inlet. Considering that particles at shallow depths have spent the longest time in the domain during the test, it is conceivable that some colloids initially associated with the near surface became funneled to grain-to-grain contacts where they are eventually able to find a CCHD to properly attach to, or became reentrained with the bulk flow. Importantly, the heavy tailed BTC demonstrates that even in a simple flow field, the presence of

CCHDs facilitates the entry of particles to hydrodynamically stagnant zones where they may very slowly become released back into the main flow paths (a pseudo equilibrium retardation process) or become permanently retained by proper attachment to a heterodomain if given the necessary time to find one.

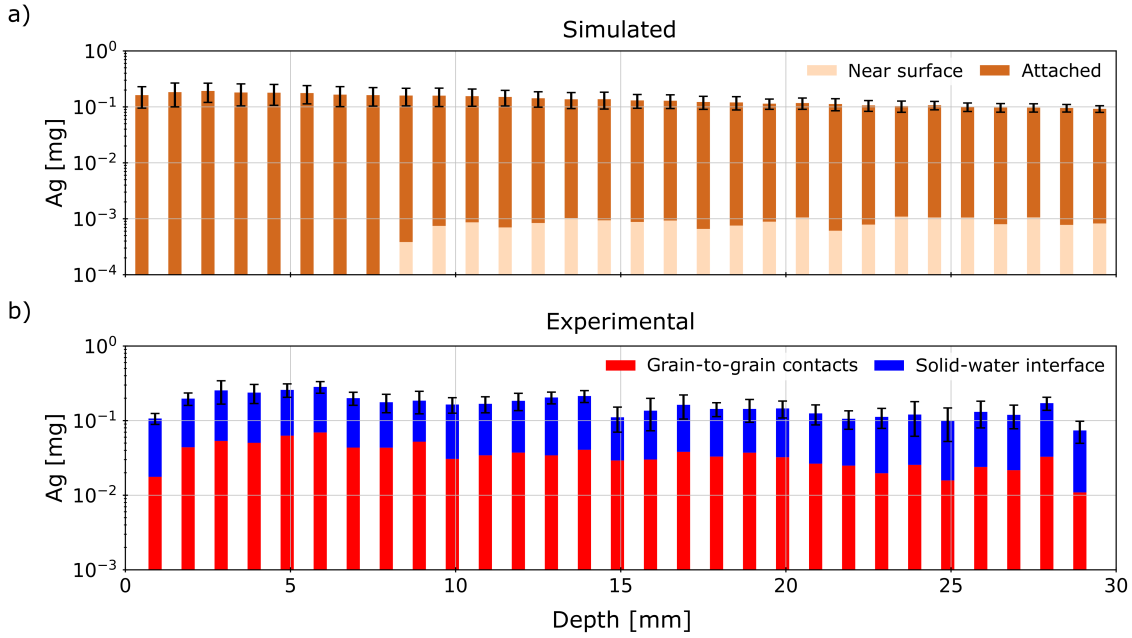

Figure 5-4: Stacked bar plots of deposited silver colloids in depth shown by their simulated retention mechanism (top) and experimentally observed pore-scale retention site association (bottom). a) For simulations, the fraction of particles that are properly attached is shown in orange and that associated with the near surface is shown in tan. Error bars represent total retained mass variability due to the particle density. b) For experiments, the fraction of particles retained at the solid-water interface is shown in blue and that associated with grain-to-grain contacts is shown in red. Error bars represent variability on the total silver for replicate experiments.

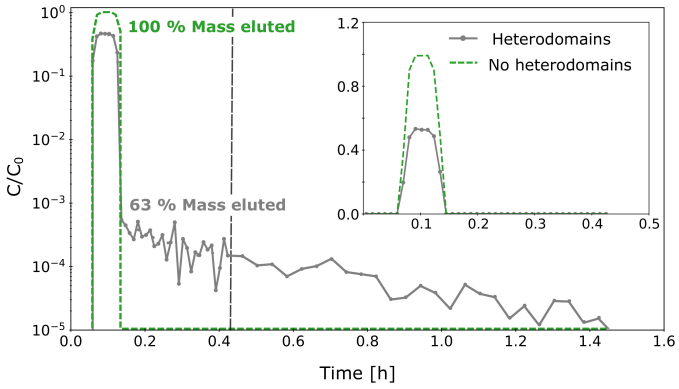

Figure 5-5: Simulated breakthrough curves. The grey solid and green dashed lines show simulations in the presence and absence of chemical heterodomains on the collector, respectively, in semi-log space. The vertical line marks the end of the experimental transport tests from which the particle pore-site distribution and deposition profiles were extracted. The insert shows the same data on linear-linear space. From these data it is evident that heterodomains display overall greater retention and a exponential heavy tailing due to broadened residence times from heterodomain interactions.

5.4 Concluding Remarks

The findings here presented underline the importance of explicitly taking into account surface heterogeneity to accurately model anomalous colloid transport under unfavorable conditions, where the effect of heterogeneity cascades onto all relevant scales for filtration. At the interface scale, individual interactions of colloids with solid-water interfaces in the presence of surface heterogeneity were modeled as a stochastic process that honors their true variability (ranging from very repulsive to very attractive). We demonstrate that representing the system by their mean-field interactions (i.e., a chemically homogeneous surface) is inadequate, as it averages out low probability but significant locally attractive interactions under bulk unfavorable conditions. At the pore scale, simulated Lagrangian trajectories of colloids moving through a Happel-sphere collector with surface heterogeneity resulted in a majority of particles irreversibly attaching along its surface, as well as a smaller fraction of particles retained without attachment at the near surface. The latter ultimately drags particles

to hydrodynamically stagnant regions at the rear of the collector where residence time is extended. The proportion of particles affected by each mechanism is in quantitative agreement with experimental observations for porous media with structure with regard to the percentage of retained particles found at the solid-water interface (attached) and at grain-to-grain contacts (near surface). At the Darcy scale, the diverse attachment efficiencies and broad residence times (even in an uniform flow field) were manifested in anomalous transport behavior, namely non-exponential deposition profiles and heavy tailed breakthrough curves. This anomalous behavior is in qualitative agreement with experimental data. Of particular notice is the good congruence between the mechanisms responsible for immobilizing simulated particles at each depth and the depth-dependent pore-scale locations where retained particles were found in experiments. Modeled breakthrough curves show a high sensitivity to the explicit consideration of surface heterogeneity, which brings about a heavy tail from near surface re-entrainment. In closing, improving the accuracy of predictions for colloid fate and transport in realistic porous media require careful characterization and consideration of surface heterogeneities (chemical and physical) across all relevant scales.

Supporting information

S5-1. xDLVO Parameters & Colloid SEM

The net interaction energy profiles were obtained using equations S1 to S5-4 and the parameters indicated in Table S5-1.

$$V_{VDW} = -\frac{A}{6D}\left(\frac{r_p r_c}{r_p + r_c}\right)\left[1 - \frac{5.32D}{\lambda}\ln\left(1 + \frac{\lambda}{5.32D}\right)\right] \tag{S5-1}$$

$$V_{EDL} = 64\pi\epsilon\left(\frac{r_p r_c}{r_p + r_c}\right)\left(\frac{\kappa_B T}{\nu e}\right)^2 \tanh\left(\frac{\nu e\zeta_1}{4\kappa_B T}\right)\tanh\left(\frac{\nu e\zeta_2}{4\kappa_B T}\right)e^{-\kappa D} \tag{S5-2}$$

$$V_{ST} = \pi a_{ST}^2 \gamma_0^{ST} \exp\left(-\frac{D}{\lambda_{ST}}\right) \tag{S5-3}$$

$$V_{AB} = 2\pi r_c \lambda_{AB}\gamma_0^{AB}\left[1 - \frac{\lambda_{AB}}{r_p} + \left(1 + \frac{\lambda_{AB}}{r_p}\right)e^{-\frac{2r_c}{\lambda_{AB}}}\right]\exp\left(-\frac{D}{\lambda_{AB}}\right) \tag{S5-4}$$

Where A is the combined Hamaker constant for the system, D is the separation distance, $r_p = 7\mu m$ and $r_c =$ are the radii of particle and collector, respectively. λ, λ_{ST}, and λ_{AB} are the decay length for van der Waals, steric and Lewis acid-base interactions, respectively. ϵ is the dielectric constant of the water, κ_B is the Boltzmann constant, T is temperature, ν is the valence of the symmetric electrolyte, e the charge of an electron, ζ_1 and ζ_2 are the zeta potential of the two interacting materials. κ is the inverse Debye length, a_{ST} is the radius of steric hydration contact.

S5-2. Attachment Efficiencies

Table S5-1: Parameters used for xDLVO calculations.

Description	Symbol	Value	Units
Hamaker constant	A	4.85×10^{-20}	J
Van der Waals decay length	λ	1.00×10^{-7}	m
Steric decay length	λ_{ST}	4.10×10^{-10}	m
Lewis acid-base decay length	λ_{AB}	6.00×10^{-10}	m
Dielectric constant of water	ϵ	80	-
Temperature	T	298	K
Valence of symmetric electrolyte	z	1	-
Zeta-potential of colloids	ζ_1	-50.00	mV
Zeta-potential of collector	ζ_2	-65.00	mV
Debye length	κ^{-1}	5.60×10^{-9}	m
Radius of steric hydration contact	a_{ST}	3.37×10^{-8}	m

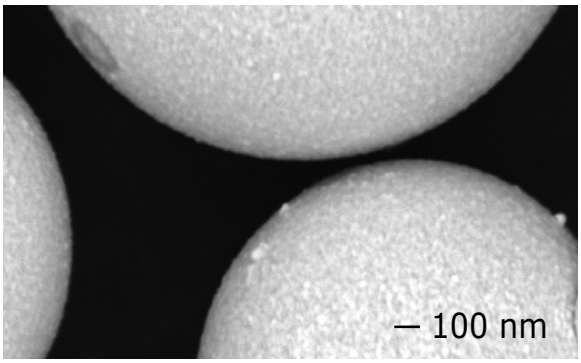

Figure S5-1: SEM image showing imperfections on the surface of the silver microspheres

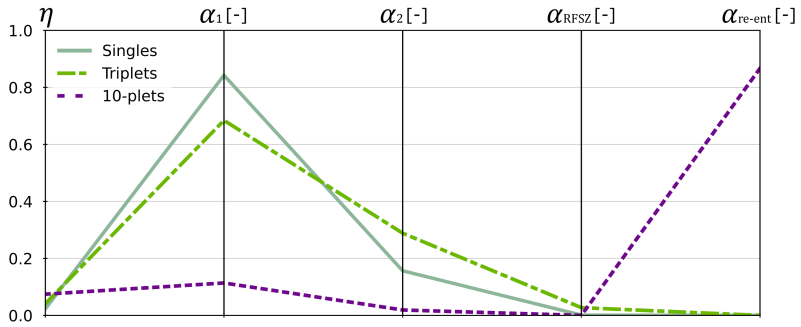

Figure S5-2: Mechanistically Simulated Near-Surface Efficiencies

S5-3. Mechanistically Simulated Near-Surface Efficiencies & Continuum-Scale Rate Constants.

Mechanistic simulations in the presence of CCHDs showed that upon approaching a collector, particles may fail to interact and exit the representative elementary volume, attach to it, or become associated at the near surface without contact as illustrated on Figure 5-1b. Lagrangian trajectories yielded the attachment efficiencies reported in Figure S5-2 for each polydisperse size fraction. The resulting α fractions exhibit size-specific trends. The collector efficiency η increased with particle size. That is, the bigger the particle, the more likely it is to enter the near surface fluid domain. Nonetheless, singlet particles showed the highest proportion of fast-attaching events (highest α_1), followed by triplets and then tenplates. This suggests that small particles are the most efficient in finding CCHDs so as to achieve attractive interactions. Conversely, only a small fraction of the tenplates sample are able to quickly find CCHDs to achieve fast attachment. The highest counts for slow-attachment (highest α_2) and for particles at the rear flow stagnation regions of the Happel-sphere (highest α_{RFSZ}) were found for the medium size particles while big particles yielded the highest fraction of particles that sample the near surface but go back onto the bulk fluid (highest α_{re-ent}).

Table S5-2: Mechanistically Simulated Near-Surface Efficiencies & Continuum-Scale Rate Constants.

Description	Units	Singlets	Triplets	Tenplates
r_p	[m]	7.0×10^{-6}	1.0×10^{-5}	1.5×10^{-5}
η	[-]	0.023	0.041	0.075
α_1	[-]	0.843	0.684	0.114
α_2	[-]	0.157	0.289	0.019
α_{RFSZ}	[-]	0.001	0.027	0.000
$\alpha_{re\text{-}ent}$	[-]	0.000	0.000	0.867
k_f	[1/hr]	11.617	21.135	39.228
k_{ns}	[1/hr]	0.403	1.343	0.161
k^*_{f2}	[1/hr]	2.275	4.551	0.257

S5-4. Mass balance for chemically homogeneous collector

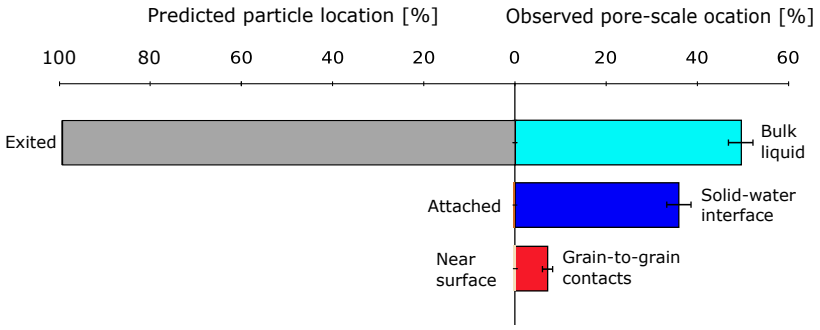

Figure S5-3: Particle location predicted from torque and force balance simulations when collector is chemically homogeneous vs. particle distribution over pore-scale locations obtained from XRCT.

Table S5-3: Parameters used to generate particle trajectories.

Description	Units	Value
Number of particles	[-]	5000
Darcy velocity	[m/s]	1.07×10^{-4}
Injection radius[a]	[m]	1.20×10^{-4}
Particle radius[a]	[m]	7.00×10^{-6}
Collector radius	[m]	5.00×10^{-4}
Happel porosity	[-]	0.53
Particle density[b]	[kg/m^3]	1.03×10^{3}
CCHD ζ-potential	[mV]	65.00
CCHD radius	[m]	5.00×10^{-7}
CCHD coverage	[%]	2.00
Slip length	[m]	1.00×10^{-8}
Asperity height	[m]	5.00×10^{-8}
Acid-base energy per area	[J/m^2]	-2.70×10^{-2}
Steric energy per area	[J/m^2]	1.70×10^{-3}
Combined elastic modulus	[N/m^2]	5.28×10^{10}
Work of adhesion	[J/m^2]	-2.20×10^{-3}

[a] For colloid radius 1.00×10^{-5}, injection radius was set to 1.5×10^{-4} m. For colloid radius 1.50×10^{-5}, injection radius was set to 1.9×10^{-4}.
[b] Trajectories were also generated for particle density of 1.00×10^{3}.

Table S5-4: Experimental conditions (parameters also used for upscaling) and mass recovery for transport tests.

Description	Units	Value±STD
Column length	[m]	0.03±0.001
Column diameter	[mm]	5.00±0.00
Injection time	[s]	222 ± 3
Concentration[a]	[# part./m^3]	9.59×10^{12}± 0.00
Tot. Simulation time	[s]	1542 ± 30
Mass at the solid-water interface	[%]	35.80 ± 2.66
Mass at grain-to-grain contacts	[%]	6.95 ± 1.12
Mass at bulk liquid	[%]	49.34 ± 2.69
Eluted mass	[%]	7.91 ± 1.09

[a] For colloid radius 1.00×10^{-5}, concentration was 1.27×10^{12}. For colloid radius 1.50×10^{-5}, concentration was 7.72×10^{10}. The particle concentrations were set up in order to have 68% of the total mass coming from singlets, 27% from triplets, and 5% from tenplets based on the aggregate size distribution from Perez et al., (2020) [209].

S5-5. Experimental conditions and mass recovery for transport tests

Conclusions, Implications and Perspectives

Anthropogenic colloid particle contaminants are released to natural environments by inadvertent pathways that lead to their growing accumulation in soil, sediment, freshwater, groundwater, and marine ecosystems. The research herein conducted provides insight to advance current model predictions for colloid transport in the subsurface and porous media environments at large. Classic theories and engineering tools often fail to predict the magnitude of groundwater contamination, frequently underestimating the true extent of areas at risk of colloid pollution. Results of this work can be used to reduce exposure risk to hazardous colloids in agricultural crops and drinking water wells. Also, soil-groundwater remediation techniques based on colloids as the active ingredient can benefit from the gained knowledge on the governing processes that control colloid retention at multiple spatial scales for better results on their practical implementation.

The following list summarize the main findings of the four projects that makeup this dissertation.

1. Dissolved organic matter (DOM) is ubiquitous in solution compositions relevant to agricultural soils. Such organic macromolecules readily adsorb onto silver and mica substrates, which significantly influence the deposition of silver colloids onto mineral soil grains.

2. Sorbed DOM alters the energy of interaction between the two charged sub-

strates in three key ways: i) by increasing the electrical double layer forces; ii) by creating a physical barrier between particles and collectors; and, iii) by triggering additional osmotic interactions due to compression of the DOM adsorbed layers.

3. Calcium ions overall promote DOM sorption but their effect on the adsorbed layer properties (e.g., thickness and compressibility) is substrate-dependent.

4. Silver colloids exhibit depth invariant trends for particle retention over the pore sites available within granular media, irrespective of the saturation, velocity and solution chemistry variability.

5. The solid-water interface is the pore-scale location that contributes the most to colloid retention, but it only accounts for half of deposited mass. Significant retention can take place in flow-stagnant regions corresponding to grain-to-grain contacts and the air-water-solid triple point for saturated and unsaturated systems, respectively.

6. Significant retention of colloids in flow stagnation zones, which are subject to reentrainment by diffusive means, is likely a key driver of ubiquitous heavy tails in breakthrough curves.

7. For colloidal suspensions, a broad distribution of aggregate sizes and compaction will affect the transport (single collector) coefficient, but not its attachment coefficient. This implies that colloids undergoing aggregation during transport in porous media move toward collectors driven by varying relative contribution of classic transport mechanisms (diffusion, interception, sedimentation) depending on size.

8. Formation of very large deposits of low fractal dimension is most likely near the column inlet under steady state conditions. At greater penetration depths

and higher shear, aggregates breakup and undergo structural evolution. Thus, sporadic release and redistribution of particles during physical or chemical disturbance is likely to disproportionately affect the small number of very large and frail aggregates near the inlet.

9. Surface heterogeneity is critical for modeling anomalous colloid transport in porous media under unfavorable conditions, where its effect cascades on all relevant scales for filtration.

10. In the presence of surface heterogeneity, individual colloid-collector interactions are stochastic, ranging from very repulsive to very attractive and cannot be properly described by profiles of average interactions.

11. We propose a link between pore-scale mechanisms and retention-site for retained particles that is in close agreement between simulations and experimental observations, respectively. That is, the proportion of particles that are affected by attachment is commensurate to the fraction of particles observed to deposit at the solid-water interface, while the proportion of particles retained without attachment at the near surface is commensurate to the fraction of particles observed to accumulate at grain-o-grain contacts.

12. Anomalous transport (non-exponential deposition profiles and heavy tailed breakthrough curves) may be explained by broadened residence times of colloids at the near surface resulting from surface interactions over heterogeneous surfaces, which can take place even in an uniform flow field.

These results have consequential implications for the prediction and control of particle transport and fate in soils. We find that agricultural soils are particularly vulnerable to enhanced spreading of inadvertently released colloidal particles, given that DOM-rich systems promote suspension stabilization. We infer that colloid transport in unsaturated soils (the vadose zone) may be hindered because the pore structure

promotes colloid retention at the air-water-solid tripe point and grain-to-grain contacts, which are abundant. We discern that surface heterogeneity promotes a variety of retention mechanisms and retention sites that vastly differ in macroscopic transport trends compared to equivalent chemically homogeneous systems, which may grossly impair remediation strategies that rely on uniformly distributing reactive particles throughout the contaminated porous medium.

Remaining questions that can be addressed with future work are summarized as follows. At the nanoscale, a more precise characterization of physical and chemical heterogeneities and coating layers on charged surfaces can facilitate the determination of possible colloid-substrate interactions under complex solution chemistries and improve prediction accuracy for upscaling models that rely on this information. At the pore-scale, extending the investigation to include real porous media or less ideal conditions would solidify the representativeness of the findings for real environmental systems. At the Darcy-scale, considering the effects that complex pore structures in real porous media (characterized by pores of variable size and connectivity) have on flow channelization and colloid filtration is another aspect that merits attention. Recent advances on the quality and resolution of three dimensional printed prototypes offers a promising tool to overcome experimental issues of reproducibility and repeatability that arise from using undisturbed soil cores. Detailed information of the characteristics of deposited aggregates along with their spatial location could be used to better understand the processes that lead to colloid remobilization during physical or chemical disturbances. A systematic assessment that couples transient transport experiments (at variable changes for ionic strength and pore velocity) with high resolution XRCT non-destructive imaging could be a first step towards understanding when and where particle deposits form and which ones become unstable.

Bibliography

[1] W. Stumm, "Chemical interaction in particle separation," *Environmental Science & Technology*, vol. 11, no. 12, pp. 1066–1070, 1977.

[2] J. R. Lead and K. J. Wilkinson, "Aquatic colloids and nanoparticles: current knowledge and future trends," *Environmental Chemistry*, vol. 3, no. 3, pp. 159–171, 2006.

[3] J. McCarthy and J. Zachara, "Es&t features: Subsurface transport of contaminants," *Environmental Science & Technology*, vol. 23, no. 5, pp. 496–502, 1989.

[4] S. A. Bradford and S. Torkzaban, "Colloid transport and retention in unsaturated porous media: A review of interface-, collector-, and pore-scale processes and models," *Vadose Zone Journal*, vol. 7, no. 2, pp. 667–681, 2008.

[5] R. N. Jordan, D. R. Yonge, and W. E. Hathhorn, "Enhanced mobility of pb in the presence of dissolved natural organic matter," *Journal of Contaminant Hydrology*, vol. 29, no. 1, pp. 59–80, 1997.

[6] M. B. McBride, B. K. Richards, T. Steenhuis, J. J. Russo, and S. Sauvé, "Mobility and solubility of toxic metals and nutrients in soil fifteen years after sludge application," *Soil Science*, vol. 162, no. 7, pp. 487–500, 1997.

[7] V. Guiné, J. Martins, and J. Gaudet, "Facilitated transport of heavy metals by bacterial colloids in sand columns," in *Journal de Physique IV (Proceedings)*, vol. 107, pp. 593–596, EDP sciences, 2003.

[8] L. A. Sprague, J. S. Herman, G. M. Hornberger, and A. L. Mills, "Atrazine adsorption and colloid-facilitated transport through the unsaturated zone," *Journal of Environmental Quality*, vol. 29, no. 5, pp. 1632–1641, 2000.

[9] C. Williams, M. Agassi, J. Letey, W. Farmer, S. Nelson, and M. Ben-Hur, "Facilitated transport of napropamide by dissolved organic matter through soil columns," *Soil Science Society of America journal*, vol. 64, no. 2, pp. 590–594, 2000.

[10] M. Cruz-Guzmán, R. Celis, M. C. Hermosin, W. C. Koskinen, and J. Cornejo, "Adsorption of pesticides from water by functionalized organobentonites," *Journal of Agricultural and Food Chemistry*, vol. 53, no. 19, pp. 7502–7511, 2005.

[11] A. P. Novikov, S. N. Kalmykov, S. Utsunomiya, R. C. Ewing, F. Horreard, A. Merkulov, S. B. Clark, V. V. Tkachev, and B. F. Myasoedov, "Colloid transport of plutonium in the far-field of the mayak production association, russia," *Science*, vol. 314, no. 5799, pp. 638–641, 2006.

[12] G. Chen, M. Flury, J. B. Harsh, and P. C. Lichtner, "Colloid-facilitated transport of cesium in variably saturated hanford sediments," *Environmental Science & Technology*, vol. 39, no. 10, pp. 3435–3442, 2005.

[13] J. E. Amburgey, A. Amirtharajah, M. T. York, B. M. Brouckaert, N. C. Spivey, and M. J. Arrowood, "Comparison of conventional and biological filter performance for cryptosporidium and microsphere removal," *Journal-American Water Works Association*, vol. 97, no. 12, pp. 77–91, 2005.

[14] A. Forslund, B. Markussen, L. Toenner-Klank, T. B. Bech, O. S. Jacobsen, and A. Dalsgaard, "Leaching of cryptosporidium parvum oocysts, escherichia coli, and a salmonella enterica serovar typhimurium bacteriophage through intact soil cores following surface application and injection of slurry," *Applied Environmental Microbiology*, vol. 77, no. 22, pp. 8129–8138, 2011.

[15] I. Molnar, W. P. Johnson, J. I. Gerhard, C. S. Willson, and D. M. O'Carroll, "Predicting colloid transport through saturated porous media: A critical review," *Water Resources Research*, vol. 51, no. 9, pp. 6804–6845, 2015.

[16] M. R. Wiesner, G. V. Lowry, P. Alvarez, D. Dionysiou, and P. Biswas, "Assessing the risks of manufactured nanomaterials," 2006.

[17] D. Montalvo, R. Vanderschueren, A. Fritzsche, R. U. Meckenstock, and E. Smolders, "Efficient removal of arsenate from oxic contaminated water by colloidal humic acid-coated goethite: Batch and column experiments," *Journal of Cleaner Production*, vol. 189, pp. 510–518, 2018.

[18] A. Tiraferri, L. A. S. Hernandez, C. Bianco, T. Tosco, and R. Sethi, "Colloidal behavior of goethite nanoparticles modified with humic acid and implications for aquifer reclamation," *Journal of Nanoparticle Research*, vol. 19, no. 3, p. 107, 2017.

[19] C. Bianco, J. Patiño, T. Tosco, A. Tiraferri, and R. Sethi, "Controlled deposition of particles in porous media for effective aquifer nanoremediation," *Scientific Reports*, vol. 7, no. 1, pp. 1–10, 2017.

[20] S. K. Brar, M. Verma, R. Tyagi, and R. Surampalli, "Engineered nanoparticles in wastewater and wastewater sludge–evidence and impacts," *Waste Management*, vol. 30, no. 3, pp. 504–520, 2010.

[21] E. Nanosilver, "State of the science literature review: Everything nanosilver and more," *U.S. Environmental Protection Agency, Washington, DC, EPA/600/R-10/084*, 2010.

[22] C. Buzea, I. I. Pacheco, and K. Robbie, "Nanomaterials and nanoparticles: sources and toxicity," *Biointerphases*, vol. 2, no. 4, pp. MR17–MR71, 2007.

[23] A. A. Keller and A. Lazareva, "Predicted releases of engineered nanomaterials: from global to regional to local," *Environmental Science & Technology Letters*, vol. 1, no. 1, pp. 65–70, 2014.

[24] F. Gottschalk, T. Sun, and B. Nowack, "Environmental concentrations of engineered nanomaterials: review of modeling and analytical studies," *Environmental Pollution*, vol. 181, pp. 287–300, 2013.

[25] T. M. Benn and P. Westerhoff, "Nanoparticle silver released into water from commercially available sock fabrics," *Environmental Science & Technology*, vol. 42, no. 11, pp. 4133–4139, 2008.

[26] K. Balantrapu and D. V. Goia, "Silver nanoparticles for printable electronics and biological applications," *Journal of Materials Research*, vol. 24, no. 9, pp. 2828–2836, 2009.

[27] M. U. Rashid, M. K. H. Bhuiyan, and M. E. Quayum, "Synthesis of silver nano particles (ag-nps) and their uses for quantitative analysis of vitamin c tablets," *Dhaka University Journal of Pharmaceutical Sciences*, vol. 12, no. 1, pp. 29–33, 2013.

[28] H.-M. Kwon, H.-W. Yun, S.-C. Kang, I.-J. Kim, and S.-S. Go, "Antibacterial paint containing nano silver particles and coating method using the same," Dec. 29 2005. US Patent App. 11/140,876.

[29] A. A. Keller, W. Vosti, H. Wang, and A. Lazareva, "Release of engineered nanomaterials from personal care products throughout their life cycle," *Journal of Nanoparticle Research*, vol. 16, no. 7, p. 2489, 2014.

[30] L. Geranio, M. Heuberger, and B. Nowack, "The behavior of silver nanotextiles during washing," *Environmental Science & Technology*, vol. 43, no. 21, pp. 8113–8118, 2009.

[31] A. Geranmayeh Oromieh, "Evaluating solubility, aggregation and sorption of nanosilver particles and silver ions in soils," *Soil and Environment. Swedish University of Agricultural Sciences*, 2011.

[32] K. Mijnendonckx, N. Leys, J. Mahillon, S. Silver, and R. Van Houdt, "Antimicrobial silver: uses, toxicity and potential for resistance," *Biometals*, vol. 26, no. 4, pp. 609–621, 2013.

[33] C. Beer, R. Foldbjerg, Y. Hayashi, D. S. Sutherland, and H. Autrup, "Toxicity of silver nanoparticles—nanoparticle or silver ion?," *Toxicology Letters*, vol. 208, no. 3, pp. 286–292, 2012.

[34] Y. Tian, B. Gao, C. Silvera-Batista, and K. J. Ziegler, "Transport of engineered nanoparticles in saturated porous media," *Journal of Nanoparticle Research*, vol. 12, no. 7, pp. 2371–2380, 2010.

[35] Y. Liang, S. A. Bradford, J. Simunek, H. Vereecken, and E. Klumpp, "Sensitivity of the transport and retention of stabilized silver nanoparticles to physicochemical factors," *Water Research*, vol. 47, no. 7, pp. 2572–2582, 2013.

[36] M. Dentz, T. Le Borgne, A. Englert, and B. Bijeljic, "Mixing, spreading and reaction in heterogeneous media: A brief review," *Journal of Contaminant Hydrology*, vol. 120, pp. 1–17, 2011.

[37] M. Elimelech, X. Jia, J. Gregory, and R. Williams, "Particle deposition and aggregation: Measurement, modelling and simulation woburn," *Massachusetts Butterworth-Heinemann*, vol. 440, 1998.

[38] A. Perez, V. L. Morales, and J. Patino, "Morphology of colloidal aggregates in porous media: Consequences for transport, deposition and reentrainment," *AGUFM*, vol. 2019, pp. H12E–06, 2019.

[39] D. C. Mays, O. T. Cannon, A. W. Kanold, K. J. Harris, T. C. Lei, and B. Gilbert, "Static light scattering resolves colloid structure in index-matched porous media," *Journal of Colloid and Interface Science*, vol. 363, no. 1, pp. 418–424, 2011.

[40] J.-F. Gaillard, C. Chen, S. H. Stonedahl, B. L. Lau, D. T. Keane, and A. I. Packman, "Imaging of colloidal deposits in granular porous media by x-ray difference micro-tomography," *Geophysical Research Letters*, vol. 34, no. 18, 2007.

[41] B. A. Legg, M. Zhu, L. R. Comolli, B. Gilbert, and J. F. Banfield, "Impacts of ionic strength on three-dimensional nanoparticle aggregate structure and consequences for environmental transport and deposition," *Environmental Science & Technology*, vol. 48, no. 23, pp. 13703–13710, 2014.

[42] S. Sirivithayapakorn and A. Keller, "Transport of colloids in unsaturated porous media: A pore-scale observation of processes during the dissolution of air-water interface," *Water Resources Research*, vol. 39, no. 12, 2003.

[43] J. Wan and T. K. Tokunaga, "Comments on "pore-scale visualization of colloid transport and retention in partly saturated porous media"," *Vadose Zone Journal*, vol. 4, no. 4, pp. 954–956, 2005.

[44] S. Xu, B. Gao, and J. E. Saiers, "Straining of colloidal particles in saturated porous media," *Water Resources Research*, vol. 42, no. 12, 2006.

[45] H. Vereecken, R. Kasteel, J. Vanderborght, and T. Harter, "Upscaling hydraulic properties and soil water flow processes in heterogeneous soils," *Vadose Zone Journal*, vol. 6, no. 1, pp. 1–28, 2007.

[46] K.-M. Yao, M. T. Habibian, and C. R. O'Melia, "Water and waste water filtration. concepts and applications," *Environmental Science & Technology*, vol. 5, no. 11, pp. 1105–1112, 1971.

[47] L. M. McDowell-Boyer, J. R. Hunt, and N. Sitar, "Particle transport through porous media," *Water Resources Research*, vol. 22, no. 13, pp. 1901–1921, 1986.

[48] N. Tufenkji and M. Elimelech, "Correlation equation for predicting single-collector efficiency in physicochemical filtration in saturated porous media," *Environmental Science & Technology*, vol. 38, no. 2, pp. 529–536, 2004.

[49] G. De Marsily, "Quantitative hydrogeology," tech. rep., Paris School of Mines, Fontainebleau, 1986.

[50] C. W. Fetter, T. B. Boving, and D. K. Kreamer, *Contaminant hydrogeology*, vol. 500. Prentice hall Upper Saddle River, NJ, 1999.

[51] R. Rajagopalan and C. Tien, "Trajectory analysis of deep-bed filtration with the sphere-in-cell porous media model," *AIChE Journal*, vol. 22, no. 3, pp. 523–533, 1976.

[52] B. E. Logan, D. Jewett, R. G. Arnold, E. Bouwer, and C. O'Melia, "Clarification of clean-bed filtration models," *Journal of Environmental Engineering*, vol. 121, no. 12, pp. 869–873, 1995.

[53] M. Elimelech and C. R. O'Melia, "Kinetics of deposition of colloidal particles in porous media," *Environmental Science & Technology*, vol. 24, no. 10, pp. 1528–1536, 1990.

[54] M. Elimelech, "Particle deposition on ideal collectors from dilute flowing suspensions: Mathematical formulation, numerical solution, and simulations," *Separations Technology*, vol. 4, no. 4, pp. 186–212, 1994.

[55] F. Messina, T. Tosco, and R. Sethi, "On the failure of upscaling the single-collector efficiency to the transport of colloids in an array of collectors," *Water Resources Research*, vol. 52, no. 7, pp. 5492–5505, 2016.

[56] B. V. Derjaguin, "Acta physicochim," *USSR*, vol. 14, 1941.

[57] E. Verwey and J. Willem, "Theory of the stability of lyophobic colloids.," *The Journal of Physical Chemistry*, vol. 51, no. 3, pp. 631–636, 1947.

[58] J. N. Israelachvili, *Intermolecular and surface forces*. Academic press, 2015.

[59] R. Bai and C. Tien, "Particle deposition under unfavorable surface interactions," *Journal of Colloid and Interface Science*, vol. 218, no. 2, pp. 488–499, 1999.

[60] M. W. Hahn, D. Abadzic, and C. R. O'Melia, "Aquasols: On the role of secondary minima," *Environmental Science & Technology*, vol. 38, no. 22, pp. 5915–5924, 2004.

[61] C. Shen, B. Li, Y. Huang, and Y. Jin, "Kinetics of coupled primary-and secondary-minimum deposition of colloids under unfavorable chemical conditions," *Environmental Science & Technology*, vol. 41, no. 20, pp. 6976–6982, 2007.

[62] S. A. Bradford, S. Torkzaban, H. Kim, and J. Simunek, "Modeling colloid and microorganism transport and release with transients in solution ionic strength," *Water Resources Research*, vol. 48, no. 9, 2012.

[63] S. Salgin, U. Salgin, and S. Bahadir, "Zeta potentials and isoelectric points of biomolecules: the effects of ion types and ionic strengths," *International Journal of Electrochemical Science*, vol. 7, no. 12, pp. 12404–12414, 2012.

[64] H. Ohshima, "Theory of electrostatics and electrokinetics of soft particles," *Science and Technology of Advanced Materials*, vol. 10, no. 6, p. 063001, 2009.

[65] T. Phenrat, N. Saleh, K. Sirk, H.-J. Kim, R. D. Tilton, and G. V. Lowry, "Stabilization of aqueous nanoscale zerovalent iron dispersions by anionic polyelectrolytes: adsorbed anionic polyelectrolyte layer properties and their effect on aggregation and sedimentation," *Journal of Nanoparticle Research*, vol. 10, no. 5, pp. 795–814, 2008.

[66] K. Birdi and S, "Surface and colloid chemistry," in *Handbook of surface and colloid chemistry*, pp. 10–52, CRC press, 2008.

[67] H. Ohshima, M. Nakamura, and T. Kondo, "Electrophoretic mobility of colloidal particles coated with a layer of adsorbed polymers," *Colloid and Polymer Science*, vol. 270, no. 9, pp. 873–877, 1992.

[68] W. Zhang, U.-s. Rattanaudompol, H. Li, and D. Bouchard, "Effects of humic and fulvic acids on aggregation of aqu/nc60 nanoparticles," *Water Research*, vol. 47, no. 5, pp. 1793–1802, 2013.

[69] V. L. Morales, W. Sang, D. R. Fuka, L. W. Lion, B. Gao, and T. S. Steenhuis, "Correlation equation for predicting attachment efficiency (α) of organic matter-colloid complexes in unsaturated porous media," *Environmental Science & Technology*, vol. 45, no. 23, pp. 10096–10101, 2011.

[70] M. M. Bob and H. W. Walker, "Effect of natural organic coatings on the polymer-induced coagulation of colloidal particles," *Colloids and surfaces A: Physicochemical and Engineering Aspects*, vol. 177, no. 2-3, pp. 215–222, 2001.

[71] S. Staunton, C. Dumat, and A. Zsolnay, "Possible role of organic matter in radiocaesium adsorption in soils," *Journal of Environmental Radioactivity*, vol. 58, no. 2-3, pp. 163–173, 2002.

[72] Y. Refaey, B. Jansen, A.-H. El-Shater, A.-A. El-Haddad, and K. Kalbitz, "The role of dissolved organic matter in adsorbing heavy metals in clay-rich soils," *Vadose Zone Journal*, vol. 13, no. 7, 2014.

[73] R. Abudalo, J. Ryan, R. W. Harvey, D. W. Metge, and L. Landkamer, "Influence of organic matter on the transport of cryptosporidium parvum oocysts in a ferric oxyhydroxide-coated quartz sand saturated porous medium," *Water Research*, vol. 44, no. 4, pp. 1104–1113, 2010.

[74] A. Franchi and C. R. O'Melia, "Effects of natural organic matter and solution chemistry on the deposition and reentrainment of colloids in porous media," *Environmental Science & Technology*, vol. 37, no. 6, pp. 1122–1129, 2003.

[75] X. Jiang, M. Tong, and H. Kim, "Influence of natural organic matter on the transport and deposition of zinc oxide nanoparticles in saturated porous media," *Journal of Colloid and Interface Science*, vol. 386, no. 1, pp. 34–43, 2012.

[76] V. L. Morales, W. Zhang, B. Gao, L. W. Lion, J. J. Bisogni Jr, B. A. McDonough, and T. S. Steenhuis, "Impact of dissolved organic matter on colloid transport in the vadose zone: Deterministic approximation of transport deposition coefficients from polymeric coating characteristics," *Water Research*, vol. 45, no. 4, pp. 1691–1701, 2011.

[77] A. J. Pelley and N. Tufenkji, "Effect of particle size and natural organic matter on the migration of nano-and microscale latex particles in saturated porous media," *Journal of Colloid and Interface Science*, vol. 321, no. 1, pp. 74–83, 2008.

[78] K. Kalbitz, D. Schwesig, J. Schmerwitz, K. Kaiser, L. Haumaier, B. Glaser, R. Ellerbrock, and P. Leinweber, "Changes in properties of soil-derived dissolved organic matter induced by biodegradation," *Soil Biology and Biochemistry*, vol. 35, no. 8, pp. 1129–1142, 2003.

[79] J. Gao, C. Liang, G. Shen, J. Lv, and H. Wu, "Spectral characteristics of dissolved organic matter in various agricultural soils throughout china," *Chemosphere*, vol. 176, pp. 108–116, 2017.

[80] K. Hunter and P. Liss, "The surface charge of suspended particles in estuarine and coastal waters," *Nature*, vol. 282, no. 5741, pp. 823–825, 1979.

[81] X. Li, T. D. Scheibe, and W. P. Johnson, "Apparent decreases in colloid deposition rate coefficients with distance of transport under unfavorable deposition conditions: A general phenomenon," *Environmental Science & Technology*, vol. 38, no. 21, pp. 5616–5625, 2004.

[82] W. P. Johnson, E. Pazmino, and H. Ma, "Direct observations of colloid retention in granular media in the presence of energy barriers, and implications for inferred mechanisms from indirect observations," *Water Research*, vol. 44, no. 4, pp. 1158–1169, 2010.

[83] A. J. Worthen, V. Tran, K. A. Cornell, T. M. Truskett, and K. P. Johnston, "Steric stabilization of nanoparticles with grafted low molecular weight ligands

in highly concentrated brines including divalent ions," *Soft Matter*, vol. 12, no. 7, pp. 2025–2039, 2016.

[84] N. Tufenkji and M. Elimelech, "Deviation from the classical colloid filtration theory in the presence of repulsive dlvo interactions," *Langmuir*, vol. 20, no. 25, pp. 10818–10828, 2004.

[85] S. A. Bradford, S. R. Yates, M. Bettahar, and J. Simunek, "Physical factors affecting the transport and fate of colloids in saturated porous media," *Water Resources Research*, vol. 38, no. 12, pp. 63–1, 2002.

[86] J. Simunek and M. T. van Genuchten, "Modeling nonequilibrium flow and transport processes using hydrus," *Vadose Zone Journal*, vol. 7, no. 2, pp. 782–797, 2008.

[87] Y. Zevi, A. Dathe, B. Gao, W. Zhang, B. K. Richards, and T. S. Steenhuis, "Transport and retention of colloidal particles in partially saturated porous media: Effect of ionic strength," *Water Resources Research*, vol. 45, no. 12, 2009.

[88] V. L. Morales, B. Gao, and T. S. Steenhuis, "Grain surface-roughness effects on colloidal retention in the vadose zone," *Vadose Zone Journal*, vol. 8, no. 1, pp. 11–20, 2009.

[89] J. T. Crist, J. F. McCarthy, Y. Zevi, P. Baveye, J. A. Throop, and T. S. Steenhuis, "Pore-scale visualization of colloid transport and retention in partly saturated porous media," *Vadose Zone Journal*, vol. 3, no. 2, pp. 444–450, 2004.

[90] A. A. Keller and M. Auset, "A review of visualization techniques of biocolloid transport processes at the pore scale under saturated and unsaturated conditions," *Advances in Water Resources*, vol. 30, no. 6-7, pp. 1392–1407, 2007.

[91] S. Bradford and M. Bettahar, "Straining, attachment, and detachment of cryptosporidium oocysts in saturated porous media," *Journal of Environmental Quality*, vol. 34, no. 2, pp. 469–478, 2005.

[92] C. Shen, Y. Huang, B. Li, and Y. Jin, "Effects of solution chemistry on straining of colloids in porous media under unfavorable conditions," *Water Resources Research*, vol. 44, no. 5, 2008.

[93] W. Johnson, X. Li, and G. Yal, "Colloid retention in porous media: Mechanistic confirmation of wedging and retention in zones of flow stagnation," *Environmental Science & Technology*, vol. 41, no. 4, pp. 1279–1287, 2007.

[94] H. Ma and W. P. Johnson, "Colloid retention in porous media of various porosities: Predictions by the hemispheres-in-cell model," *Langmuir*, vol. 26, no. 3, pp. 1680–1687, 2010.

[95] J. Wan and T. K. Tokunaga, "Film straining of colloids in unsaturated porous media: Conceptual model and experimental testing," *Environmental Science & Technology*, vol. 31, no. 8, pp. 2413–2420, 1997.

[96] Y. Jin, Y. Chu, and Y. Li, "Virus removal and transport in saturated and unsaturated sand columns," *Journal of Contaminant Hydrology*, vol. 43, no. 2, pp. 111–128, 2000.

[97] W. Zhang, V. L. Morales, M. E. Cakmak, A. E. Salvucci, L. D. Geohring, A. G. Hay, J.-Y. Parlange, and T. S. Steenhuis, "Colloid transport and retention in unsaturated porous media: Effect of colloid input concentration," *Environmental Science & Technology*, vol. 44, no. 13, pp. 4965–4972, 2010.

[98] B. Gao, T. S. Steenhuis, Y. Zevi, V. L. Morales, J. L. Nieber, B. K. Richards, J. F. McCarthy, and J.-Y. Parlange, "Capillary retention of colloids in unsaturated porous media," *Water Resources Research*, vol. 44, no. 4, 2008.

[99] M. Flury and S. Aramrak, "Role of air-water interfaces in colloid transport in porous media: A review," *Water Resources Research*, vol. 53, no. 7, pp. 5247–5275, 2017.

[100] J. J. Lenhart and J. E. Saiers, "Transport of silica colloids through unsaturated porous media: Experimental results and model comparisons," *Environmental Science & Technology*, vol. 36, no. 4, pp. 769–777, 2002.

[101] I. Molnar, J. I. Gerhard, C. S. Willson, and D. M. O'Carroll, "The impact of immobile zones on the transport and retention of nanoparticles in porous media," *Water Resources Research*, vol. 51, no. 11, pp. 8973–8994, 2015.

[102] C. Chen, B. Gaillard, and A. Packman, "Temporal evolution of pore geometry, fluid flow, and solute transport resulting from colloid deposition.," *Water Resources Research*, vol. 45, no. 6, p. W06416, 2009.

[103] E. Roth, B. Gilbert, and D. Mays, "Colloid deposit morphology and clogging in porous media: Fundamental insights through investigation of deposit fractal dimension.," *Environmental Science & Technology*, vol. 49, no. 20, pp. 12263–12270, 2015.

[104] S. A. Bradford, Y. F. Tadassa, and Y. Pachepsky, "Transport of giardia and manure suspensions in saturated porous media," *Journal of Environmental Quality*, vol. 35, no. 3, pp. 749–757, 2006.

[105] T. Tosco, M. P. Papini, C. C. Viggi, and R. Sethi, "Nanoscale zerovalent iron particles for groundwater remediation: a review," *Journal of Cleaner Production*, vol. 77, pp. 10–21, 2014.

[106] Z. Adamczyk, B. Siwek, M. Zembala, and P. Belouschek, "Kinetics of localized adsorption of colloid particles," *Advances in Colloid and Interface Science*, vol. 48, pp. 151–280, 1994.

[107] C.-H. Ko and M. Elimelech, "The "shadow effect" in colloid transport and deposition dynamics in granular porous media: measurements and mechanisms," *Environmental Science & Technology*, vol. 34, no. 17, pp. 3681–3689, 2000.

[108] X. Li, C.-L. Lin, J. D. Miller, and W. P. Johnson, "Pore-scale observation of microsphere deposition at grain-to-grain contacts over assemblage-scale porous media domains using x-ray microtomography," *Environmental Science & Technology*, vol. 40, no. 12, pp. 3762–3768, 2006.

[109] X. Li, C.-L. Lin, J. D. Miller, and W. P. Johnson, "Role of grain-to-grain contacts on profiles of retained colloids in porous media in the presence of an energy barrier to deposition," *Environmental Science & Technology*, vol. 40, no. 12, pp. 3769–3774, 2006.

[110] G. Malgaresi, B. Collins, P. Alvaro, and P. Bedrikovetsky, "Explaining non-monotonic retention profiles during flow of size-distributed colloids," *Chemical Engineering Journal*, vol. 375, p. 121984, 2019.

[111] W. P. Johnson, A. Rasmuson, E. Pazmiño, and M. Hilpert, "Why variant colloid transport behaviors emerge among identical individuals in porous media when colloid–surface repulsion exists," *Environmental Science & Technology*, vol. 52, no. 13, pp. 7230–7239, 2018.

[112] E. Pazmino, J. Trauscht, B. Dame, and W. P. Johnson, "Power law size-distributed heterogeneity explains colloid retention on soda lime glass in the presence of energy barriers," *Langmuir*, vol. 30, no. 19, pp. 5412–5421, 2014.

[113] C. A. Ron, K. VanNess, A. Rasmuson, and W. P. Johnson, "How nanoscale surface heterogeneity impacts transport of nano-to micro-particles on surfaces under unfavorable attachment conditions," *Environmental Science: Nano*, vol. 6, no. 6, pp. 1921–1931, 2019.

[114] C. A. Ron and W. P. Johnson, "Complementary colloid and collector nanoscale heterogeneity explains microparticle retention under unfavorable conditions," *Environmental Science: Nano*, vol. 7, no. 12, pp. 4010–4021, 2020.

[115] W. P. Johnson, "Quantitative linking of nanoscale interactions to continuum-scale nanoparticle and microplastic transport in environmental granular media," *Environmental Science & Technology*, vol. 54, no. 13, pp. 8032–8042, 2020.

[116] W. P. Johnson and M. Hilpert, "Upscaling colloid transport and retention under unfavorable conditions: Linking mass transfer to pore and grain topology," *Water Resources Research*, vol. 49, no. 9, pp. 5328–5341, 2013.

[117] F. Gottschalk, T. Sonderer, R. W. Scholz, and B. Nowack, "Modeled environmental concentrations of engineered nanomaterials (tio2, zno, ag, cnt, fullerenes) for different regions," *Environmental Science & Technology*, vol. 43, no. 24, pp. 9216–9222, 2009.

[118] L. Goswami, K.-H. Kim, A. Deep, P. Das, S. S. Bhattacharya, S. Kumar, and A. A. Adelodun, "Engineered nano particles: nature, behavior, and effect on the environment," *Jounal of Environmental Management*, vol. 196, pp. 297–315, 2017.

[119] I. Sondi and B. Salopek-Sondi, "Silver nanoparticles as antimicrobial agent: a case study on e. coli as a model for gram-negative bacteria," *Journal of Colloid & Interface Science*, vol. 275, no. 1, pp. 177–182, 2004.

[120] J.-Y. Maillard and P. Hartemann, "Silver as an antimicrobial: facts and gaps in knowledge," *Critical Reviews in Microbiology*, vol. 39, no. 4, pp. 373–383, 2013.

[121] C. Zhang, Z. Hu, and B. Deng, "Silver nanoparticles in aquatic environments: Physiochemical behavior and antimicrobial mechanisms," *Water Research*, vol. 88, pp. 403–427, 2016.

[122] R. Kaegi, A. Voegelin, B. Sinnet, S. Zuleeg, H. Hagendorfer, M. Burkhardt, and H. Siegrist, "Behavior of metallic silver nanoparticles in a pilot wastewater treatment plant," *Environmental Science & Technology*, vol. 45, no. 9, pp. 3902–3908, 2011.

[123] T. Benn, B. Cavanagh, K. Hristovski, J. D. Posner, and P. Westerhoff, "The release of nanosilver from consumer products used in the home," *Journal of Environmental Quality*, vol. 39, no. 6, pp. 1875–1882, 2010.

[124] S. McGrath, A. Chang, A. Page, and E. Witter, "Land application of sewage sludge: scientific perspectives of heavy metal loading limits in europe and the united states," *Environmental Reviews*, vol. 2, no. 1, pp. 108–118, 1994.

[125] S. A. Blaser, M. Scheringer, M. MacLeod, and K. Hungerbühler, "Estimation of cumulative aquatic exposure and risk due to silver: contribution of nano-functionalized plastics and textiles," *Science of the Total Environment*, vol. 390, no. 2-3, pp. 396–409, 2008.

[126] P. Gajjar, B. Pettee, D. W. Britt, W. Huang, W. P. Johnson, and A. J. Anderson, "Antimicrobial activities of commercial nanoparticles against an environmental soil microbe, pseudomonas putida kt2440," *Journal of Biological Engineering*, vol. 3, no. 1, pp. 1–13, 2009.

[127] C. Dimkpa, A. Calder, P. Gajjar, S. Merugu, W. Huang, D. Britt, J. McLean, W. Johnson, and A. Anderson, "Interaction of silver nanoparticles with an environmentally beneficial bacterium, pseudomonas chlororaphis," *Journal of Hazardous Materials*, vol. 188, no. 1-3, pp. 428–435, 2011.

[128] A. J. Calder, C. O. Dimkpa, J. E. McLean, D. W. Britt, W. Johnson, and A. J. Anderson, "Soil components mitigate the antimicrobial effects of silver nanoparticles towards a beneficial soil bacterium, pseudomonas chlororaphis o6," *Science of the Total Environment*.

[129] E. J. W. Verwey, J. T. G. Overbeek, and K. Van Nes, *Theory of the stability of lyophobic colloids: the interaction of sol particles having an electric double layer*. Elsevier Publishing Company, 1948.

[130] D. Grasso, K. Subramaniam, M. Butkus, K. Strevett, and J. Bergendahl, "A review of non-dlvo interactions in environmental colloidal systems," *Reviews in Environmental Science & Biotechnology*, vol. 1, no. 1, pp. 17–38, 2002.

[131] A. D. Dwivedi, S. P. Dubey, M. Sillanpää, Y.-N. Kwon, C. Lee, and R. S. Varma, "Fate of engineered nanoparticles: implications in the environment," *Coordination Chemistry Reviews*, vol. 287, pp. 64–78, 2015.

[132] R. W. Harvey and S. P. Garabedian, "Use of colloid filtration theory in modeling movement of bacteria through a contaminated sandy aquifer," *Environmental Science & Technology*, vol. 25, no. 1, pp. 178–185, 1991.

[133] J. N. Ryan and M. Elimelech, "Colloid mobilization and transport in groundwater," *Colloids and surfaces A: Physicochemical and Engineering Aspects*, vol. 107, pp. 1–56, 1996.

[134] H. Ma, M. Hradisky, and W. P. Johnson, "Extending applicability of correlation equations to predict colloidal retention in porous media at low fluid velocity," *Environmental Science & Technology*, vol. 47, no. 5, pp. 2272–2278, 2013.

[135] M. Elimelech, "Predicting collision efficiencies of colloidal particles in porous media," *Water Research*, vol. 26, no. 1, pp. 1–8, 1992.

[136] R. Bai and C. Tien, "A new correlation for the initial filter coefficient under unfavorable surface interactions," *Journal of Colloid and Interface Science*, vol. 179, no. 2, pp. 631–634, 1996.

[137] T. Phenrat, J. E. Song, C. M. Cisneros, D. P. Schoenfelder, R. D. Tilton, and G. V. Lowry, "Estimating attachment of nano-and submicrometer-particles coated with organic macromolecules in porous media: development of an empirical model," *Environmental Science & Technology*, vol. 44, no. 12, pp. 4531–4538, 2010.

[138] G. R. Aiken, H. Hsu-Kim, and J. N. Ryan, "Influence of dissolved organic matter on the environmental fate of metals, nanoparticles, and colloids," *Environmental Science & Technology*, vol. 45, pp. 3196–3201, 2011.

[139] R. Grillo, A. H. Rosa, and L. F. Fraceto, "Engineered nanoparticles and organic matter: a review of the state-of-the-art," *Chemosphere*, vol. 119, pp. 608–619, 2015.

[140] S. M. Louie, R. D. Tilton, and G. V. Lowry, "Effects of molecular weight distribution and chemical properties of natural organic matter on gold nanoparticle aggregation," *Environmental Science & Technology*, vol. 47, no. 9, pp. 4245–4254, 2013.

[141] D. P. Stankus, S. E. Lohse, J. E. Hutchison, and J. A. Nason, "Interactions between natural organic matter and gold nanoparticles stabilized with different organic capping agents," *Environmental Science & Technology*, vol. 45, no. 8, pp. 3238–3244, 2011.

[142] Y. Zhang, Y. Chen, P. Westerhoff, and J. Crittenden, "Impact of natural organic matter and divalent cations on the stability of aqueous nanoparticles," *Water Research*, vol. 43, no. 17, pp. 4249–4257, 2009.

[143] K. L. Chen and M. Elimelech, "Influence of humic acid on the aggregation kinetics of fullerene (c60) nanoparticles in monovalent and divalent electrolyte solutions," *Journal of Colloid and Interface Science*, vol. 309, no. 1, pp. 126–134, 2007.

[144] N. B. Saleh, L. D. Pfefferle, and M. Elimelech, "Aggregation kinetics of multiwalled carbon nanotubes in aquatic systems: measurements and environmental implications," *Environmental Science & Technology*, vol. 42, no. 21, pp. 7963–7969, 2008.

[145] B. J. R. Thio, M. O. Montes, M. A. Mahmoud, D.-W. Lee, D. Zhou, and A. A. Keller, "Mobility of capped silver nanoparticles under environmentally relevant conditions," *Environmental Science & Technology*, vol. 46, no. 13, pp. 6985–6991, 2012.

[146] K. L. Chen and M. Elimelech, "Interaction of fullerene (c-60) nanoparticles with humic acid and alginate coated silica surfaces: Measurements, mechanisms, and environmental implications," *Environmental Science & Technology*, vol. 42, no. 20, pp. 7607–7614, 2008.

[147] Y. F. Adrian, U. Schneidewind, S. A. Bradford, J. Simunek, T. M. Fernandez-Steeger, and R. Azzam, "Transport and retention of surfactant-and polymer-stabilized engineered silver nanoparticles in silicate-dominated aquifer material," *Environmental Pollution*, vol. 236, pp. 195–207, 2018.

[148] M. Hoppe, R. Mikutta, J. Utermann, W. Duijnisveld, and G. Guggenberger, "Retention of sterically and electrosterically stabilized silver nanoparticles in soils," *Environmental Science & Technology*, vol. 48, no. 21, pp. 12628–12635, 2014.

[149] S. R. Kanel, J. Flory, A. Meyerhoefer, J. L. Fraley, I. E. Sizemore, and M. N. Goltz, "Influence of natural organic matter on fate and transport of silver nanoparticles in saturated porous media: laboratory experiments and modeling," *Journal of Nanoparticle Research*, vol. 17, no. 3, p. 154, 2015.

[150] Z. Li, K. Greden, P. J. Alvarez, K. B. Gregory, and G. V. Lowry, "Adsorbed polymer and nom limits adhesion and toxicity of nano scale zerovalent iron to e. coli," *Environmental Science & Technology*, vol. 44, no. 9, pp. 3462–3467, 2010.

[151] O. Furman, S. Usenko, and B. L. Lau, "Relative importance of the humic and fulvic fractions of natural organic matter in the aggregation and deposition of silver nanoparticles," *Environmental Science & Technology*, vol. 47, no. 3, pp. 1349–1356, 2013.

[152] S. Sander, L. M. Mosley, and K. A. Hunter, "Investigation of interparticle forces in natural waters: Effects of adsorbed humic acids on iron oxide and alumina surface properties," *Environmental Science & Technology*, vol. 38, no. 18, pp. 4791–4796, 2004.

[153] A. J. Fairhurst and P. Warwick, "The influence of humic acid on europium–mineral interactions," *Colloids and Surfaces A: Physicochemical and Engineering Aapects*, vol. 145, no. 1-3, pp. 229–234, 1998.

[154] S. Assemi, J. Nalaskowski, and W. P. Johnson, "Direct force measurements between carboxylate-modified latex microspheres and glass using atomic force microscopy," *Colloids and Surfaces A: Physicochemical and Engineering Aapects*, vol. 286, no. 1-3, pp. 70–77, 2006.

[155] T. Kuhl, D. E. Leckband, D. Lasic, and J. Israelachvili, "Modulation of interaction forces between bilayers exposing short-chained ethylene oxide headgroups," *Biophysical Journal*, vol. 66, no. 5, pp. 1479–1488, 1994.

[156] S. Boggs Jr, D. Livermore, and M. G. Seitz, "Humic substances in natural waters and their complexation with trace metals and radionuclides: a review.[129 references]," tech. rep., Argonne National Lab., IL (USA), 1985.

[157] J. Israelachvili, "Thin film studies using multiple-beam interferometry," *Journal of Colloid and Interface Science*, vol. 44, no. 2, pp. 259–272, 1973.

[158] J. Kurniawan, N.-N. Yin, G.-y. Liu, and T. L. Kuhl, "Interaction forces between ternary lipid bilayers containing cholesterol," *Langmuir*, vol. 30, no. 17, pp. 4997–5004, 2014.

[159] O. J. Rojas, "Adsorption of polyelectrolytes on mica," 2002.

[160] J. N. Israelachvili and G. E. Adams, "Measurement of forces between two mica surfaces in aqueous electrolyte solutions in the range 0–100 nm," *Journal of the Chemical Society, Faraday Transactions 1: Physical Chemistry in Condensed Phases*, vol. 74, pp. 975–1001, 1978.

[161] A. Grabbe, "Double layer interactions between silylated silica surfaces," *Langmuir*, vol. 9, no. 3, pp. 797–801, 1993.

[162] M. Elimelech, J. Gregory, and X. Jia, *Particle deposition and aggregation: measurement, modelling and simulation*. Butterworth-Heinemann, 2013.

[163] J. Levins and T. Vanderlick, "Characterization of the interface between a rough metal and smooth mica in contact," *Journal of Colloid and Interface Science*, vol. 185, no. 2, pp. 449–458, 1997.

[164] I. Lifshitz and A. Kosevich, "Theory of magnetic susceptibility in metals at low temperatures," *Journal of Experimental and Theoretical Physics*, vol. 2, no. 4, pp. 636–645, 1956.

[165] R. Hogg, T. W. Healy, and D. W. Fuerstenau, "Mutual coagulation of colloidal dispersions," *Transactions of the Faraday Society*, vol. 62, pp. 1638–1651, 1966.

[166] G. Wiese and T. W. Healy, "Effect of particle size on colloid stability," *Transactions of the Faraday Society*, vol. 66, pp. 490–499, 1970.

[167] G. Bell, S. Levine, and L. McCartney, "Approximate methods of determining the double-layer free energy of interaction between two charged colloidal spheres," *Journal of Colloid and Interface Science*, vol. 33, no. 3, pp. 335–359, 1970.

[168] S. Klitzke, G. Metreveli, A. Peters, G. E. Schaumann, and F. Lang, "The fate of silver nanoparticles in soil solution—sorption of solutes and aggregation," *Science of The Total Environment*, vol. 535, pp. 54–60, 2015.

[169] M. J. Haider and M. S. Mehdi, "Study of morphology and zeta potential analyzer for the silver nanoparticles," *International Journal of Scientific and Engineering Research*, vol. 5, no. 7, pp. 381–385, 2014.

[170] P. Maroni, F. J. Montes Ruiz-Cabello, C. Cardoso, and A. Tiraferri, "Adsorbed mass of polymers on self-assembled monolayers: Effect of surface chemistry and polymer charge," *Langmuir*, vol. 31, no. 22, pp. 6045–6054, 2015.

[171] M. Moazzami-Gudarzi, P. Maroni, M. Borkovec, and G. Trefalt, "Depletion and double layer forces acting between charged particles in solutions of like-charged polyelectrolytes and monovalent salts," *Soft Matter*, vol. 13, no. 18, pp. 3284–3295, 2017.

[172] P. C. Kearney, L. S. Mizoue, R. A. Kumpf, J. E. Forman, A. McCurdy, and D. A. Dougherty, "Molecular recognition in aqueous media. new binding studies provide further insights into the cation-. pi. interaction and related phenomena," *Journal of the American Chemical Society*, vol. 115, no. 22, pp. 9907–9919, 1993.

[173] D. A. Dougherty, "The cation- π interaction," *Accounts of Chemical Research*, vol. 46, no. 4, pp. 885–893, 2013.

[174] T. Kuhl, D. Leckband, D. Lasic, and J. Israelachvili, *Modulation and modeling of interaction forces between lipid bilayers exposing terminally grafted polymer chains*. CRC Press: Boca Raton, FL, 1995.

[175] S. M. Louie, T. Phenrat, M. J. Small, R. D. Tilton, and G. V. Lowry, "Parameter identifiability in application of soft particle electrokinetic theory to determine polymer and polyelectrolyte coating thicknesses on colloids," *Langmuir*, vol. 28, no. 28, pp. 10334–10347, 2012.

[176] S. Ren, E. Tombacz, and J. A. Rice, "Dynamic light scattering from power-law polydisperse fractals: Application of dynamic scaling to humic acid," *Physical Review E*, vol. 53, no. 3, p. 2980, 1996.

[177] Y.-P. Chin, G. Aiken, and E. O'Loughlin, "Molecular weight, polydispersity, and spectroscopic properties of aquatic humic substances," *Environmental Science & Technology*, vol. 28, no. 11, pp. 1853–1858, 1994.

[178] A. Tiraferri and P. Maroni, "Rapid desorption of polyelectrolytes from solid surfaces induced by changes of aqueous chemistry," *Langmuir*, vol. 34, no. 41, pp. 12302–12309, 2018.

[179] J. A. van Heiningen and R. J. Hill, "Poly (ethylene oxide) adsorption onto and desorption from silica microspheres: New insights from optical tweezers electrophoresis," *Macromolecules*, vol. 44, no. 20, pp. 8245–8260, 2011.

[180] P. Relan, K. Girdhar, and S. Khanna, "Molecular configuration of compost's humic acid by viscometric studies," *Plant Soil*, vol. 81, no. 2, pp. 203–208, 1984.

[181] W.-P. Liao, I. G. Elliott, R. Faller, and T. L. Kuhl, "Normal and shear interactions between high grafting density polymer brushes grown by atom transfer radical polymerization," *Soft Matter*, vol. 9, no. 24, pp. 5753–5761, 2013.

[182] H. J. Taunton, C. Toprakcioglu, L. J. Fetters, and J. Klein, "Interactions between surfaces bearing end-adsorbed chains in a good solvent," *Macromolecules*, vol. 23, no. 2, pp. 571–580, 1990.

[183] A. Tiraferri, P. Maroni, and M. Borkovec, "Adsorption of polyelectrolytes to like-charged substrates induced by multivalent counterions as exemplified by poly (styrene sulfonate) and silica," *Physical Chemistry Chemical Physics*, vol. 17, no. 16, pp. 10348–10352, 2015.

[184] B. Derjaguin, "Friction and adhesion. iv. the theory of adhesion of small particles," *Kolloid Zeits*, vol. 69, pp. 155–164, 1934.

[185] B. Vincent, J. Edwards, S. Emmett, and A. Jones, "Depletion flocculation in dispersions of sterically-stabilised particles ("soft spheres")," *Colloids Surfaces*, vol. 18, no. 2-4, pp. 261–281, 1986.

[186] K. A. Huynh and K. L. Chen, "Aggregation kinetics of citrate and polyvinylpyrrolidone coated silver nanoparticles in monovalent and divalent electrolyte solutions," *Environmental Science & Technology*, vol. 45, no. 13, pp. 5564–5571, 2011.

[187] S. Lin, Y. Cheng, Y. Bobcombe, K. L. Jones, J. Liu, and M. R. Wiesner, "Deposition of silver nanoparticles in geochemically heterogeneous porous media: predicting affinity from surface composition analysis," *Environmental Science & Technology*, vol. 45, no. 12, pp. 5209–5215, 2011.

[188] X. Yang, S. Lin, and M. R. Wiesner, "Influence of natural organic matter on transport and retention of polymer coated silver nanoparticles in porous media," *Journal of Hazardous Materials*, vol. 264, pp. 161–168, 2014.

[189] P. R. Johnson, N. Sun, and M. Elimelech, "Colloid transport in geochemically heterogeneous porous media: Modeling and measurements," *Environmental Science & Technology*, vol. 30, no. 11, pp. 3284–3293, 1996.

[190] M. Elimelech, M. Nagai, C.-H. Ko, and J. N. Ryan, "Relative insignificance of mineral grain zeta potential to colloid transport in geochemically heterogeneous porous media," *Environmental Science & Technology*, vol. 34, no. 11, pp. 2143–2148, 2000.

[191] A. R. Petosa, D. P. Jaisi, I. R. Quevedo, M. Elimelech, and N. Tufenkji, "Aggregation and deposition of engineered nanomaterials in aquatic environments: role of physicochemical interactions," *Environmental Science & Technology*, vol. 44, no. 17, pp. 6532–6549, 2010.

[192] K. A. Huynh, J. M. McCaffery, and K. L. Chen, "Heteroaggregation of multiwalled carbon nanotubes and hematite nanoparticles: rates and mechanisms," *Environmental Science & Technology*, vol. 46, no. 11, pp. 5912–5920, 2012.

[193] G. Cornelis, L. Pang, C. Doolette, J. K. Kirby, and M. J. McLaughlin, "Transport of silver nanoparticles in saturated columns of natural soils," *Science of The Total Environment*, vol. 463, pp. 120–130, 2013.

[194] F. Gottschalk, T. Sun, and B. Nowack, "Environmental concentrations of engineered nanomaterials: review of modeling and analytical studies," *Environmental Pollution*, vol. 181, pp. 287–300, 2013.

[195] J. Hedberg, M. Lundin, T. Lowe, E. Blomberg, S. Wold, and I. O. Wallinder, "Interactions between surfactants and silver nanoparticles of varying charge," *Journal of Colloid and Interface Science*, vol. 369, no. 1, pp. 193–201, 2012.

[196] A. M. El Badawy, R. G. Silva, B. Morris, K. G. Scheckel, M. T. Suidan, and T. M. Tolaymat, "Surface charge-dependent toxicity of silver nanoparticles," *Environmental Science & Technology*, vol. 45, no. 1, pp. 283–287, 2011.

[197] J. E. Patiño, T. L. Kuhl, and V. L. Morales, "Direct measurements of the forces between silver and mica in humic substance-rich solutions," *Environmental Science & Technology*, vol. 54, no. 23, pp. 15076–15085, 2020.

[198] A. Samarajeewa, J. Velicogna, J. Princz, R. Subasinghe, R. Scroggins, and L. Beaudette, "Effect of silver nano-particles on soil microbial growth, activity and community diversity in a sandy loam soil," *Environmental Pollution*, vol. 220, pp. 504–513, 2017.

[199] W. M. Sillen, S. Thijs, G. R. Abbamondi, J. Janssen, N. Weyens, J. C. White, and J. Vangronsveld, "Effects of silver nanoparticles on soil microorganisms and maize biomass are linked in the rhizosphere," *Soil Biology and Biochemistry*, vol. 91, pp. 14–22, 2015.

[200] H. Zhang, M. Huang, W. Zhang, J. L. Gardea-Torresdey, J. C. White, R. Ji, and L. Zhao, "Silver nanoparticles alter soil microbial community compositions and metabolite profiles in unplanted and cucumber-planted soils," *Environmental Science & Technology*, vol. 54, no. 6, pp. 3334–3342, 2020.

[201] N. Hadrup and H. R. Lam, "Oral toxicity of silver ions, silver nanoparticles and colloidal silver–a review," *Regulatory Toxicology and Pharmacology*, vol. 68, no. 1, pp. 1–7, 2014.

[202] E.-J. Park, E. Bae, J. Yi, Y. Kim, K. Choi, S. H. Lee, J. Yoon, B. C. Lee, and K. Park, "Repeated-dose toxicity and inflammatory responses in mice by oral administration of silver nanoparticles," *Environmental Toxicology and Pharmacology*, vol. 30, no. 2, pp. 162–168, 2010.

[203] E. D. Kuempel, J. R. Roberts, G. Roth, R. D. Zumwalde, D. Nathan, A. F. Hubbs, D. Trout, G. Holdsworth, *et al.*, "Current intelligence bulletin 70: Health effects of occupational exposure to silver nanomaterials," *U.S. Department of Health and Human Services, Centers for Disease Control and Prevention, National Institute for Occupational Safety and Health, DHHS (NIOSH)*, no. 2021-112, 2021.

[204] A. Rasmuson, E. Pazmino, S. Assemi, and W. P. Johnson, "Contribution of nano-to microscale roughness to heterogeneity: Closing the gap between unfavorable and favorable colloid attachment conditions," *Environmental Science & Technology*, vol. 51, no. 4, pp. 2151–2160, 2017.

[205] A. Cortis, T. Harter, L. Hou, E. R. Atwill, A. I. Packman, and P. G. Green, "Transport of cryptosporidium parvum in porous media: Long-term elution experiments and continuous time random walk filtration modeling," *Water Resources Research*, vol. 42, no. 12, 2006.

[206] E. Goldberg, M. Scheringer, T. D. Bucheli, and K. , Hungerbühler, "Critical assessment of models for transport of engineered nanoparticles in saturated porous media," *Environmental Science & Technology*, vol. 48, no. 21, pp. 12732–12741, 2014.

[207] N. Tufenkji and M. Elimelech, "Breakdown of colloid filtration theory: Role of the secondary energy minimum and surface charge heterogeneities," *Langmuir*, vol. 21, no. 3, pp. 841–852, 2005.

[208] F. Leuther, J. M. Köhne, G. Metreveli, and H.-J. Vogel, "Transport and retention of sulfidized silver nanoparticles in porous media: The role of air-water interfaces, flow velocity, and natural organic matter," *Water Resources Research*, vol. 56, no. 9, p. e2020WR027074, 2020.

[209] A. J. Perez, J. E. Patino, M. Soos, and V. L. Morales, "Morphology of shear-induced colloidal aggregates in porous media: Consequences for transport, deposition, and re-entrainment," *Environmental Science & Technology*, vol. 54, no. 9, pp. 5813–5821, 2020.

[210] S. Torkzaban, S. S. Tazehkand, S. L. Walker, and S. A. Bradford, "Transport and fate of bacteria in porous media: Coupled effects of chemical conditions and pore space geometry," *Water Resources Research*, vol. 44, no. 4, 2008.

[211] S. Torkzaban, S. A. Bradford, and S. L. Walker, "Resolving the coupled effects of hydrodynamics and dlvo forces on colloid attachment in porous media," *Langmuir*, vol. 23, no. 19, pp. 9652–9660, 2007.

[212] J. Bergendahl and D. Grasso, "Colloid generation during batch leaching tests: Mechanics of disaggregation," *Colloids and surfaces A: Physicochemical and Engineering Aspects*, vol. 135, no. 1-3, pp. 193–205, 1998.

[213] S. A. Bradford, S. Torkzaban, and S. L. Walker, "Coupling of physical and chemical mechanisms of colloid straining in saturated porous media," *Water Research*, vol. 41, no. 13, pp. 3012–3024, 2007.

[214] W. P. Johnson, X. Li, and G. Yal, "Colloid retention in porous media: Mechanistic confirmation of wedging and retention in zones of flow stagnation," *Environmental Science & Technology*, vol. 41, no. 4, pp. 1279–1287, 2007.

[215] D. Lin, L. Hu, S. A. Bradford, X. Zhang, and I. Lo, "Simulation of colloid transport and retention using a pore-network model with roughness and chemical heterogeneity on pore surfaces," *Water Resources Research*, vol. 57, no. 2, p. e2020WR028571, 2021.

[216] J. Wan and J. L. Wilson, "Colloid transport in unsaturated porous media," *Water Resources Research*, vol. 30, no. 4, pp. 857–864, 1994.

[217] V. Lazouskaya, Y. Jin, and D. Or, "Interfacial interactions and colloid retention under steady flows in a capillary channel (vol 303, pg 171, 2006)," *Journal of Colloid and Interface Science*, vol. 405, pp. 346–346, 2006.

[218] Y. Zevi, B. Gao, W. Zhang, V. L. Morales, M. E. Cakmak, E. A. Medrano, W. Sang, and T. S. Steenhuis, "Colloid retention at the meniscus-wall contact

line in an open microchannel," *Water Research*, vol. 46, no. 2, pp. 295–306, 2012.

[219] G. Chen and M. Flury, "Retention of mineral colloids in unsaturated porous media as related to their surface properties," *Colloids and surfaces A: Physicochemical and Engineering Aspects*, vol. 256, no. 2-3, pp. 207–216, 2005.

[220] S. Rahmatpour, M. R. Mosaddeghi, M. Shirvani, and J. Simunek, "Transport of silver nanoparticles in intact columns of calcareous soils: The role of flow conditions and soil texture," *Geoderma*, vol. 322, pp. 89–100, 2018.

[221] S. Torkzaban and S. A. Bradford, "Critical role of surface roughness on colloid retention and release in porous media," *Water Research*, vol. 88, pp. 274–284, 2016.

[222] M. Polemio, S. Bufo, and S. Paoletti, "Evaluation of ionic strength and salinity of groundwaters: effect of the ionic composition," *Geochimica et Cosmochimica Acta*, vol. 44, no. 6, pp. 809–814, 1980.

[223] A. L. Mills, J. S. Herman, G. M. Hornberger, and T. H. DeJesús, "Effect of solution ionic strength and iron coatings on mineral grains on the sorption of bacterial cells to quartz sand," *Applied and Environmental Microbiology*, vol. 60, no. 9, pp. 3300–3306, 1994.

[224] P. Babakhani, J. Bridge, R.-a. Doong, and T. Phenrat, "Continuum-based models and concepts for the transport of nanoparticles in saturated porous media: A state-of-the-science review," *Advances in Colloid and Interface Science*, vol. 246, pp. 75–104, 2017.

[225] K. L. Chen and M. Elimelech, "Aggregation and deposition kinetics of fullerene (c60) nanoparticles," *Langmuir*, vol. 22, no. 26, pp. 10994–11001, 2006.

[226] C. J. Van Oss, *Interfacial forces in aqueous media*. CRC press, 2006.

[227] J. T. Crist, Y. Zevi, J. F. McCarthy, J. A. Throop, and T. S. Steenhuis, "Transport and retention mechanisms of colloids in partially saturated porous media," *Vadose Zone Journal*, vol. 4, no. 1, pp. 184–195, 2005.

[228] R. Kohli and K. L. Mittal, *Developments in Surface Contamination and Cleaning, Vol. 1: Fundamentals and Applied Aspects*. William Andrew, 2015.

[229] G. C. Iltis, R. T. Armstrong, D. P. Jansik, B. D. Wood, and D. Wildenschild, "Imaging biofilm architecture within porous media using synchrotron-based x-ray computed microtomography," *Water Resources Research*, vol. 47, no. 2, 2011.

[230] J. Wielinski, A. Gogos, A. Voegelin, C. R. Müller, E. Morgenroth, and R. Kaegi, "Release of gold (au), silver (ag) and cerium dioxide (ceo 2) nanoparticles from sewage sludge incineration ash," *Environmental Science: Nano*, vol. 8, no. 11, pp. 3220–3232, 2021.

[231] N. S. Tulve, A. B. Stefaniak, M. E. Vance, K. Rogers, S. Mwilu, R. F. LeBouf, D. Schwegler-Berry, R. Willis, T. A. Thomas, and L. C. Marr, "Characterization of silver nanoparticles in selected consumer products and its relevance for predicting children's potential exposures," *International journal of hygiene and environmental health*, vol. 218, no. 3, pp. 345–357, 2015.

[232] E. Smulders and W. Rähse, *Laundry detergents*. Wiley Online Library, 2002.

[233] M. Flury and H. Qiu, "Modeling colloid-facilitated contaminant transport in the vadose zone," *Vadose Zone Journal*, vol. 7, no. 2, pp. 682–697, 2008.

[234] S. Granger, R. Bol, P. Butler, P. Haygarth, P. Naden, G. Old, P. Owens, and B. Smith, "Processes affecting transfer of sediment and colloids, with associated phosphorus, from intensively farmed grasslands: tracing sediment and organic matter," *Hydrological Processes: An International Journal*, vol. 21, no. 3, pp. 417–422, 2007.

[235] D. P. Jaisi, N. B. Saleh, R. E. Blake, and M. Elimelech, "Transport of single-walled carbon nanotubes in porous media: filtration mechanisms and reversibility," *Environmental Science & Technology*, vol. 42, no. 22, pp. 8317–8323, 2008.

[236] N. A. Marley, J. S. Gaffney, K. A. Orlandini, and M. M. Cunningham, "Evidence for radionuclide transport and mobilization in a shallow, sandy aquifer," *Environmental Science & Technology*, vol. 27, no. 12, pp. 2456–2461, 1993.

[237] J. Mibus, S. Sachs, W. Pfingsten, C. Nebelung, and G. Bernhard, "Migration of uranium (iv)/(vi) in the presence of humic acids in quartz sand: A laboratory column study," *Journal of Contaminant Hydrology*, vol. 89, no. 3-4, pp. 199–217, 2007.

[238] T. K. Sen and K. C. Khilar, "Review on subsurface colloids and colloid-associated contaminant transport in saturated porous media," *Advances in Colloid and Interface Science*, vol. 119, no. 2-3, pp. 71–96, 2006.

[239] J. Gregory, "Approximate expressions for retarded van der waals interaction," *Journal of Colloid and Interface Science*, vol. 83, no. 1, pp. 138–145, 1981.

[240] S. Lin and M. R. Wiesner, "Paradox of stability of nanoparticles at very low ionic strength," *Langmuir*, vol. 28, no. 30, pp. 11032–11041, 2012.

[241] H.-J. Butt, B. Cappella, and M. Kappl, "Force measurements with the atomic force microscope: Technique, interpretation and applications," *Surface Science Reports*, vol. 59, no. 1-6, pp. 1–152, 2005.

[242] J. A. Wood and L. Rehmann, "Geometric effects on non-dlvo forces: relevance for nanosystems," *Langmuir*, vol. 30, no. 16, pp. 4623–4632, 2014.

[243] R.-H. Yoon and L. Mao, "Application of extended dlvo theory, iv: derivation of flotation rate equation from first principles," *Journal of Colloid and Interface Science*, vol. 181, no. 2, pp. 613–626, 1996.

[244] V. L. Morales, M. Dentz, M. Willmann, and M. Holzner, "Stochastic dynamics of intermittent pore-scale particle motion in three-dimensional porous media: Experiments and theory," *Geophysical Research Letters*, vol. 44, no. 18, pp. 9361–9371, 2017.

[245] R.-H. Yoon and B. S. Aksoy, "Hydrophobic forces in thin water films stabilized by dodecylammonium chloride," *Journal of Colloid and Interface Science*, vol. 211, no. 1, pp. 1–10, 1999.

[246] F. Bartell and J. Smith, "Alteration of surface properties of gold and silver as indicated by contact angle measurements," *The Journal of Physical Chemistry*, vol. 57, no. 2, pp. 165–172, 1953.

[247] K. S. Gadre and T. Alford, "Contact angle measurements for adhesion energy evaluation of silver and copper films on parylene-n and sio 2 substrates," *Journal of applied physics*, vol. 93, no. 2, pp. 919–923, 2003.

[248] L. W. de Jonge, C. Kjærgaard, and P. Moldrup, "Colloids and colloid-facilitated transport of contaminants in soils: An introduction," *Vadose Zone Journal*, vol. 3, no. 2, pp. 321–325, 2004.

[249] A. D. Maynard, R. J. Aitken, T. Butz, V. Colvin, K. Donaldson, G. Oberdörster, M. A. Philbert, J. Ryan, A. Seaton, V. Stone, *et al.*, "Safe handling of nanotechnology," *Nature*, vol. 444, no. 7117, pp. 267–269, 2006.

[250] C. Tien and A. C. Payatakes, "Advances in deep bed filtration," *AIChE Journa*, vol. 25, no. 5, pp. 737–759, 1979.

[251] D. C. Mays and J. R. Hunt, "Hydrodynamic and chemical factors in clogging by montmorillonite in porous media," *Environmental Science & Technology*, vol. 41, no. 16, pp. 5666–5671, 2007.

[252] S. Torkzaban, S. A. Bradford, J. L. Vanderzalm, B. M. Patterson, B. Harris, and H. Prommer, "Colloid release and clogging in porous media: Effects of solution ionic strength and flow velocity," *Journal of Contaminant Hydrology*, vol. 181, pp. 161–171, 2015.

[253] A. Dexter, "Advances in characterization of soil structure," *Soil and Tillage Research*, vol. 11, pp. 199–238, 06 1988.

[254] Y. Cheng, L. Yin, S. Lin, M. Wiesner, E. Bernhardt, and J. Liu, "Toxicity reduction of polymer-stabilized silver nanoparticles by sunlight.," *The Journal of Physical Chemistry C*, vol. 115, pp. 4425–4432, 2011.

[255] J. Jiang, G. Oberdoerster, and P. Biswas, "Characterization of size, surface charge, and agglomeration state of nanoparticle dispersions for toxicological studies.," *Journal of Nanoparticle Research*, vol. 11, pp. 77–89, 2008.

[256] D. Jassby, J. Farner Budarz, and M. Wiesner, "Impact of aggregate size and structure on the photocatalytic properties of tio2 and zno nanoparticles.," *Environmental Science & Technology*, vol. 46, no. 13, pp. 6934–6941, 2012.

[257] C. Levard, E. M. Hotze, G. V. Lowry, and J. Brown, G. E., "Environmental transformations of silver nanoparticles: impact on stability and toxicity.," *Environmental Science & Technology*, vol. 46, pp. 6900–6914, 2012.

[258] K. Tiede, M. Hassellov, E. Breitbarth, Q. Chaudhry, and A. Boxall, "Considerations for environmental fate and ecotoxiclogy testing to support environmental risk assessments for engineered nanoparticles.," *Journal of Chromatography*, vol. 1216, pp. 503–509, 2009.

[259] X. Li and J. J. Lenhart, "Aggregation and dissolution of silver nanoparticles in natural surface water.," *Environmental Science & Technology*, vol. 46, pp. 5378–5386, 2012.

[260] E. M. Hotze, J.-Y. Bottero, and M. R. Wiesner, "Theoretical framework for nanoparticle reactivity as a function of aggregation state.," *Langmuir*, vol. 26, pp. 11170–11175, 2010.

[261] M. Wiesner, "Morphology of particle deposits.," *Journal of Environmental Engineering*, vol. 125, no. 12, pp. 1124–1132, 1999.

[262] L. Fellay, C. Twist, and M. Vanni, "Motion of rigid aggregates under different flow conditions," *Acta Mechanica*, vol. 224, no. 10, pp. 2225–2248, 2013.

[263] S. Veerapaneni and M. Wiesner, "Hydrodynamics of fractal aggregates with radially varying permeability.," *Journal of Colloid and Interface Science*, vol. 177, pp. 45–57, 1996.

[264] S. Bradford, J. Simunek, M. Bettahar, M. van Genuchten, and S. Yates, "Modeling colloid attachment, straining, and exclusion in saturated porous media.," *Environmental Science & Technology*, vol. 37, no. 10, pp. 2242–2250, 2003.

[265] I. Chowdhury, S. Walker, and S. Mylon, "Aggregate morphology of nano-tio 2: role of primary particle size, solution chemistry, and organic matter.," *Environmental Science: Processes & Impacts*, vol. 15, no. 1, pp. 275–282, 2013.

[266] Q. Liu, V. Lazouskaya, Q. He, and Y. Jin, "Effect of particle shape on colloid retention and release in saturated porous media," *Journal of Environmental Quality*, vol. 29, pp. 500–508, 2010.

[267] M. Salerno, M. Flamm, B. E. Logan, and D. Valegol, "Transport of rodlike colloids through packed beds," *Environmental Science & Technology*, vol. 40, pp. 6336–6340, 2006.

[268] M. Seymour, G. Chen, C. Su, and Y. Li, "Transport and retention of colloids in porous media: Does shape really matter?," *Environmental Science & Technology*, vol. 47, pp. 8391–8398, 2013.

[269] S. Xu, Q. Liao, and J. Saiers, "Straining of nonshperical colloids in saturated porous media," *Environmental Science & Technology*, vol. 42, pp. 771–778, 2008.

[270] T. H. Weiss, A. L. Mills, G. M. Hornberger, and J. S. Herman, "Effect of bacterial cell shape on transport of bacteria in porous media," *Environmental Science & Technology*, vol. 29, pp. 1737–1740, 1995.

[271] D. Zhou and A. A. Keller, "Role of morphology in the aggregation kinetics of zno nanoparticles," *Water Research*, vol. 44, no. 9, pp. 2948–2956, 2010.

[272] V. Oles, "Shear-induced aggregation and breakup of polysterene latex particles," *Journal of Colloid and Interface Science*, vol. 154, no. 2, pp. 351–358, 1992.

[273] D. Wei, H. Wu, Z. Xia, D. Xie, L. Zhong, and M. Morbidelli, "Monitoring coalescence behavior of soft colloidal particles in water by small-angle light scattering," *Colloid and Polymer Science*, vol. 290, no. 11, pp. 1033–1040, 2012.

[274] A. Zaccone, D. Gentili, H. Wu, and M. Morbidelli, "Shear-induced reaction-limited aggregation kinetics of brownian particles at arbitrary concentrations," *The Journal of Chemical Physics*, vol. 132, 2010.

[275] J. Gregory, "Interaction of unequal double layers at constant charge," *Journal of Colloid and Interface Science*, vol. 51, no. 1, pp. 44–51, 1975.

[276] J. Husband and J. Adams, "Shear-induced aggregation of carboxylated polymer latices.," *Colloid and Polymer Science*, vol. 270, no. 12, pp. 1194–1200, 1992.

[277] J. Schindelin, I. Arganda-Carreras, and E. Frise, ""fiji: an open-source platform for biological-image analysis"," *Nature Methods*, vol. 9, no. 7, pp. 676–682, 2012.

[278] M. Doube, M. Klosowski, I. Arganda-Carreras, F. Cordelieres, R. Dougherty, J. Jackson, B. Schmid, J. Hutchinson, and S. Shefelbine, "Bonej: free and extensible bone image analysis in imagej.," *Bone*, vol. 47, pp. 1076–1079, 2010.

[279] C. Lee and T. Kramer, "Prediction of three-dimensional fractal dimensions using the two-dimensional properties of fractal aggregates.," *Adv. Colloid Interface Sci.*, vol. 112, no. 1-3, pp. 49–57, 2004.

[280] M. Soos, A. Moussa, L. Ehrl, J. Sefcik, H. Wu, and M. Morbidelli, "Effect of shear rate on aggregate size and morphology investigated under turbulent conditions in stirred tank.," *J. Colloid Interface Sci.*, vol. 319, no. 2, pp. 577–589, 2008.

[281] S. A. Bradford, J. Simunek, M. Bettahar, M. T. Van Genuchten, and S. Yates, "Significance of straining in colloid deposition: Evidence and implications," *Water Resources Research*, vol. 42, no. 12, 2006.

[282] S. Veerapaneni and M. Wiesner, "Deposit morphology and head loss development in porous media.," *Environmental Science & Technology*, vol. 31, no. 10, pp. 2738–2744, 1997.

[283] R. Darby, *Chemical engineering fluid mechanics, revised and expanded*. Taylor and Francis, 2001.

[284] C. J. van Oss, "The extended dlvo theory," vol. 16, pp. 31–48, 2008.

[285] E. Pazmino, J. Trauscht, and W. P. Johnson, "Release of colloids from primary minimum contact under unfavorable conditions by perturbations in ionic strength and flow rate," *Environmental Science & Technology*, vol. 48, no. 16, pp. 9227–9235, 2014.

[286] R. Duffadar, S. Kalasin, J. M. Davis, and M. M. Santore, "The impact of nanoscale chemical features on micron-scale adhesion: Crossover from heterogeneity-dominated to mean-field behavior," *Journal of Colloid and Interface Science*, vol. 337, no. 2, pp. 396–407, 2009.

[287] H. Ma, E. Pazmino, and W. P. Johnson, "Surface heterogeneity on hemispheres-in-cell model yields all experimentally-observed non-straining colloid retention mechanisms in porous media in the presence of energy barriers," *Langmuir*, vol. 27, no. 24, pp. 14982–14994, 2011.

[288] F. Miele, P. De Anna, and M. Dentz, "Stochastic model for filtration by porous materials," *Physical Review Fluids*, vol. 4, no. 9, p. 094101, 2019.

[289] J. E. Patiño, F. J. Pérez-Reche, and V. L. Morales, "Retention site contribution towards silver particle immobilization in porous media," *Water Resources Research*, p. e2021WR031807, 2022.

[290] K. VanNess, A. Rasmuson, C. A. Ron, and W. P. Johnson, "A unified force and torque balance for colloid transport: Predicting attachment and mobilization under favorable and unfavorable conditions," *Langmuir*, vol. 35, no. 27, pp. 9061–9070, 2019.

[291] L. Song, P. R. Johnson, and M. Elimelech, "Kinetics of colloid deposition onto heterogeneously charged surfaces in porous media," *Environmental Science & Technology*, vol. 28, no. 6, pp. 1164–1171, 1994.

[292] M. Bendersky, M. M. Santore, and J. M. Davis, "Statistically-based dlvo approach to the dynamic interaction of colloidal microparticles with topographically and chemically heterogeneous collectors," *Journal of Colloid and Interface Science*, vol. 449, pp. 443–451, 2015.

[293] A. Rasmuson, K. VanNess, C. A. Ron, and W. P. Johnson, "Hydrodynamic versus surface interaction impacts of roughness in closing the gap between favorable and unfavorable colloid transport conditions," *Environmental Science & Technology*, vol. 53, no. 5, pp. 2450–2459, 2019.